

Development of Improved Guidelines and Designs for Thin Whitetopping: Environmental Response of Full-Scale BCOA Sections

Authors:

A. Mateos, J. Harvey, R. Wu, F. Paniagua, and J. Paniagua

Partnered Pavement Research Center (PPRC) Project Number 4.58B (DRISI Task 2878):
Evaluate Early Age and Premature Cracking for PaveM and LCCA (whitetopping)

PREPARED FOR:

California Department of Transportation
Division of Research, Innovation, and System Information
Office of Materials and Infrastructure

PREPARED BY:

University of California
Pavement Research Center
UC Davis, UC Berkeley



TECHNICAL REPORT DOCUMENTATION PAGE

1. REPORT NUMBER UCPRC-RR-2017-03	2. GOVERNMENT ASSOCIATION NUMBER	3. RECIPIENT'S CATALOG NUMBER
4. TITLE AND SUBTITLE Development of Improved Guidelines and Designs for Thin Whitetopping: Environmental Response of Full-Scale BCOA Sections		5. REPORT PUBLICATION DATE May 2020
		6. PERFORMING ORGANIZATION CODE
7. AUTHOR(S) A. Mateos (ORCID 0000-0002-3614-2858), J. Harvey (ORCID 0000-0002-8924-6212), R. Wu (ORCID 0000-0001-7364-7583), F. Paniagua (ORCID 0000-0002-2385-4899), and J. Paniagua (ORCID 0000-0003-4062-5454)		8. PERFORMING ORGANIZATION REPORT NO. UCPRC-RR-2017-03
9. PERFORMING ORGANIZATION NAME AND ADDRESS University of California Pavement Research Center Department of Civil and Environmental Engineering, UC Davis 1 Shields Avenue Davis, CA 95616		10. WORK UNIT NUMBER
		11. CONTRACT OR GRANT NUMBER 65A0542
12. SPONSORING AGENCY AND ADDRESS California Department of Transportation Division of Research, Innovation, and System Information P.O. Box 942873 Sacramento, CA 94273-0001		13. TYPE OF REPORT AND PERIOD COVERED Research Report January 2015 to December 2016
		14. SPONSORING AGENCY CODE
15. SUPPLEMENTAL NOTES		
16. ABSTRACT Fifteen bonded concrete overlay of asphalt (BCOA) sections were built at the UCPRC facility in Davis, California, from February 23 to 25, 2016. The concrete mixes included Type II/V and Type III portland cements and calcium sulfoaluminate cement, and they were designed to provide 2.8 MPa (400 psi) flexural strength after either 4 or 10 hours. Six of the 15 sections were instrumented with a total of 245 sensors to measure the responses to environmental actions and cement hydration. Based on the analysis of the data collected by these sensors up until May 31, 2017, preliminary conclusions were drawn regarding how the different section configurations and concrete types responded to moisture and temperature-related actions. A clear link between drying shrinkage, concrete relative humidity, and environmental conditions was verified. Very high levels of drying shrinkage were measured in all portland cement mixes. For these mixes, the topical use of a shrinkage-reducing admixture proved to be an effective and efficient way to reduce drying shrinkage. Due to the low water/cement ratio of the portland cement mixes, very high levels of autogenous shrinkage occurred except in the mix that had been internally cured with pre-wetted lightweight aggregates. Autogenous shrinkage barely occurred in the internally cured mix. The mix with calcium sulfoaluminate cement did not present any autogenous shrinkage and presented much lower drying shrinkage than the mixes with portland cement. Despite the high levels of drying shrinkage in the mixes with portland cement, the concrete and asphalt remained fully bonded. For all the mixes, the apparent coefficient of thermal expansion was clearly influenced by the environmental conditions. Overall, thermal deformations of the mixes were much higher than predicted using the coefficient of thermal expansion determined in the laboratory under saturated conditions.		
17. KEY WORDS BCOA, rigid pavement, bonded concrete overlay of asphalt, thin whitetopping, early high-strength concrete, coefficient of thermal expansion, moisture-related shrinkage, relative humidity, concrete shrinkage, drying shrinkage		18. DISTRIBUTION STATEMENT No restrictions. This document is available to the public through the National Technical Information Service, Springfield, VA 22161
19. SECURITY CLASSIFICATION (of this report) Unclassified	20. NUMBER OF PAGES 102	21. PRICE None

Reproduction of completed page authorized

UCPRC ADDITIONAL INFORMATION

1. DRAFT STAGE Final	2. VERSION NUMBER 1
3. PARTNERED PAVEMENT RESEARCH CENTER STRATEGIC PLAN ELEMENT NUMBER 4.58B	4. DRISI TASK NUMBER 2878
5. CALTRANS TECHNICAL LEAD AND REVIEWER(S) D. Maskey	6. FHWA NUMBER CA202878A

7. PROPOSALS FOR IMPLEMENTATION

This research report includes a preliminary analysis of the environmental response of BCOA pavements. Several conclusions were drawn that can significantly impact the way BCOA and other concrete pavements are designed and built. These conclusions are related to drying shrinkage and thermal deformation. This report includes only a preliminary analysis of the data collected in the 4.58B project. Further analysis has been included in two companion reports, one focused on moisture-related shrinkage and another focused on thermal deformation. The preliminary conclusions discussed in this report and its companions should be considered in the design of pilot projects for BCOA.

8. RELATED DOCUMENTS

- Mateos, J. Harvey, J. Paniagua, and F. Paniagua. Development of Improved Guidelines and Designs for Thin Whitetopping: Literature Review. 2015. Technical Memorandum: UCPRC-TM-2015-01.
- Mateos, J. Harvey, F. Paniagua, J. Paniagua, and R. Wu. Development of Improved Guidelines and Designs for Thin Whitetopping: Construction and Initial Environmental Response of Full-Scale BCOA Sections. 2018. Research Report: UCPRC-RR-2017-02.
- Mateos, J. Harvey, J. Paniagua, R. Wu, and F. Paniagua. Development of Improved Guidelines and Designs for Thin Whitetopping: Environmental Effects on the Coefficient of Thermal Expansion of the Concrete. 2019. Research Report: UCPRC-RR-2017-04.
- Mateos, J. Harvey, F. Paniagua, J. Paniagua, and R. Wu. Development of Improved Guidelines and Designs for Thin Whitetopping: Moisture-Related Shrinkage of BCOA Sections. 2019. Research Report: UCPRC-RR-2017-05.

9. LABORATORY ACCREDITATION

The UCPRC laboratory is accredited by AASHTO re:source for the tests listed in this report



10. SIGNATURES

A. Mateos FIRST AUTHOR	J.T. Harvey TECHNICAL REVIEW	D. Spinner EDITOR	J.T. Harvey PRINCIPAL INVESTIGATOR	D. Maskey CALTRANS TECH. LEADS	T.J. Holland CALTRANS CONTRACT MANAGER
----------------------------------	--	-----------------------------	--	--	--

Reproduction of completed page authorized

TABLE OF CONTENTS

LIST OF FIGURES	iv
LIST OF TABLES	v
ACKNOWLEDGMENTS	vi
PROJECT OBJECTIVES.....	vii
EXECUTIVE SUMMARY.....	ix
LIST OF ABBREVIATIONS.....	xi
1 INTRODUCTION.....	1
2 EXPERIMENT DESIGN	3
2.1 Description of the BCOA Environmental Sections.....	3
2.2 Instrumentation of the BCOA Environmental Sections	6
2.3 Data Collection from the BCOA Environmental Sections.....	13
2.4 Sign Criteria	15
3 ANALYSIS OF DATA COLLECTED FROM THE BCOA ENVIRONMENTAL SECTIONS.....	17
3.1 Data Collected by the Thermocouples	17
3.1.1 Examples of Collected Data	17
3.1.2 Data Analysis	18
3.1.3 Preliminary Conclusions	19
3.2 Data Collected by the Relative Humidity Sensors	25
3.2.1 Examples of Collected Data	25
3.2.2 Data Analysis	26
3.2.3 Preliminary Conclusions	26
3.3 Data Collected by the Moisture-Content Sensors	36
3.3.1 Examples of Collected Data	36
3.3.2 Data Analysis	36
3.3.3 Preliminary Conclusions	37
3.4 Data Collected by the Vibrating Wire Strain Gages	41
3.4.1 Examples of Collected Data	41
3.4.2 Data Analysis	43
3.4.3 Preliminary Conclusions	55
3.5 Data Collected by the JDMD and IOMD Sensors	72
3.5.1 Examples of Collected Data	72
3.5.2 Data Analysis	76
3.5.3 Preliminary Conclusions	77
4 CONCLUSIONS	81
REFERENCES.....	84
APPENDIX: SENSOR-NAMING CONVENTION	86

LIST OF FIGURES

Figure 1.1: Full-scale test track layout.....	2
Figure 2.1: Partial factorial design behind the ENV sections.....	4
Figure 2.2: Cross section of the full-scale BCOA sections.....	5
Figure 2.3: Instrumentation of the ENV sections.....	7
Figure 2.4: Vibrating wire strain gages (VWSGs).....	9
Figure 2.5: Anchoring system for vertical JDMDs.....	9
Figure 2.6: Example of vertical JDMDs (Section L).....	10
Figure 2.7: Example of a horizontal JDMD.....	10
Figure 2.8: Anchoring system for IOMDs.....	11
Figure 2.9: Interface opening measuring device (IOMD).....	11
Figure 2.10: Installation of thermocouples embedded in the concrete.....	12
Figure 2.11: Relative humidity and moisture-content sensors.....	13
Figure 2.12: Unrestrained shrinkage beams.....	14
Figure 3.1: Example of thermocouples readings (Section M, Slab 14, location -R).....	17
Figure 3.2: Example of thermocouples readings: Detail of Figure 3.1 (Section M, Slab 14, location -R).....	18
Figure 3.3: Temperature distribution during one year (Feb. 26, 2016 to Feb. 26, 2017, mean all ENV sections).....	19
Figure 3.4: Frequency distribution of the ELTD during one year (Feb. 26, 2016, to Feb. 26, 2017, mean all ENV sections).....	20
Figure 3.5: Distribution of concrete temperature at 5 mm (0.2 in.) depth, by section (Feb. 26, 2016 to Jan. 31, 2017).....	21
Figure 3.6: Distribution of concrete temperature at 5 mm (0.2 in.) depth, by cement type (Feb. 26, 2016, to Jan. 31, 2017).....	21
Figure 3.7: Distribution of mean slab temperature, by cement type (Feb. 26, 2016 to Jan. 31, 2017).....	22
Figure 3.8: Distribution of asphalt temperature, by cement type (Feb. 26, 2016, to Jan. 31, 2017).....	23
Figure 3.9: Distribution of ELTD, by cement type (Feb. 26, 2016 to Jan. 31, 2017).....	23
Figure 3.10: Effect of the shoulder on slabs edge temperature.....	24
Figure 3.11: Example of readings from RHC sensors at the center of the slab (Section N).....	25
Figure 3.12: Example of readings from RHS sensors at the center of the slab (Section N).....	26
Figure 3.13: Relative humidity measured by RHC sensors at slab center at 20 mm (0.8 in.) depth.....	27
Figure 3.14: Relative humidity measured by RHS sensors at slab center at 20 mm (0.8 in.) depth.....	27
Figure 3.15: Relative humidity measured by RHS sensors at slab shoulder corners at 20 mm (0.8 in.) depth.....	29
Figure 3.16: Relative humidity measured by RHC sensors at slab center at 50 mm (0.8 in.) depth.....	32
Figure 3.17: Example of diurnal variations of RH (Section N).....	33
Figure 3.18: RH dependence on temperature, based on RHC sensors at 20 mm (0.8 in.) depth.....	34
Figure 3.19: Example of readings from MC sensors (Section N).....	36
Figure 3.20: Moisture content at 20 mm (0.8 in.) depth.....	38
Figure 3.21: Moisture content at 50 mm (2.0 in.) depth.....	39
Figure 3.22: Example of diurnal variations of MC (Section L).....	40
Figure 3.23: Example of readings from VWSG sensors (Section N).....	42
Figure 3.24: Example of readings from VWSG sensors (unrestrained shrinkage beams).....	42
Figure 3.25: Strain composition for analysis of VWSG data.....	43
Figure 3.26: Example of mean and differential strain calculated from VWSG sensors (Section N, Slab 13-L, Figure 3.23 data).....	44
Figure 3.27: Example of early strain development (Section J, Slab 12-L).....	45
Figure 3.28: Example of determination of concrete field setting time (Section J, Slab 12-L).....	46
Figure 3.29: Correlation between lab and field setting times for the portland cement mixes.....	47
Figure 3.30: The evolution of moisture-related shrinkage and CTE in the USB strain model.....	49

Figure 3.31: Example of fitting with the uniaxial strain model (Beam 1, P2 mix).....	49
Figure 3.32: Model’s limitations during rainfall events.....	50
Figure 3.33: Evolution of the moisture-related shrinkage and CTE in the BCOA strains models.	53
Figure 3.34: Example of fitting with the BCOA strain model (ϵ_{MEAN} , Section N, Slab 13-L).....	53
Figure 3.35: Example of fitting with the BCOA strain model (ϵ_{DIFF} , Section N, Slab 13-L).....	54
Figure 3.36: Moisture-related shrinkage determined for the unrestrained shrinkage beams ($\epsilon_{Sh,T0}$).....	56
Figure 3.37: Moisture-related shrinkage determined in the laboratory (ASTM C157-08).	56
Figure 3.38: Differential drying shrinkage of the BCOA sections ($\epsilon_{DIFF,Sh,T0}$).	57
Figure 3.39: Preliminary modeling of slab response to drying shrinkage (6×6 slab).	60
Figure 3.40: Moisture-related shrinkage at the bottom of the slabs.	61
Figure 3.41: Differential drying shrinkage of the BCOA sections ($\epsilon_{DIFF,Sh,T0}$) (close-up of Figure 3.38).	63
Figure 3.42: Differential drying shrinkage versus relative humidity (Section L).	64
Figure 3.43: CTE backcalculated for the unrestrained shrinkage beams.	65
Figure 3.44: CTE backcalculated for the unrestrained shrinkage beams (close-up of Figure 3.43).	66
Figure 3.45: Example of active joint (Section K).	67
Figure 3.46: Transverse joint deployments in the BCOA sections.	68
Figure 3.47: Effect of transverse joint deployment on thermal bending compliance of the slabs.	71
Figure 3.48: Example of readings from vertical JDMDs in a section with 12×12 slabs (Section K).	72
Figure 3.49: Example of readings from horizontal JDMDs in a section with 12×12 slabs (Section K).	73
Figure 3.50: Example of readings from IOMDs in a section with 12×12 slabs (Section K).	73
Figure 3.51: Example of readings from vertical JDMDs in a section with 6×6 slabs (Section N).	74
Figure 3.52: Example of readings from horizontal JDMDs in a section with 6×6 slabs (Section N).	74
Figure 3.53: Example of readings from IOMDs in a section with 6×6 slabs (Section N).	75
Figure 3.54: Moisture-related component of the vertical displacements ($U_{V,Sh,T1}$), corner JDMDs.	77
Figure 3.55: Corner vertical displacements versus differential drying shrinkage ($U_{V,Sh,T0}$ vs $\epsilon_{DIFF,Sh,T0}$).	79
Figure 3.56: Moisture-related component of concrete-asphalt interface opening measured with IOMDs ($I_{Sh,T0}$).	80
Figure A.1: Example sensor codes (Section M).....	87
Figure A.2: Example sensor codes (Section K).	88

LIST OF TABLES

Table 2.1: Thermocouple Depths.....	11
Table A.1: Short Names of the Sensor Types	86

DISCLAIMER

This document is disseminated in the interest of information exchange. The contents of this report reflect the views of the authors who are responsible for the facts and accuracy of the data presented herein. The contents do not necessarily reflect the official views or policies of the State of California or the Federal Highway Administration. This publication does not constitute a standard, specification or regulation. This report does not constitute an endorsement by the Department of any product described herein.

For individuals with sensory disabilities, this document is available in alternate formats. For information, call (916) 654-8899, TTY 711, or write to California Department of Transportation, Division of Research, Innovation and System Information, MS-83, P.O. Box 942873, Sacramento, CA 94273-0001.

ACKNOWLEDGMENTS

A number of people have provided inputs and support for developing the research presented in this report. Special thanks must be given to the South West Concrete Pavement Association, particularly to its Executive Director Charles Stuart, and to the University of Pittsburgh, which was a subcontractor in this research project, and in particular to Julie Vandebossche and John DeSantis. The technical contribution from Teichert Materials, particularly by Pete Conlin, Moises Caballero, and Chris Fuchs, and from CTS Cement, particularly by Vince Perez and Art Bigelow, is acknowledged and greatly appreciated. Finally, special thanks are due to several experts for their valuable inputs to this project: Deepak Maskey (Caltrans), John Bolander (UC Davis), Tom Van Dam (NCE), and Jason Weiss (Oregon State University).

PROJECT OBJECTIVES

Thin whitetopping, also known as bonded concrete overlay of asphalt (BCOA), is a rehabilitation alternative consisting of a 100 to 175 mm (0.33 to 0.58 ft) thick portland cement concrete overlay on an existing flexible or composite pavement. The main goal of this project was to develop recommendations and guidance on the use of thin BCOA as a rehabilitation alternative for California based on the adoption of, and improvements to, the technology developed in other US states. Towards completion of that goal, this research report describes the environmental response of six full-scale BCOA sections that were built and monitored within the framework of Partnered Pavement Research Center Strategic Plan Element (PPRC SPE) Project 4.58B. The specific goals of the study presented in this report are listed below:

- ✓ Conduct a preliminary analysis of the data collected on the six full-scale BCOA sections
- ✓ Assess the consistency of the data collected with the different types of sensors
- ✓ Evaluate how environmental actions impact the structural response of BCOA
- ✓ Rank the different mixes, curing techniques, and slab sizes, based on the response to environmental actions and cement hydration
- ✓ Identify topics that require further analysis and research

EXECUTIVE SUMMARY

Fifteen bonded concrete overlay of asphalt (BCOA) sections were built at the UCPRC facility in Davis, California, from February 23 to 25, 2016. That construction was part of Caltrans Partnered Pavement Research Program Strategic Plan Element 4.58B, whose primary goal is to develop recommendations and guidance on the use of thin BCOA as a rehabilitation alternative for California. Six of the 15 sections were instrumented with 245 sensors to measure the response of the concrete slabs to environmental actions and cement hydration. These six sections are referred to as environmental sections (*ENV sections*).

The set of ENV sections is the result of a partial factorial design with three factors: concrete mix, concrete curing procedure, and slab size. The levels of each of these three factors are shown below:

- Concrete mix (each type of concrete is preceded by a shortened name used to refer to it in this report):
 - P2: 10-hour design opening time (OT) with Type II/V portland cement
 - P2-ICC: Internally cured concrete based on the P2 mix
 - P3: 4-hour design OT with Type III portland cement
 - CSA: 4-hour design OT with calcium sulfoaluminate (CSA) cement

Note: the Caltrans flexural strength requirement for opening time is 2.8 MPa (400 psi).
- Concrete curing procedures:
 - Curing compound
 - Shrinkage-reducing admixture (topical use) applied before the curing compound
- Slab size (in this report, each slab size is preceded by a shortened name used to refer to it):
 - 6×6: Half-lane width, 1.8×1.8 m (approximately 6×6 ft) slabs
 - 12×12: Full-lane width, 3.6×3.6 m (approximately 12×12 ft) slabs

The ENV sections instrumentation was designed to measure the slabs' structural, thermal, and moisture-related responses to environmental agents and cement hydration. Three sensor types were installed to measure structural response: 1) vibrating wire strain gages (VWSGs) to measure concrete horizontal strain; 2) joint displacement measuring devices (JDMDs) to measure slab corner and edge deflections (vertical displacement) and the opening and closing of transverse joints; and 3) interface opening measuring devices (IOMDs) to measure slab–base separation. Sensors to measure concrete temperature, moisture, and internal relative humidity were also installed. A weather station near the test track measured environmental conditions.

Most of the ENV section sensors began collecting data the day before the overlay construction, and they continued to collect data regularly until the end of 4.58B project. This report is based on data collected through May 31, 2017.

The data collected with the VWSGs, JDMDs, and IOMDs were analyzed by using incremental models that included thermal and moisture-related effects so that both the thermal and moisture-related components of strains and displacements could be determined. Data related to the concrete relative humidity, moisture-related components, and temperature were analyzed by calculating daily means and daily variations. Preliminary conclusions based on these analyses were drawn about how the different section configurations and concrete types responded to moisture and temperature-related actions.

The results reported here show a clear link between drying shrinkage and environmental conditions. Both slab bending and slab corner deflection tended to increase (in absolute value) during dry periods and they rapidly decreased after rainfall events. In both the dry and wet periods, the structural response of the slabs due to the environmental actions was in line with the changes in concrete relative humidity measured at 20 mm (0.8 in.) depth.

Very high levels of drying shrinkage—up to 800 $\mu\epsilon$ unrestrained shrinkage—were measured in all the portland-cement mixes treated with curing compound, while much lower values were measured in the mix with CSA cement. Topical application a shrinkage-reducing admixture proved to be an effective, efficient way to reduce drying shrinkage in the portland cement mixes. Very high autogenous shrinkage values, between 200 and 250 $\mu\epsilon$, were also measured in the portland-cement mixes with normal weight aggregates, while autogenous shrinkage barely occurred in the mix with pre-wetted lightweight aggregates. To the contrary, this internally cured mix presented more drying shrinkage than the mix upon which its design is based.

The apparent CTE of the BCOA slabs concrete tended to increase during dry periods and decreased after rainfall events. Overall, measured thermal deformations of the slabs were much higher—up to 60 percent greater—than the values predicted using CTE under saturated conditions in the laboratory. Deformations measured on a set of beams next to the test track supported the conclusion that the mixes' coefficient of thermal expansion (CTE) was highly influenced by concrete moisture.

With the exception of some transverse joints in the CSA sections, by August 2016 cracks were observed at all the transverse joints of all the other sections. This high joint deployment level is related to the high drying shrinkage levels estimated for all the mixes. However, despite the high drying shrinkage levels, the concrete and asphalt remained bonded 15 months after the overlay construction.

The preliminary analysis of the experimental data presented in this report identified a number of topics that required further analysis and research. These topics were analyzed as part of this research project. The analysis is included in two companion reports that are focused on concrete thermal and moisture-related deformations respectively.

LIST OF ABBREVIATIONS

ASTM	American Society for Testing and Materials
BCOA	Bonded concrete overlay of asphalt
CSA	Calcium sulfoaluminate
CTE	Coefficient of thermal expansion
DAS	Data acquisition system
ELTD	Equivalent linear temperature difference
ENV	Environmental response section
FDR	Full-depth reclamation
FST	Field setting time
HMA	Hot mix asphalt
HVS	Heavy Vehicle Simulator
IOMD	Interface opening measuring device
JDMD	Joint displacement measuring device
LVDT	Linear Variable Displacement Transducer
LWA	Lightweight aggregate
MC	Moisture content
OT	Opening time
RAP	Reclaimed asphalt pavement
RH	Relative humidity
RHC	Campbell Scientific CS215-L sensor
RHS	Sensirion SHT75 sensor
SRA	Shrinkage-reducing admixture
TAC	Asphalt temperature
TPCC	Mean slab temperature
UCPRC	University of California Pavement Research Center
USB	Unrestrained shrinkage beam
VWSG	Vibrating wire strain gage

SI* (MODERN METRIC) CONVERSION FACTORS

APPROXIMATE CONVERSIONS TO SI UNITS

Symbol	When You Know	Multiply By	To Find	Symbol
LENGTH				
in	inches	25.4	Millimeters	mm
ft	feet	0.305	Meters	m
yd	yards	0.914	Meters	m
mi	miles	1.61	Kilometers	Km
AREA				
in ²	square inches	645.2	Square millimeters	mm ²
ft ²	square feet	0.093	Square meters	m ²
yd ²	square yard	0.836	Square meters	m ²
ac	acres	0.405	Hectares	ha
mi ²	square miles	2.59	Square kilometers	km ²
VOLUME				
fl oz	fluid ounces	29.57	Milliliters	mL
gal	gallons	3.785	Liters	L
ft ³	cubic feet	0.028	cubic meters	m ³
yd ³	cubic yards	0.765	cubic meters	m ³
NOTE: volumes greater than 1000 L shall be shown in m ³				
MASS				
oz	ounces	28.35	Grams	g
lb	pounds	0.454	Kilograms	kg
T	short tons (2000 lb)	0.907	megagrams (or "metric ton")	Mg (or "t")
TEMPERATURE (exact degrees)				
°F	Fahrenheit	5 (F-32)/9 or (F-32)/1.8	Celsius	°C
ILLUMINATION				
fc	foot-candles	10.76	Lux	lx
fl	foot-Lamberts	3.426	candela/m ²	cd/m ²
FORCE and PRESSURE or STRESS				
lbf	poundforce	4.45	Newtons	N
lbf/in ²	poundforce per square inch	6.89	Kilopascals	kPa
APPROXIMATE CONVERSIONS FROM SI UNITS				
Symbol	When You Know	Multiply By	To Find	Symbol
LENGTH				
mm	millimeters	0.039	Inches	in
m	meters	3.28	Feet	ft
m	meters	1.09	Yards	yd
km	kilometers	0.621	Miles	mi
AREA				
mm ²	square millimeters	0.0016	square inches	in ²
m ²	square meters	10.764	square feet	ft ²
m ²	square meters	1.195	square yards	yd ²
ha	Hectares	2.47	Acres	ac
km ²	square kilometers	0.386	square miles	mi ²
VOLUME				
mL	Milliliters	0.034	fluid ounces	fl oz
L	liters	0.264	Gallons	gal
m ³	cubic meters	35.314	cubic feet	ft ³
m ³	cubic meters	1.307	cubic yards	yd ³
MASS				
g	grams	0.035	Ounces	oz
kg	kilograms	2.202	Pounds	lb
Mg (or "t")	megagrams (or "metric ton")	1.103	short tons (2000 lb)	T
TEMPERATURE (exact degrees)				
°C	Celsius	1.8C+32	Fahrenheit	°F
ILLUMINATION				
lx	lux	0.0929	foot-candles	fc
cd/m ²	candela/m ²	0.2919	foot-Lamberts	fl
FORCE and PRESSURE or STRESS				
N	newtons	0.225	Poundforce	lbf
kPa	kilopascals	0.145	poundforce per square inch	lbf/in ²

*SI is the symbol for the International System of Units. Appropriate rounding should be made to comply with Section 4 of ASTM E380 (Revised March 2003).

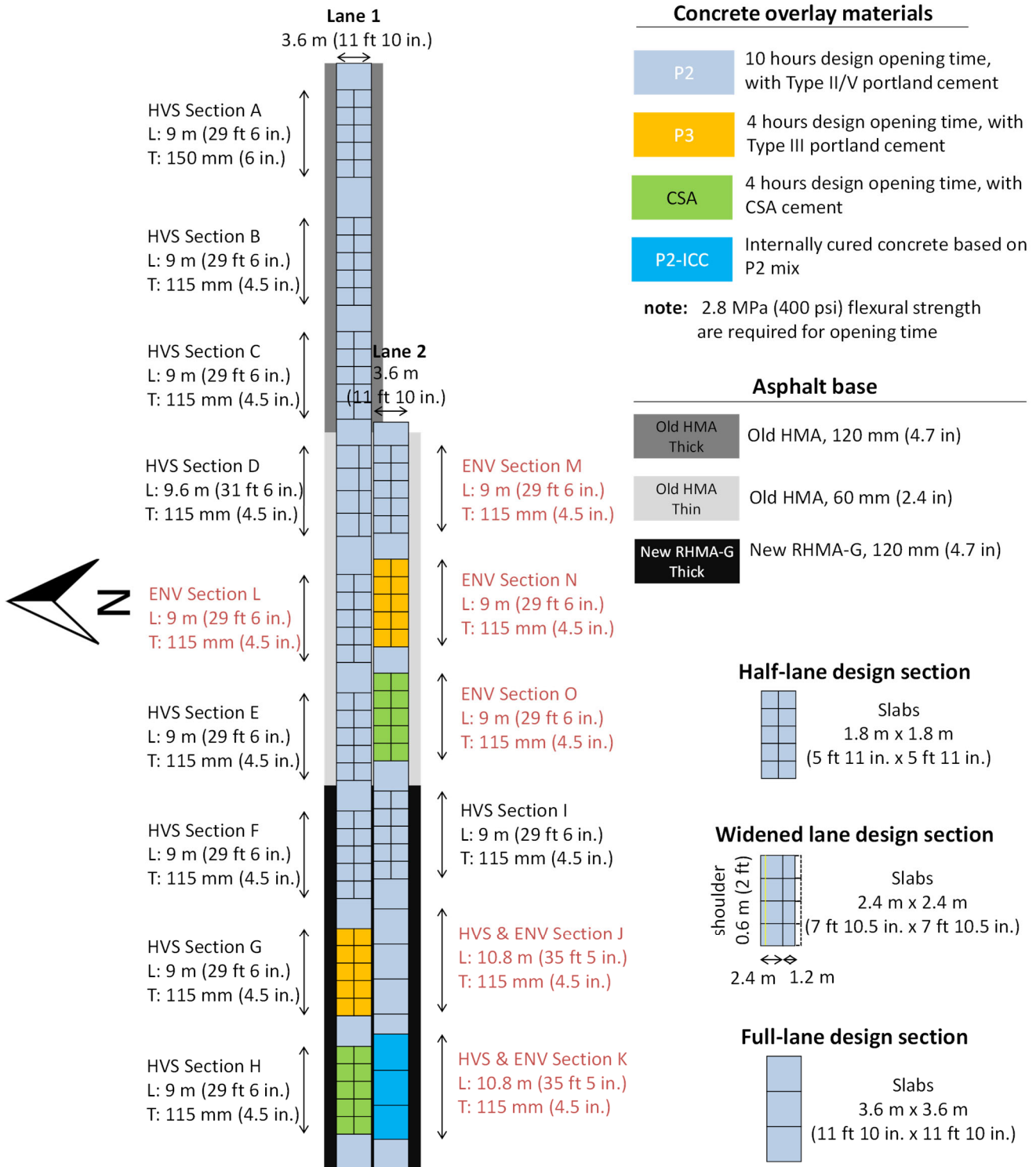
1 INTRODUCTION

Fifteen bonded concrete overlay of asphalt (BCOA) sections were built at the UCPRC facility in Davis, California, from February 23 to 25, 2016 (*1*). That construction was part of Caltrans Partnered Pavement Research Program Strategic Plan Element 4.58B, whose primary goal is to develop recommendations and guidance on the use of thin BCOA as a rehabilitation alternative for California based on the adoption of and improvements to the technology developed in other US states. Thin BCOA, formerly known as thin whitetopping, is a pavement rehabilitation technique that consists of placement of a 100 to 175 mm (0.33 to 0.58 ft) thick concrete overlay on an existing flexible or composite pavement.

Six of the 15 sections built in February 2016 were instrumented with 245 sensors to measure the concrete slabs' responses to the actions of changes in ambient environmental conditions that affect concrete pavement, primarily temperature and moisture conditions, and cement hydration. In this report these six sections are referred to as *ENV sections* (Figure 1.1), and analysis of the data collected on them through May 31, 2017, constitutes the report's main topic.

Descriptions of the BCOA ENV sections and their instrumentation is included in Chapter 2 of this report. The content of Chapter 2 is a summary of the more comprehensive information included in Reference (*1*). This reference is recommended for readers seeking additional information about the design and construction of the BCOA, the concrete mixes, the instrumentation design, the characteristics and performance of the sensors, and the data acquisition systems used for this research project. In Chapter 3, a few examples of collected data are shown for each type of sensor. Chapter 3 also includes the results of a preliminary analysis of the data collected up to May 31, 2017.

A preliminary analysis of the experimental data presented in this report identified a number of topics that required further analysis and research. These topics were analyzed as part of this research project. The analysis is included in two companion reports that are focused on concrete thermal and moisture-related deformations, respectively (*2, 3*). These references are recommended for readers seeking a deeper analysis of concrete slabs' hygrothermal deformations.



Notes: Environmental (ENV) sections are labeled with red in the figure. L = length, T = thickness of concrete. The underlying asphalt type is indicated by shading on the sides of test sections.

Figure 1.1: Full-scale test track layout.

2 EXPERIMENT DESIGN

2.1 Description of the BCOA Environmental Sections

The set of six environmental (ENV) sections is the result of a partial factorial design with three factors: concrete mix type, concrete curing procedure, and slab size (length and width only, because thickness was kept constant), as shown in Figure 2.1. These are regarded as the most important factors that determine the response of the slabs to environmental actions and to the cement hydration process. The levels for each of these three factors are shown below:

- Concrete mix (each type of concrete is preceded by a shortened name used to refer to it in this report):
 - P2: 10-hour design opening time (OT) with Type II/V portland cement
 - P2-ICC: Internally cured concrete based on the P2 mix
 - P3: 4-hour design OT with Type III portland cement
 - CSA: 4-hour design OT with calcium sulfoaluminate (CSA) cement

Note: the Caltrans flexural strength requirement for opening time is 2.8 MPa (400 psi).
- Concrete curing procedures:
 - Curing compound
 - Shrinkage-reducing admixture applied to the surface before the curing compound (referred to as “topical use”)
- Slab size (in this report, each slab size is preceded by a shortened name used to refer to it):
 - 6×6: Half-lane width, 1.8×1.8 m (approximately 6×6 ft) slabs
 - 12×12: Full-lane width, 3.6×3.6 m (approximately 12×12 ft) slabs

The levels of the three factors were set as part of the complete full-scale experiment design, which includes the six ENV sections that were not subjected to trafficking with the Heavy Vehicle Simulator (HVS) and the nine other sections that were subjected to HVS loading, all built in February 2016. The complete, full-scale experiment design is described in Section 2.2 of Reference (1).

As described in Reference (1), concrete mix designs were provided by the concrete industry and validated at the University of California Pavement Research Center (UCPRC). The design OTs of the mixes were based on overnight and 24 hour/weekend construction windows established by Caltrans. Specifically, a 4-hour design OT is required for mixes used in overnight road closures and a 10-hour design OT is required for mixes used in 24-hour and weekend-long construction windows. Mixes with two 4-hour OT cement types commonly used by Caltrans were included in the experiment: Type III portland cement and calcium sulfoaluminate (CSA) cement. The cement type might significantly impact the bonding between the concrete and the asphalt and the moisture-related shrinkage. The moisture-related shrinkage properties of CSA cement differ considerably from those of portland cement (4).

The standard curing compound process was applied to all the sections, except for Section M, according to Caltrans specifications for concrete pavements (Sections 40 and 90). On Section M, the shrinkage-reducing admixture (SRA) was applied before the curing compound. This section was included since Caltrans was interested in studying advanced curing techniques. The topical use of an SRA was selected for examination after input was received from national experts on concrete curing and consultants in the concrete pavements industry. The SRA dosage was 275 ml SRA/m² (7.8 oz/yd²). This total amount was supplied in three applications of SRA solution at 50 percent concentration. Further details about the SRA treatment design and application technique can be found in Reference (1).

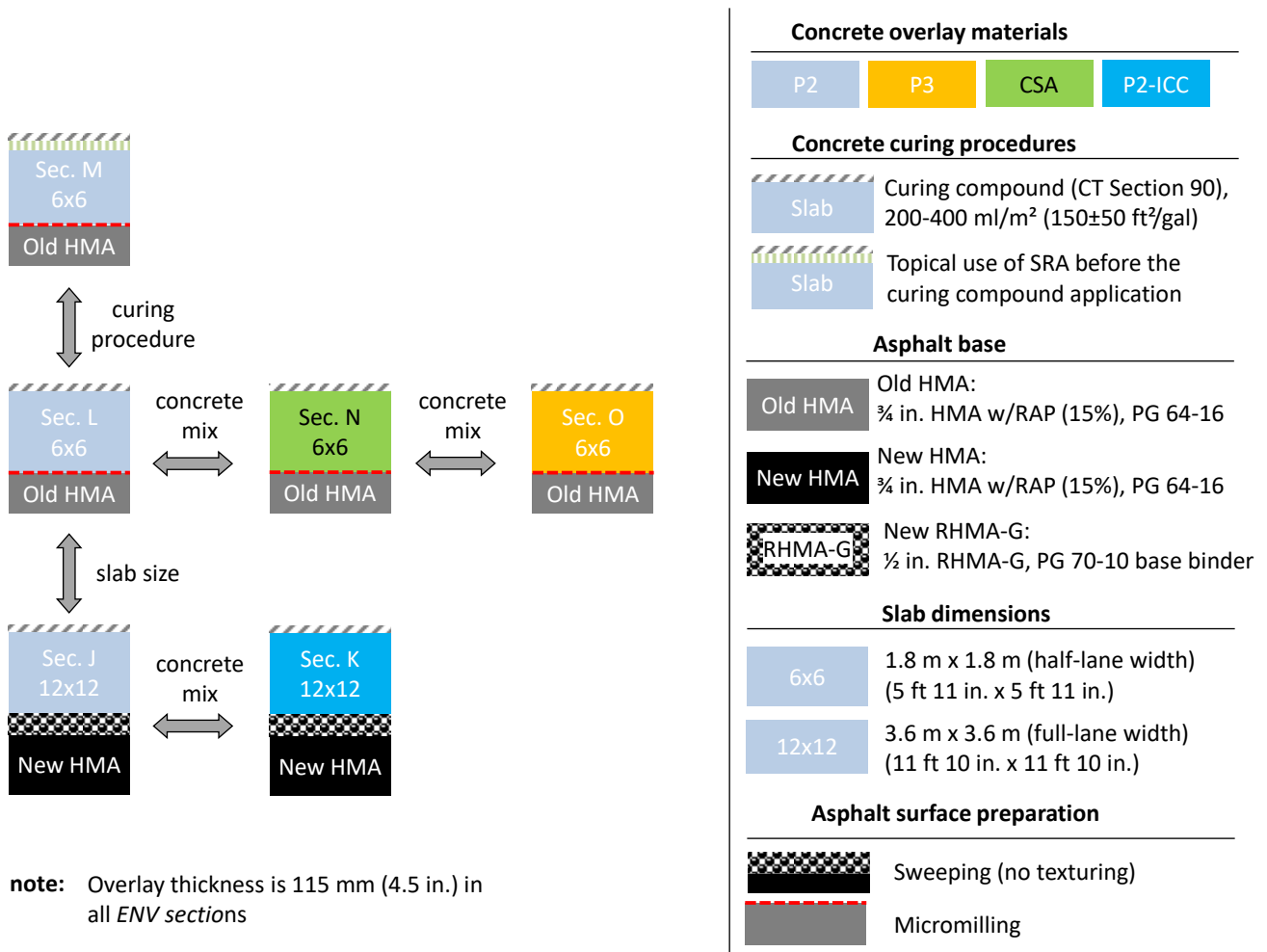
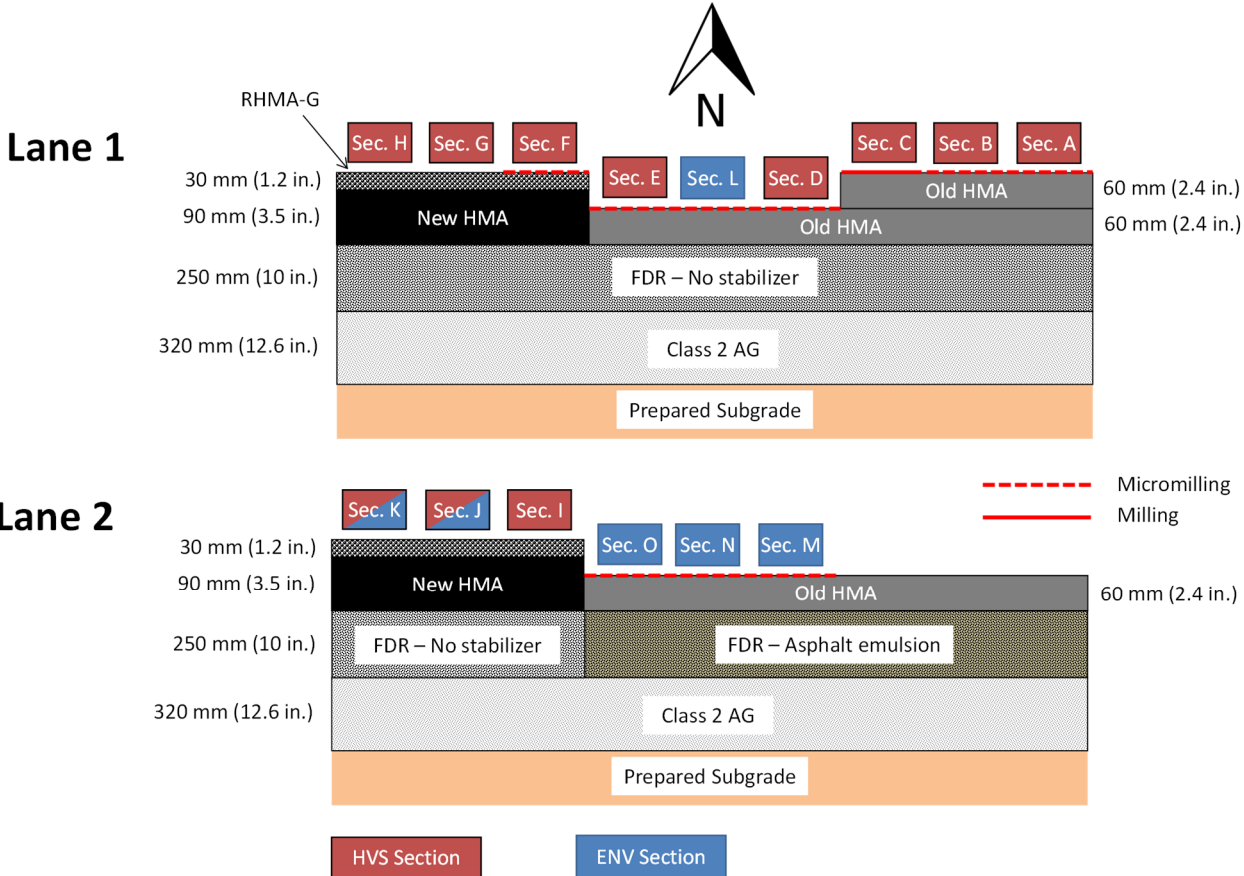


Figure 2.1: Partial factorial design behind the ENV sections.

The ENV sections included two types of asphalt bases (Figure 2.2). The 6×6 sections (L, M, N, and O) were built on top of a several-years-old asphalt mix that had been built and tested with the Heavy Vehicle Simulator (HVS) for an earlier UCPRC project on full-depth reclamation (5). That old mix consisted of dense-graded hot mix

asphalt (HMA), 19 mm (3/4 in.) nominal maximum aggregate size, with PG 64-16 binder and 15 percent reclaimed asphalt (RAP). This mix is referred to as *3/4 in. HMA w/RAP (15%), PG 64-16* in Figure 2.1. The old HMA was micromilled¹ to remove surface distresses and to create a uniform surface for overlay construction. The 12×12 sections (J and K) were built on top of a new rubberized gap-graded mix (RHMA-G) that was placed on October 2015, i.e., four months before the overlay construction. This mix is referred to as *1/2 in. RHMA-G, PG 70-10 base binder* in Figure 2.1. This 30 mm (1.2 in.) thick asphalt layer was paved on top of new HMA that was placed the same day. The new HMA was the same type as the old one: 3/4 in. HMA with RAP (15 percent), with PG 64-16 binder; all of these mixes are commonly used in California.



Note: The blue sections are the environmental sections (ENV sections). The red sections are the HVS sections that were subjected to accelerated pavement testing with the Heavy Vehicle Simulator (HVS). Sections J and K are both ENV and HVS sections since they were used to monitor the effects of environmental actions and cement hydration, and were also subjected to HVS testing.

Figure 2.2: Cross section of the full-scale BCOA sections.

¹ Milling is the typical technique used before placing a concrete overlay on an asphalt pavement. Micromilling is conducted using the same machine employed for milling but with a different drum that has a more teeth with smaller spacing than the one used for milling. The cost of micromilling is similar to that for milling, but it can remove asphalt surfaces as thin as 8 mm (1/3 in.), and with a greater precision than standard milling.

The subbase of all the BCOA sections was a 250 mm (10 in.) thick full-depth reclamation (FDR) layer. The FDR layer under Sections M, N, and O had been stabilized with asphalt emulsion, while no stabilizer was used in the FDR layer under the rest of the sections. More details of the flexible pavements under the concrete overlays can be found in Reference (1).

Construction of the concrete overlays took place on February 23 (Lane 1) and 25 (Lane 2), 2016. As Figure 1.1 shows, Lane 1 included one ENV section (Section L) while the rest of the ENV sections (Sections J, K, M, N, and O) were located in Lane 2. Weather conditions during construction were relatively mild, and no major incidents occurred during construction. Overall, all the mixes fulfilled the Caltrans requirements included in Section 39 of the Standard Specifications and in Section 40-5 of the Standard Special Provisions applicable to jointed plain concrete pavements built with rapid-strength concrete. Details of the construction process and results of the QC/QA testing can be found in Reference (1).

2.2 Instrumentation of the BCOA Environmental Sections

The ENV section instrumentation was designed to measure the slabs' structural and hygrothermal responses to environmental agents and cement hydration. Three types of sensors were installed to measure the structural response: vibrating wire strain gages (VWSGs), joint displacement measuring devices (JDMDs), and interface opening measuring devices (IOMDs). Sensors to measure concrete temperature, moisture, and internal relative humidity were also installed because these internal variables link the effects of environmental agents and cement hydration to the slabs' structural response. The instrumentation layout is shown in Figure 2.5, and a brief description of each of the sensors is presented below. More details of these sensors and the installation process can be found in Reference (1).

The vibrating wire strain gages measure concrete strain and were placed at three locations in the middle slab of each environmental section: at the slab center, at an interior corner, and at a corner at the shoulder. The gages were placed at two depths at each location: 20 mm (0.8 in.) below the slab surface and 20 mm (0.8 in.) above the slab bottom (Figure 2.4). They were configured this way to enable determination of slab expansion/contraction as well as bending (curling and warping). Figure 2.4 shows a picture with the VWSGs before placement of the concrete.

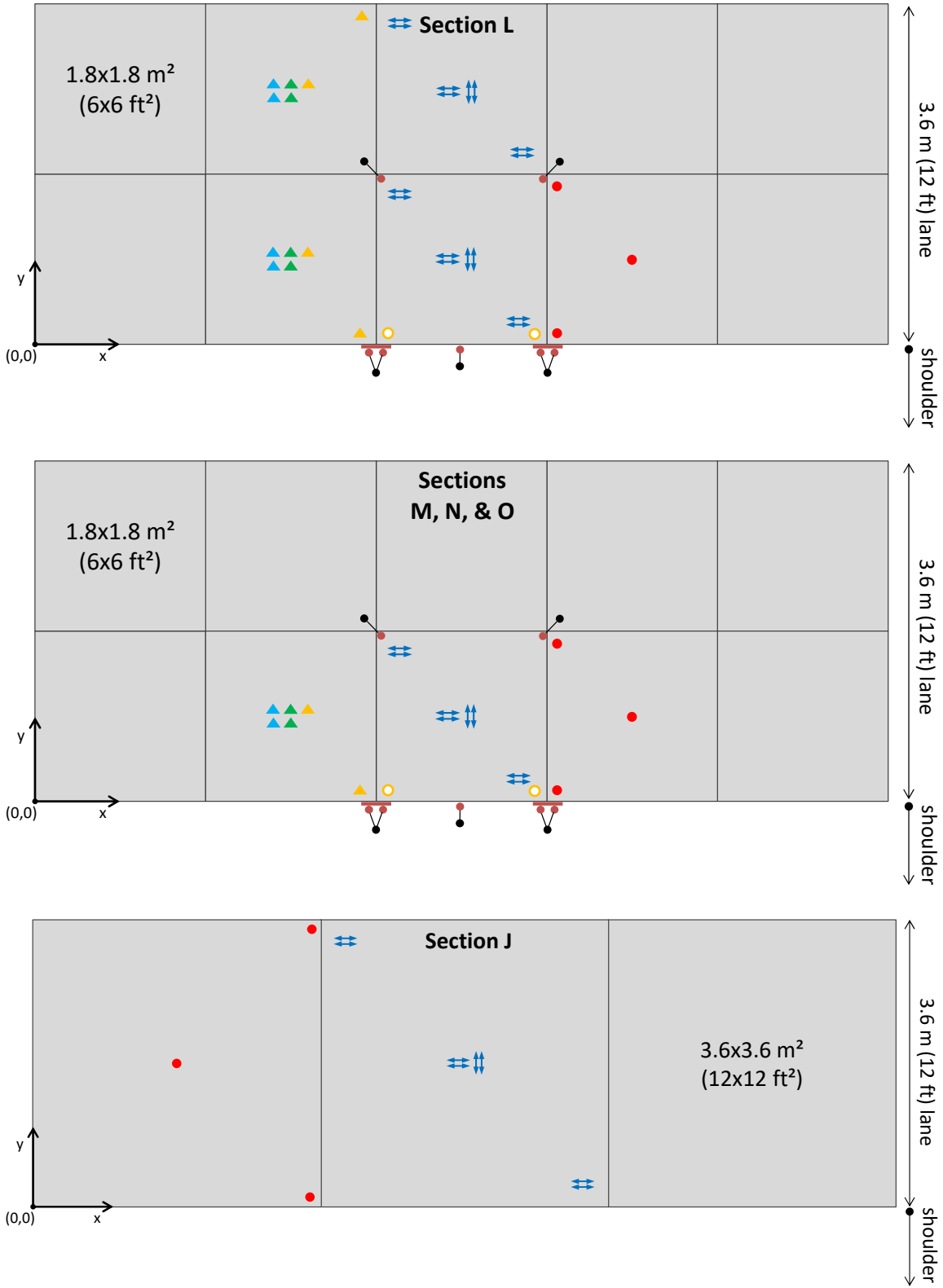
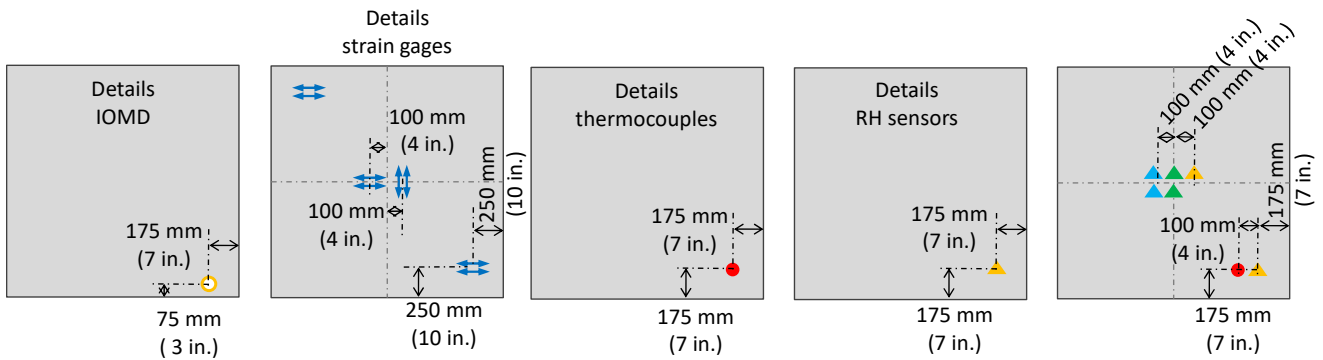
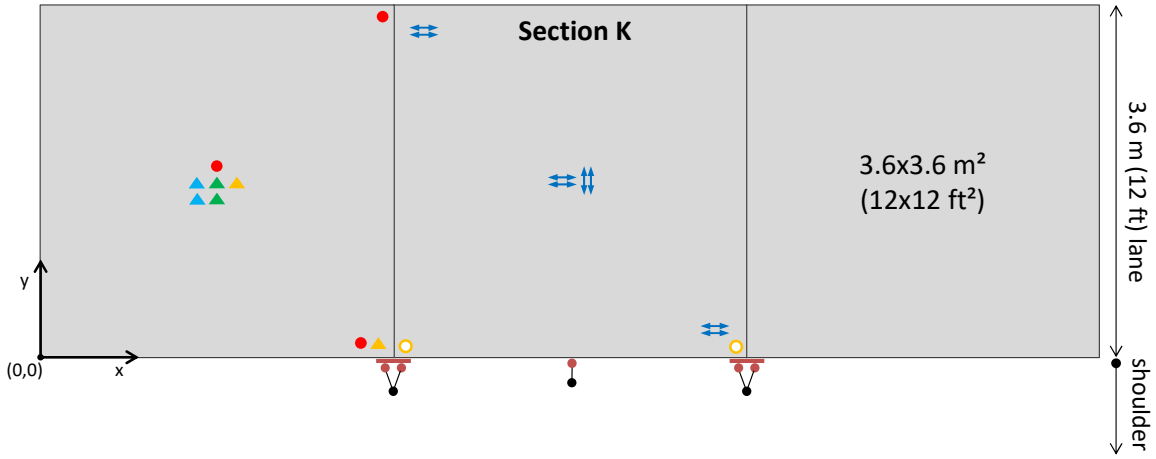


Figure 2.3: Instrumentation of the ENV sections.



-  JDMD (Joint Displacement Measuring Device)
 - 3 LVDTs: 2 vertical & 1 horizontal
 - Red points represent the 2 vertical LVDTs
 - Red line represents horizontal LVDT
 - Black point represents the anchoring rod
-  JDMD (Joint Displacement Measuring Device)
 - 1 vertical LVDT
 - Red point represents the vertical LVDT
 - Black point represents the anchoring rod
-  IOMD (Interface Opening Measuring Device)
 - 1 vertical LVDT
-  Static Strain Gages x 2 (in Concrete Slab)
 - 20 mm (0.8 in.) below slab surface
 - 20 mm (0.8 in.) above slab bottom
-  Thermocouples x 5 (4 in Concrete Slab + 1 in Asphalt Base)
 - 5 mm (0.2 in.) depth
 - 20 mm (0.8 in.) depth
 - 50 mm (2 in.) depth
 - Bottom concrete slab
 - Asphalt base (30 mm [1.2in] below asphalt surface)
-  Moisture Sensors x 2 (in Concrete Slab)
 - 20 mm (0.8 in.) below slab surface
 - 50 mm (2 in.) below slab surface
-  Relative Humidity Sensors, RHC x 2 (in Concrete Slab)
 - 20 mm (0.8 in.) below slab surface
 - 50 mm (2 in.) below slab surface
-  Relative Humidity Sensor, RHS (in Concrete Slab)
 - 20 mm (0.8 in.) below slab surface

Figure 2.3 (continued): Instrumentation of the ENV sections.

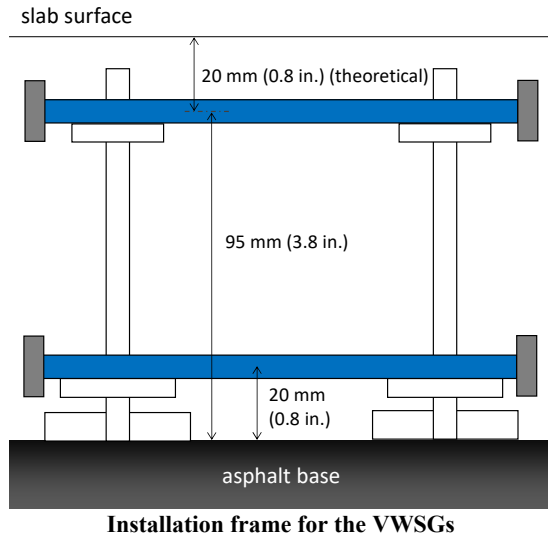


Figure 2.4: Vibrating wire strain gages (VWSGs).

The joint displacement measuring devices are LVDT-based sensors that measure slab movements. This type of sensor has long been used by the UCPRC (6). A set of nine JDMD sensors was installed in each of the 6×6 sections, six of them to measure corner deflection (vertical displacement), one to measure edge deflection, and two to measure the opening and closing of transverse joints. Section K was instrumented with seven JDMDs, while Section J was not instrumented with this type of sensor, as Figure 2.3 shows. In all these cases, the JDMDs measuring vertical displacements were attached to an arm rod fixture that was anchored in the subgrade (Figure 2.5). This anchoring system provided a relatively fixed reference (zero displacement) to measure slab deflections. Two pictures showing vertical and horizontal JDMDs are shown, respectively, in Figure 2.6 and Figure 2.7.

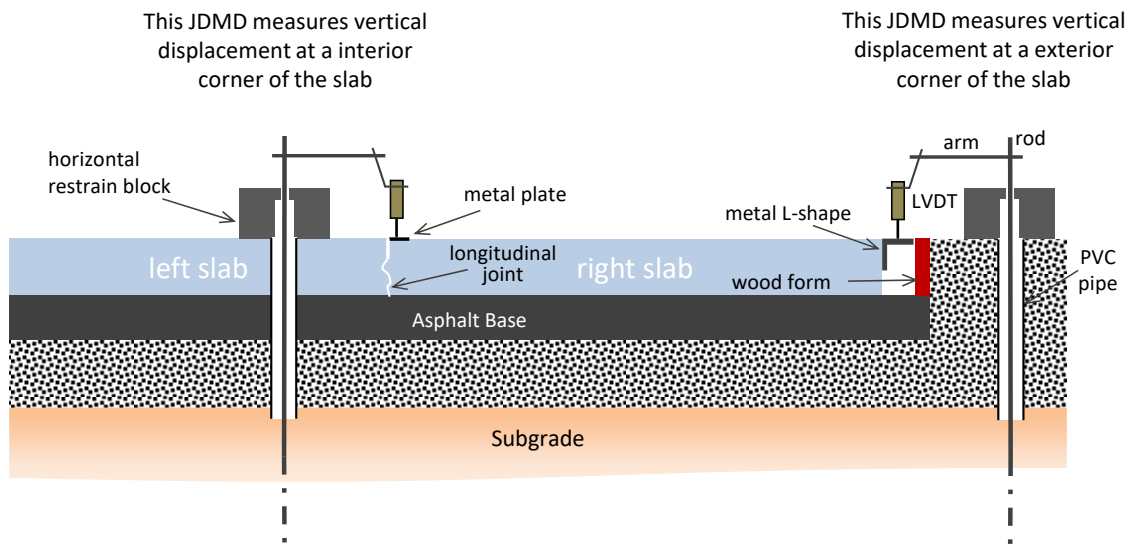


Figure 2.5: Anchoring system for vertical JDMDs.

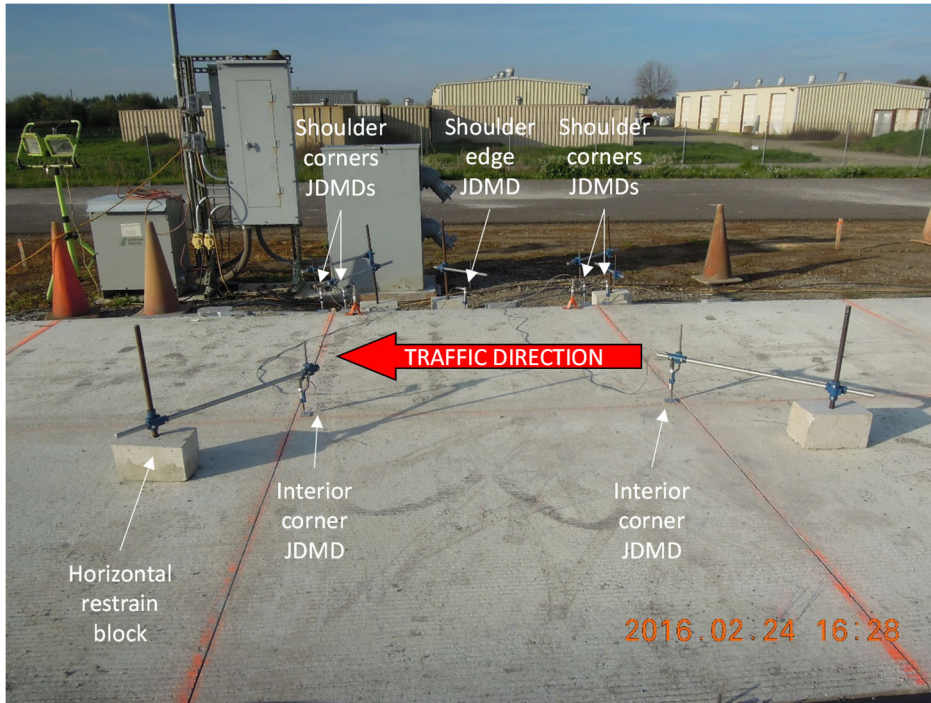


Figure 2.6: Example of vertical JDMDs (Section L).

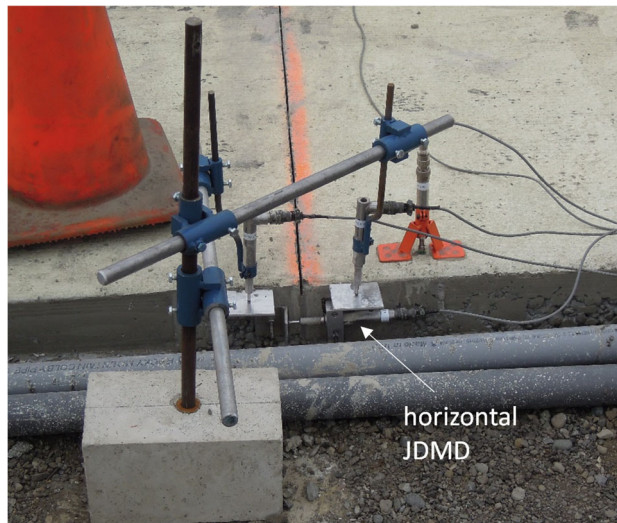


Figure 2.7: Example of a horizontal JDMD.

The interface-opening measuring devices are LVDT-based sensors that measure slab–base separation. The LVDT body of these sensors is fixed to the concrete slab, while the tip of the LVDT core rests on top of a metal rod anchored in the asphalt base (Figure 2.8). Figure 2.9 includes two pictures showing, respectively, the metal rod (before concrete placement) and the installed IOMD.

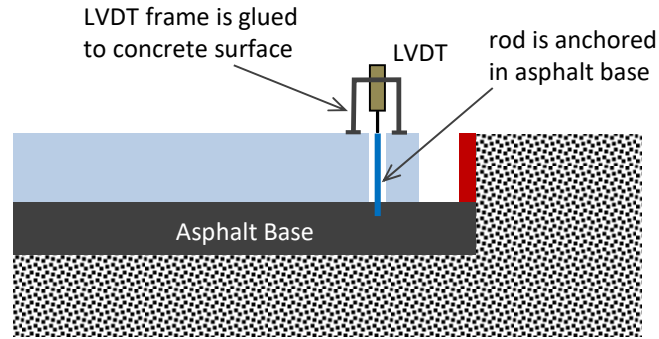


Figure 2.8: Anchoring system for IOMDs.



Figure 2.9: Interface opening measuring device (IOMD).
(Note: left side shows before concrete placement, right side after concrete placement.)

The ENV sections were also instrumented with thermocouples to monitor concrete and asphalt temperature at several depths (Table 2.1). Three locations of the middle slab of each section were instrumented: the slab center, an interior corner, and a corner at the shoulder. Thermocouples embedded in the concrete were attached to a fiberglass rod at the desired heights, as shown in Figure 2.10. The tip of the fiberglass rod, where the shallowest thermocouple was installed, was set at a depth of 5 mm (0.2 in.) using a tube-screw system to ensure that the rod tip would be at the correct distance from the surface of the concrete after placement of the overlay.

**Table 2.1: Thermocouple Depths
(measured from slab surface)**

5 mm (0.2 in.)
20 mm (0.8 in.)
50 mm (2 in.)
115 mm (4.5 in.) (bottom of concrete slab)
145 mm (5.7 in.) (asphalt base)

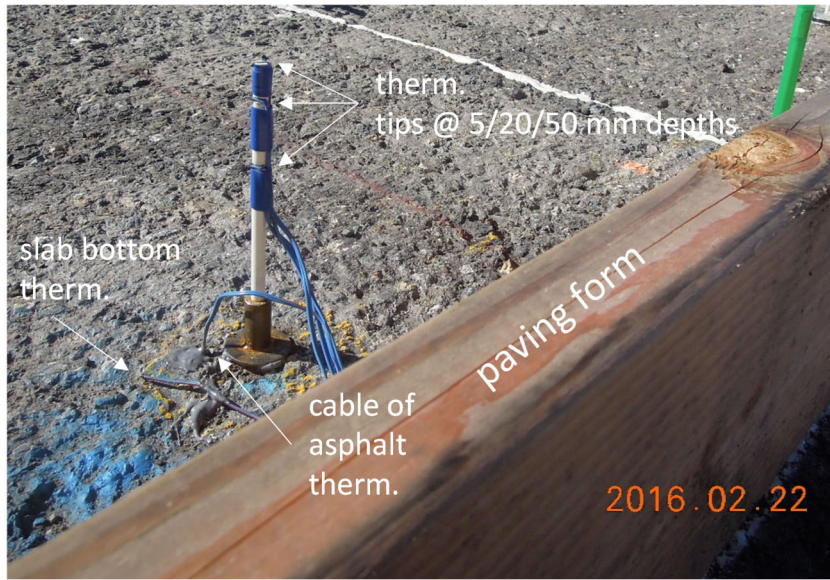
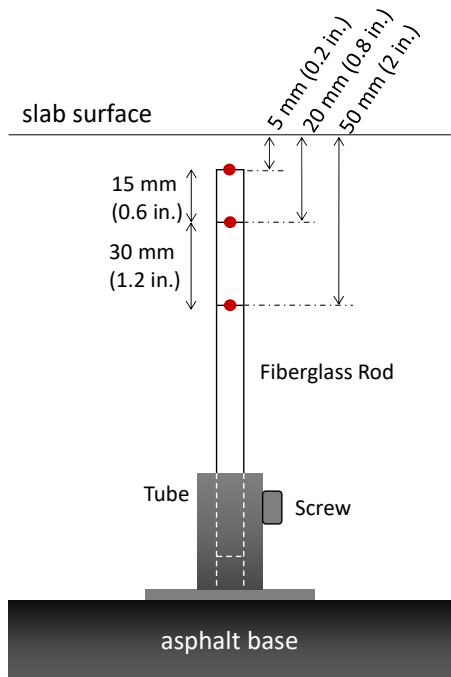


Figure 2.10: Installation of thermocouples embedded in the concrete.
(Note: right side shows before concrete placement.)

The relative humidity (RH) of the air in the concrete pores was measured using two types of sensors: the Campbell Scientific CS215-L and the Sensirion SHT75. In this report, these sensors are referred to as RHC and RHS, respectively. The actual sensor built into the former is also an SHT75 sensor. The main difference between RHC and RHS sensors is that the RHC incorporates signal conditioning, which significantly simplifies data acquisition. The RHC sensors were installed at the center of the middle slab of the sections. Two depths were instrumented: 20 and 50 mm (0.8 in. and 2.0 in.), as Figure 2.11 shows. The RHS sensors were installed in two locations of the middle slab of the sections: at the center of the slab and at an exterior corner, where more drying is expected due to moisture loss through the slab edge. RHS sensors were installed at a single depth, 20 mm (0.8 in.).

The moisture content (MC) of the concrete was measured using with SMT EMSs (Embedded Moisture Sensors). These sensors include a wooden part whose moisture content is measured and reported by the sensor. This moisture content can be regarded as an indirect indication of the moisture content of the concrete, but it is not the true moisture content of the concrete. These sensors were installed at the center of the center slab of the sections, at 20 and 50 mm (0.8 and 2.0 in.) depths, as Figure 2.11 shows.

RH and MC sensors were installed using the same chair used for the installation of the thermocouples. Figure 2.11 contains a diagram of the fiberglass installation frames and photographs of the sensors after installation, before concrete placement.

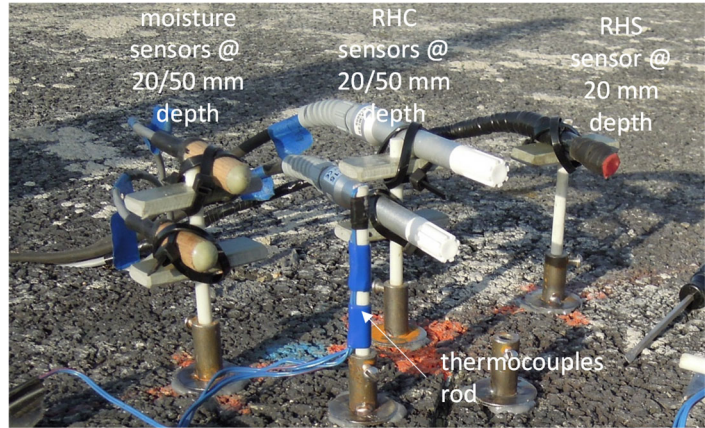
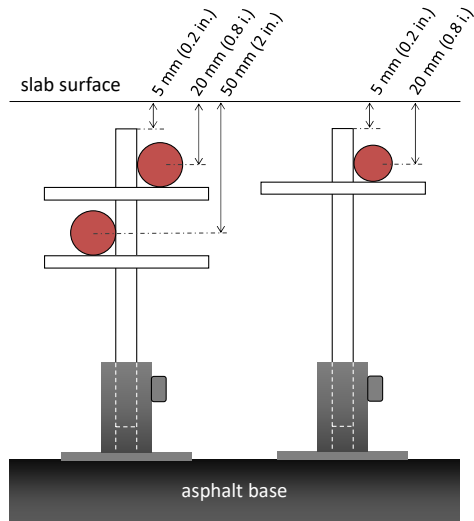


Figure 2.11: Relative humidity and moisture-content sensors.
 (Note: right side shows before concrete placement.)

Eight beams, 500×150×40 mm (18×6×1.6 in.), were fabricated during the overlay construction (Figure 2.12). The beams were fabricated using the same mixes that were placed in the BCOA sections and were cured under the same conditions as the BCOA sections. After the overlay construction, the beams were left outdoors by the test truck, so that both the BCOA sections and the beams could be subjected to the same environmental conditions. A vibrating wire strain gage was placed inside the mold of each beam so that concrete strain could be continuously monitored. These beams were used to measure the unrestrained expansion-contraction of the different concrete mixes since they were not bonded to any support.

2.3 Data Collection from the BCOA Environmental Sections

Three Campbell Scientific data acquisition systems (DAS) were used to collect the data on the environmental sections. In addition, National Instruments data acquisition systems on the two HVS units were used to collect LVDT data on Sections M and O. A summary of the data collection approach is presented below. Details of the data acquisition systems and further information about the data collection approach can be found in Reference (1).

With the exception of the LVDTs, data collection started the night before overlay construction, which was February 23, 2016, for Section L (test track Lane 1) and February 25, 2016, for Sections J, K, M, N, and O (test track Lane 2). Data collection for the LVDT-based sensors (IOMDs and JDMDs) started after overlay construction since the installation of these sensors is relatively time-consuming and cannot be conducted before saw-cutting operations. For Section L, JDMDs and IOMDs started to collect data around 6:00 p.m. the same day the overlay was placed. That was around eight hours after the concrete *field setting time*, which is defined in Section 3.4.2 of this report. For the rest of the sections (built on February 25), the JDMDs and IOMDs started to collect data the

day after overlay construction, which was around 24 hours (varying from section to section) after the field setting time of the different mixes.



VWSG inside the mold before placing concrete

- Beams 1 & 2: P2
- Beams 3 & 4: P2+SRA
- Beams 5 & 6: P2-ICC
- Beam 7: P3
- Beam 8: CSA



Beams after demolding

Note: curing compound was applied on the beams, as in the sections. SRA was also applied on top of two beams before curing compound spray.

Figure 2.12: Unrestrained shrinkage beams.

In the initial phase of data collection, the sampling interval was two minutes. After March 3, 2016, the sampling interval was set to five minutes, and it was set to 20 minutes after November 2016. The data analysis presented in this report uses one sample every 30 minutes during the first three days of data collection (February 23 to 25) and one sample every hour after that.

Data collection by the JDMDs and IOMDs was interrupted on May 13, 2016, because these sensors had to be removed to build the shoulders of the BCOA sections. They were reinstalled in Sections L and N in January 2017, although only the LVDT data collected during the initial phase (February to May 2016) have been analyzed and presented in this report. For the rest of the sensors (VWSG, RH, MC, and thermocouples), the data collected up to May 31, 2017, have been analyzed and presented in this report.

Environmental conditions, in particular air temperature, air relative humidity, rainfall, solar radiation, and wind speed, were measured by means of a weather station located by the test track.

2.4 Sign Criteria

This report uses the following convention for referring to strain: a positive value indicates an expansion and a negative value indicates a contraction. A baseline for strain was determined after concrete field setting time (FST), i.e., strain was assumed to be zero at the FST. The FST was determined for each of the environmental sections, as indicated in Section 3.4.2, based on visual examination of strain and temperature evolution after concrete placement.

This report uses the following conventions for referring to displacements: a positive value indicates upward vertical movement and a negative value indicates a downward vertical movement. This applies to the JDMDs that measure the vertical displacements of slab corners and edges. For the horizontal JDMDs that measure joint opening and closing and for the interface opening measuring devices that measure concrete-asphalt interface opening, a positive value indicates expansion and a negative value indicates contraction, the same conventions that have been used for the VWSG data. Both JDMD and IOMD displacements were determined after the installation time for the corresponding section, which was later than the corresponding FST.

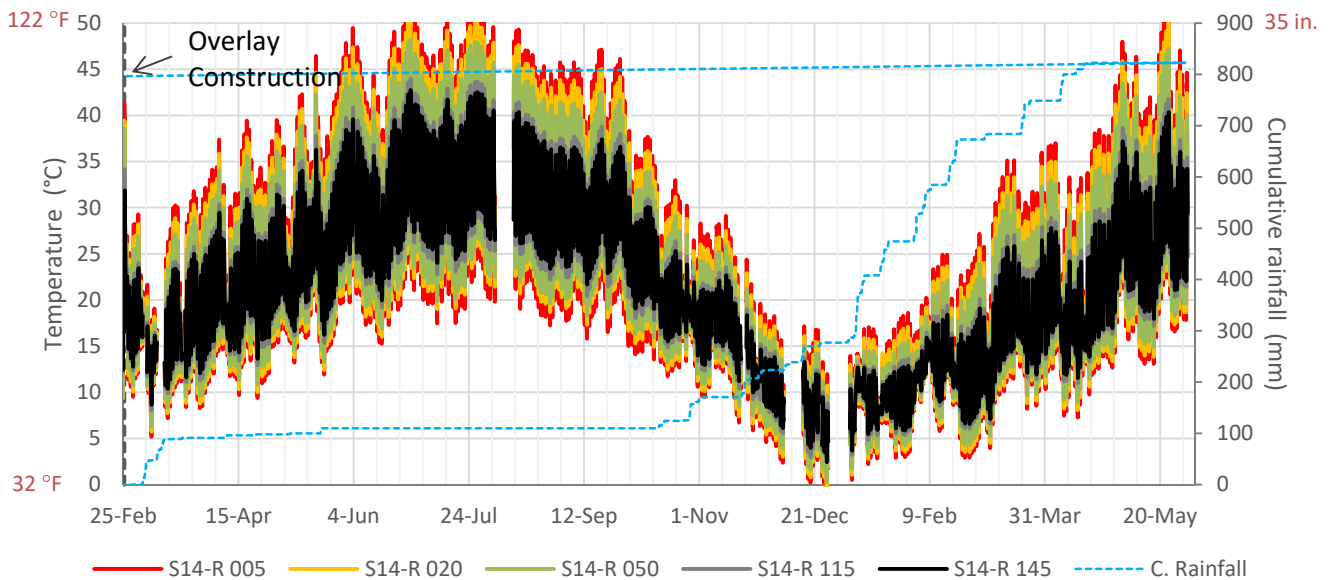
(This page intentionally blank)

3 ANALYSIS OF DATA COLLECTED FROM THE BCOA ENVIRONMENTAL SECTIONS

3.1 Data Collected by the Thermocouples

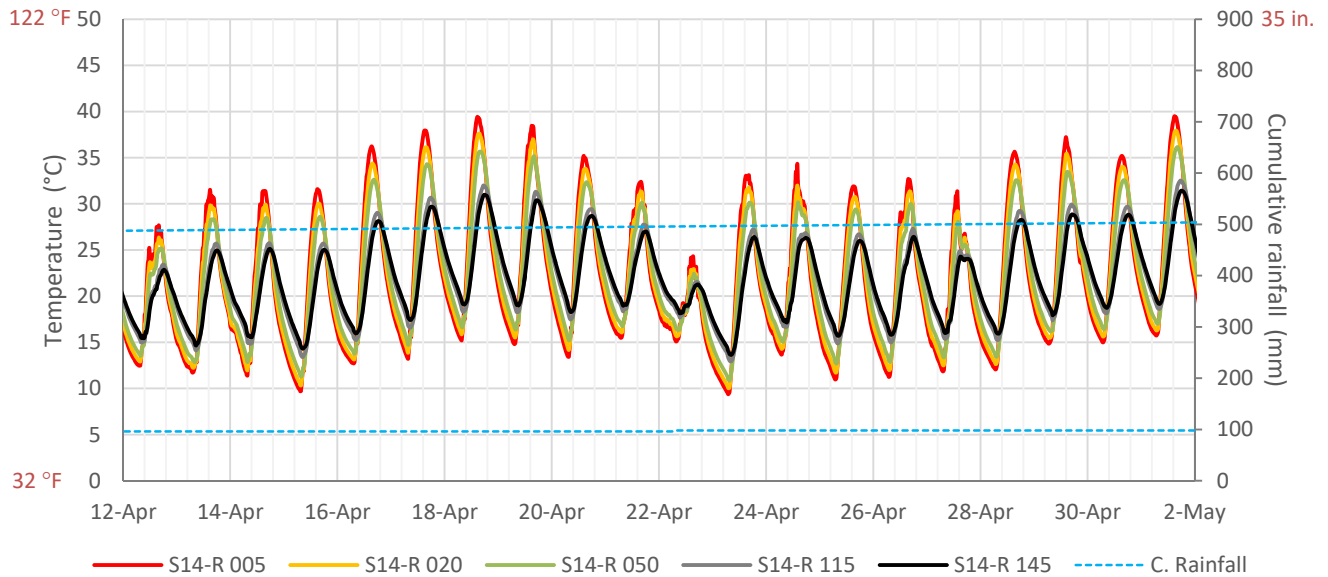
3.1.1 Examples of Collected Data

An example of data collected with the thermocouples is shown in Figure 3.1. This figure shows data collected at five depths (Table 2.1) at a specific location in Section M. Both seasonal and diurnal variations of the temperature are evident. As expected, diurnal temperature variation (maximum-minimum for each day) decreased with increased depth. Figure 3.2 shows the same data although for a narrower time interval. Diurnal variations of the temperature can be observed more clearly in this figure, together with the effects that rainfall events (and clouds) produce on slab temperature. The data gaps seen in Figure 3.1 are mostly related to the data acquisition system malfunctioning or to power outages.



Note: The three-digit number at the end of each sensor ID indicates the depth of the sensor in millimeters (mm).

Figure 3.1: Example of thermocouples readings (Section M, Slab 14, location -R).



Note: The three-digit number at the end of each sensor ID indicates the depth of the sensor in millimeters (mm).
Figure 3.2: Example of thermocouples readings: Detail of Figure 3.1 (Section M, Slab 14, location -R).

3.1.2 Data Analysis

The data from thermocouples were analyzed to determine the frequency distribution of temperature at different locations and other temperature-related variables, in particular, the *mean slab temperature* (TPCC) and the *equivalent linear temperature difference* (ELTD). In order to compute TPCC and ELTD, temperature was assumed to change linearly between each two thermocouples located at different depths. For example, temperature was assumed to change linearly versus depth between the values measured at 50 mm (2.0 in.) and 115 mm (4.5 in.) depth. The ELTD is defined as the temperature difference between the top and bottom of the slab which corresponds to the linear temperature gradient that will produce the same slab bending resulting from the slab’s current temperature profile. For this particular research project, the ELTD was determined by using the Momentum Equivalence approach (7).

It should be noted that some data have been discarded for some of the sections. The discarded data correspond to situations where the shadow projected by the HVS continuously affected an ENV section for more than a half hour. Because of the large volume of the HVS units, their shadows affected not only the specific section they were testing but the adjacent sections as well.

3.1.3 Preliminary Conclusions

Summary of Thermal Conditions of the Full-Scale BCOA Experiment

Figure 3.3 shows the cumulative distributions of three temperature-related variables: the temperature measured with the shallowest thermocouple (T005, measured at 5 mm [0.2 in.] depth), the mean slab temperature (TPCC), and the asphalt temperature (TAC, measured 30 mm [1.2 in.] below the slab bottom). In the three cases, values shown in Figure 3.3 are the average of all environmental sections during one year, from February 26, 2016, to February 26, 2017. The values shown in Figure 3.3 can be regarded an estimation of the temperatures that a 115 mm [4.5 in.] thick BCOA will be subjected to in California's Inland Valley² region. The temperature at 5 mm (0.2 in.) depth was between 3.7°C and 45.3°C 95 percent of the time. Similarly, the slab mean temperature was between 4.8°C and 41.9°C for that same percentage of time. The asphalt temperature was between 6.2°C and 38.1°C 95 percent of the time.

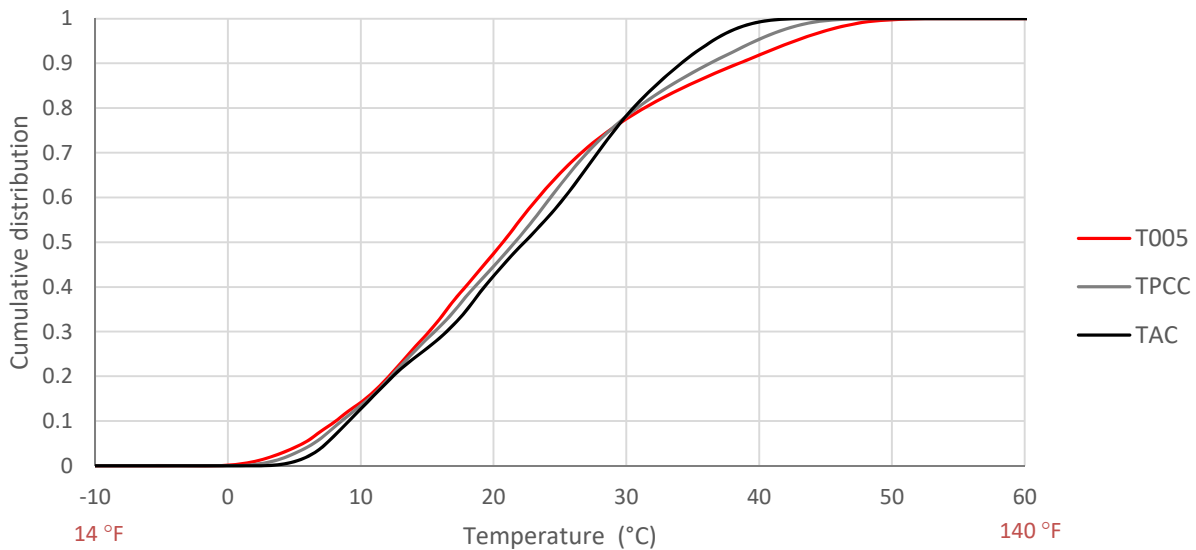


Figure 3.3: Temperature distribution during one year (Feb. 26, 2016 to Feb. 26, 2017, mean all ENV sections).

The frequency distribution of the ELTD is shown in Figure 3.4. Again, the values shown in the figure are the average of all environmental sections during the one year from February 26, 2016, to February 26, 2017. The ELTD was between -5.1 and 9.2°C 95 percent of the time.

² The Caltrans pavement climate regions map can be found online (8).

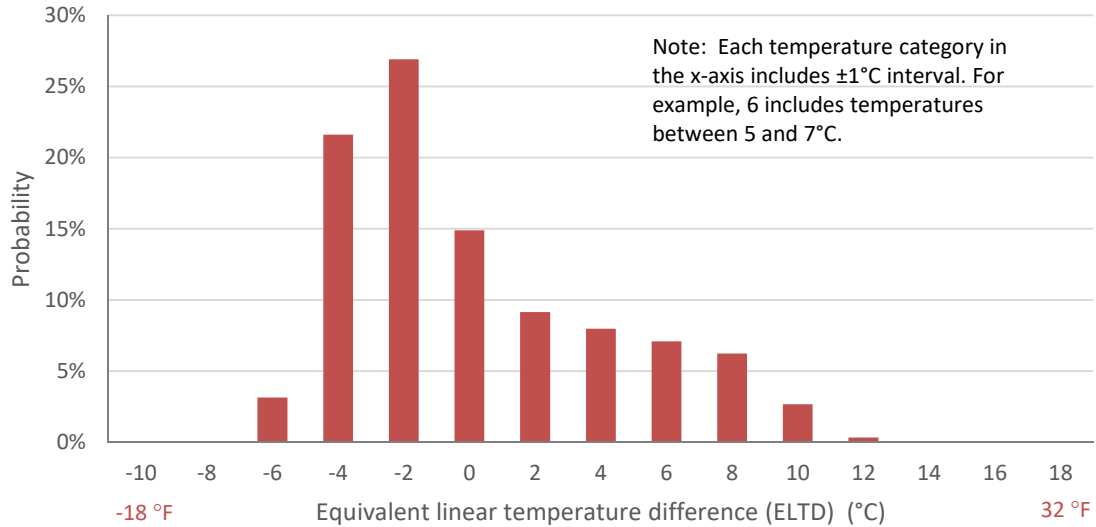


Figure 3.4: Frequency distribution of the ELTD during one year (Feb. 26, 2016, to Feb. 26, 2017, mean all ENV sections).

Temperature Differences from Mix to Mix

A preliminary analysis of the data collected with the thermocouples indicated some differences among sections, potentially related to the albedo of the different concrete surfaces. Albedo is the proportion of incident solar radiation that is reflected by a surface. The CSA and P3 mixes were lighter in color than the P2 mix and thus they had a higher capacity for reflecting solar radiation (higher albedo). The measured albedos were 0.44, 0.38, and 0.32 for the CSA, P3, and P2 mixes, respectively. The higher albedo of the CSA and P3 mixes resulted in less heating caused by solar radiation, and this resulted in lower maximum temperatures than those measured on the P2 mix. This can be seen in Figure 3.5, which shows the cumulative distribution of the temperature measured at 5 mm (0.2 in.) depth in the different ENV sections. Maximum temperatures in CSA and P3 sections (O and N) were around 4 to 5°C lower than in the P2 sections. This result is more clearly seen in Figure 3.6, where the average of all the mixes with Type II/V cement (P2 and P2-ICC) is plotted instead of the individual sections. Section L was not included in computing the average of the Type II/V cement mixes in Figure 3.6 because the distribution of the T005 temperature in this section was different from the rest of the sections with Type II/V cement. This difference was attributed to the fact that 65 days of Section L temperature data were discarded because of the effect of the HVS shadow (the HVS’s shadow affected Section L during testing of Sections D and E). As expected, the minimum temperature values in Figure 3.6 were similar for all the mixes since they tend to occur during nighttime and, consequently, they are not affected by the albedo.

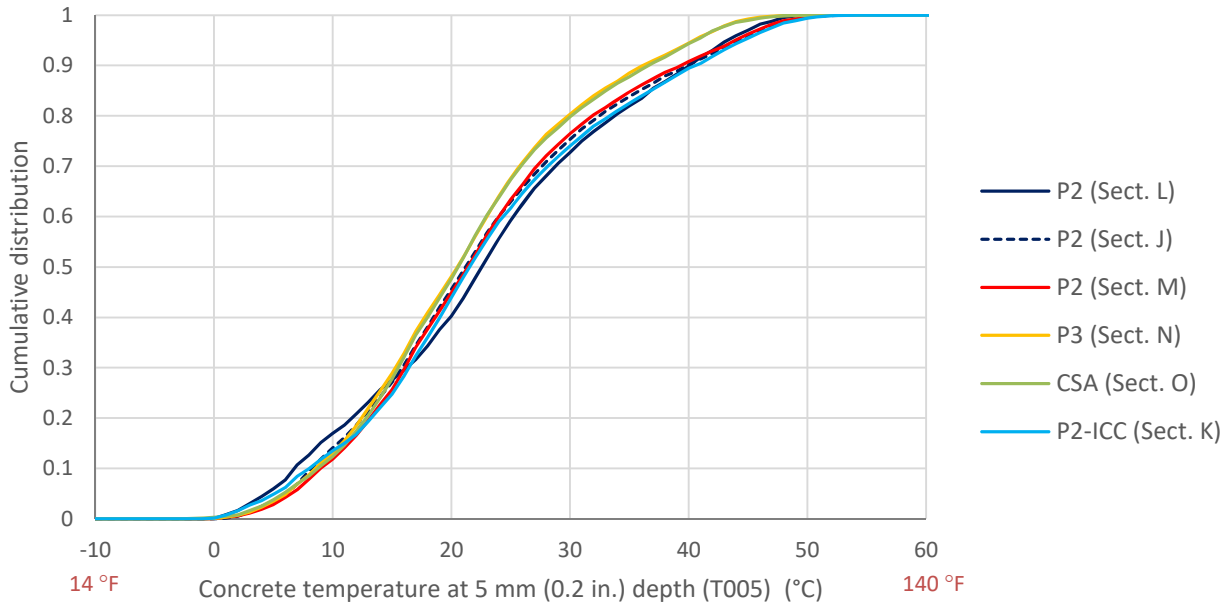


Figure 3.5: Distribution of concrete temperature at 5 mm (0.2 in.) depth, by section (Feb. 26, 2016 to Jan. 31, 2017).

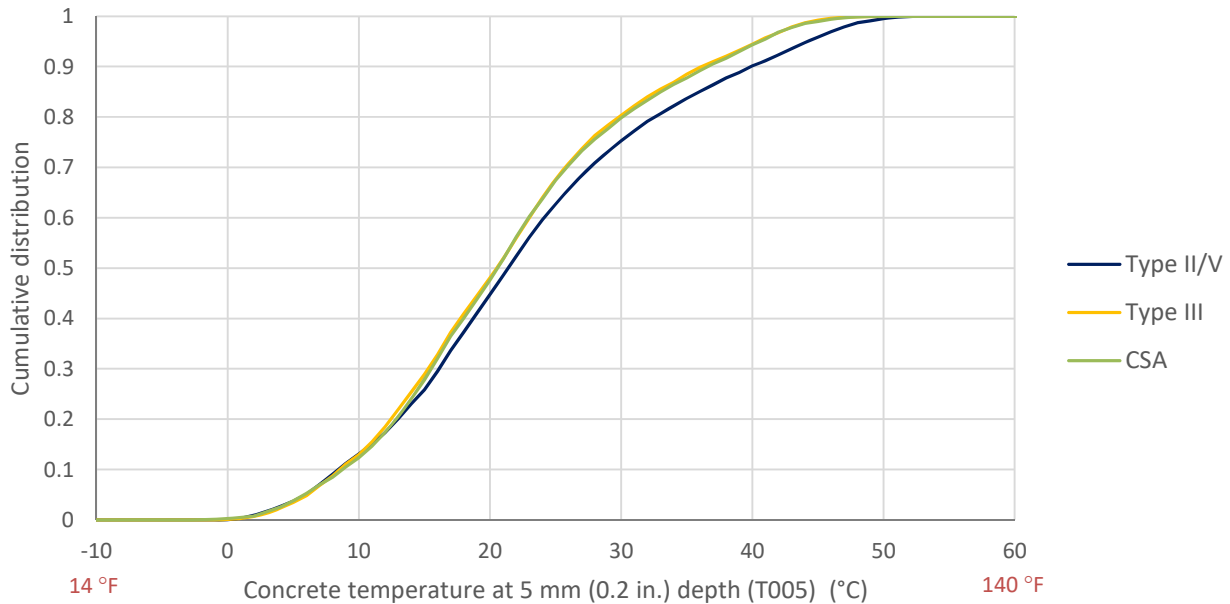


Figure 3.6: Distribution of concrete temperature at 5 mm (0.2 in.) depth, by cement type (Feb. 26, 2016, to Jan. 31, 2017).

It is not clear at this point why the P3 and CSA mixes yielded almost identical T005 temperatures in spite of having different albedos. This outcome might be related to the fact that concrete temperatures are not only determined by albedo, but by concrete density, heat capacity, and thermal conductivity too. The outcome might

be also related to incorrect depths of the thermocouples. As noted in Section 2.2, the tube-screw system used to install the thermocouples rod is believed to ensure a relatively correct distance from the surface of the concrete after placement of the overlay. Still, errors of a few millimeters (few in./10) can be expected and these errors may significantly affect temperatures recorded by the shallowest thermocouples. Nonetheless, the errors in thermocouples depths should have affected also the minimum temperatures, which did not seem to have happened (Figure 3.6).

The albedo effect is also clear at locations deeper than 5 mm (0.2 in.) since the mixes with Type II/V cement presented higher TPCC (mean slab temperature) and TAC (asphalt temperature) than the mixes with CSA and Type III cements, as can be seen in Figure 3.7 and Figure 3.8. This outcome is due to the fact that the latter mixes (with Type III or CSA cements) had higher albedo than the former mixes (with Type II/V cement).

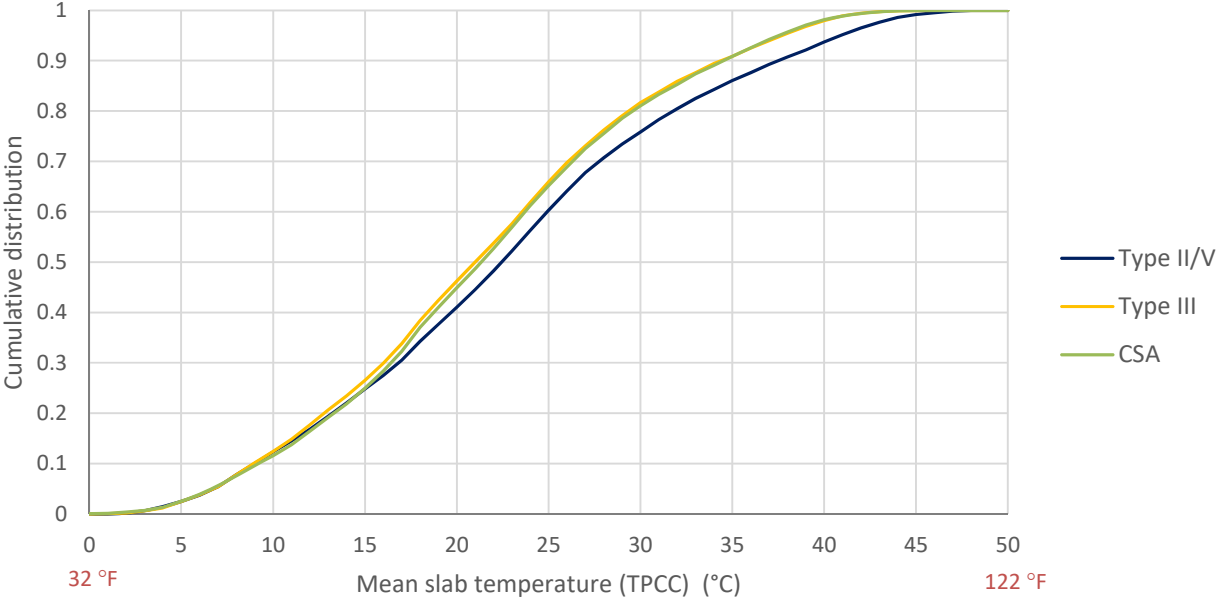


Figure 3.7: Distribution of mean slab temperature, by cement type (Feb. 26, 2016 to Jan. 31, 2017).

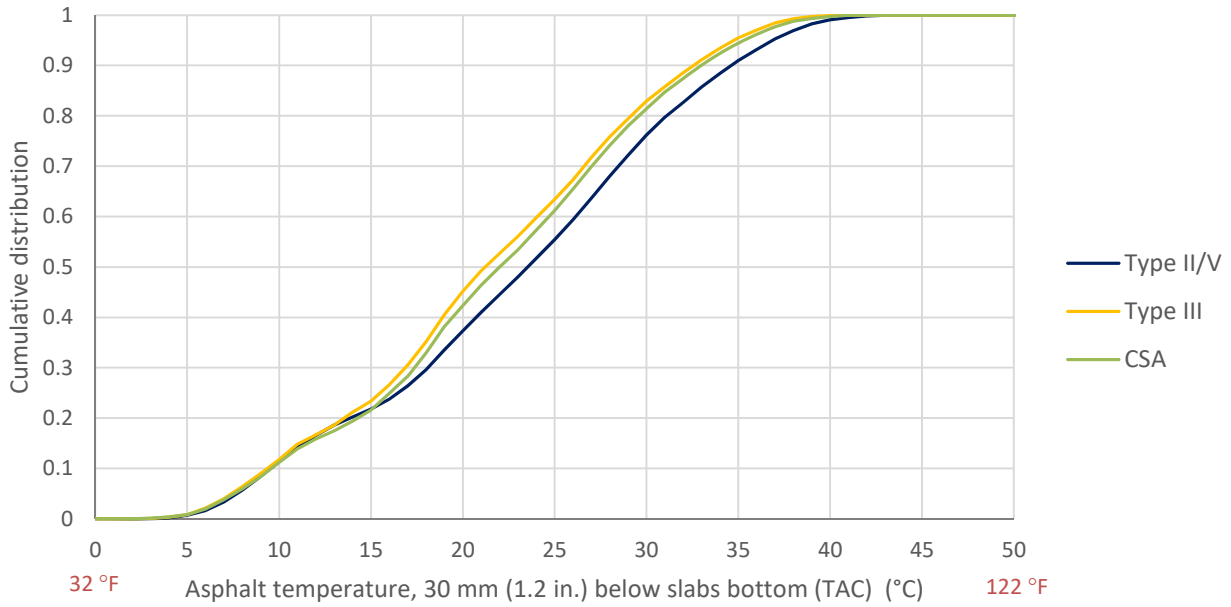


Figure 3.8: Distribution of asphalt temperature, by cement type (Feb. 26, 2016, to Jan. 31, 2017).

As expected, the albedo effect resulted in higher daytime (positive values) ELTD in sections with Type II/V cement compared to sections with Type III or CSA cements (Figure 3.9).

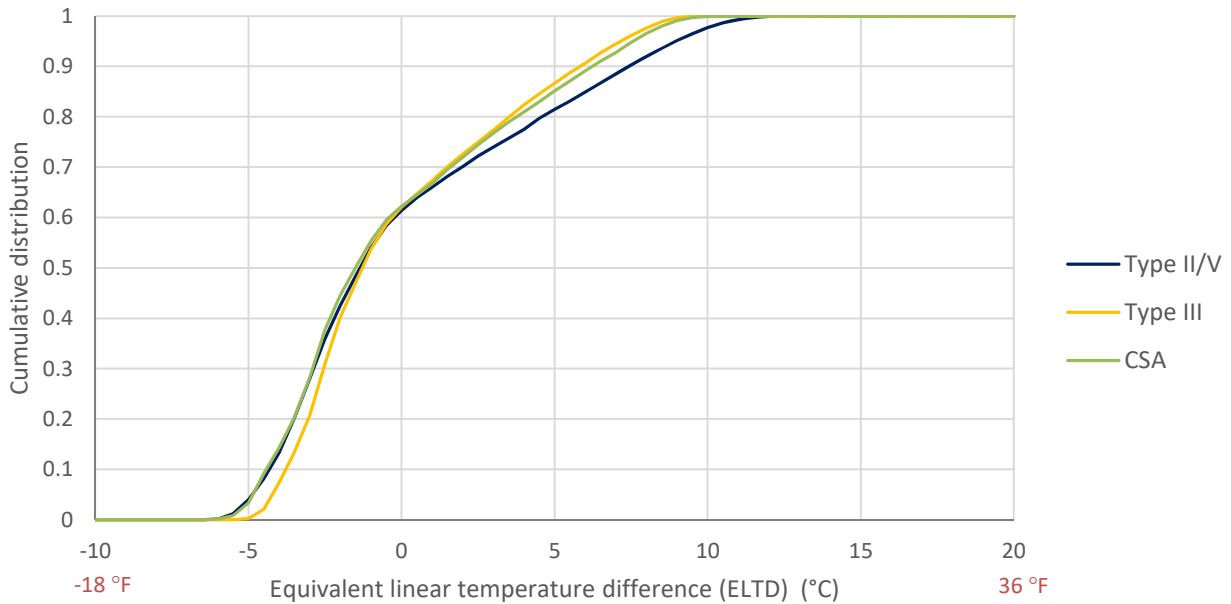
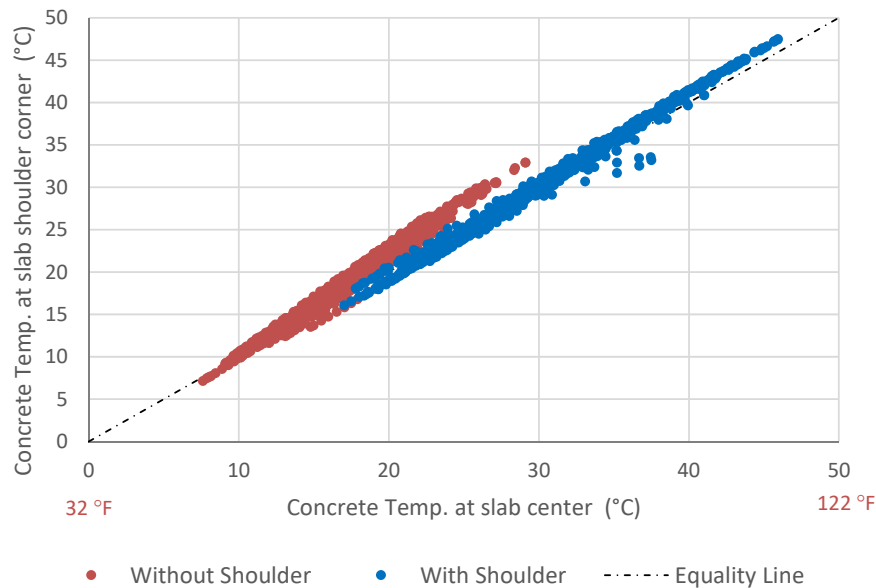


Figure 3.9: Distribution of ELTD, by cement type (Feb. 26, 2016 to Jan. 31, 2017).

It should be noted that the time interval used to produce the data in Figure 3.5 through Figure 3.9 is not exactly one year, since it extends from February 26, 2016, to January 31, 2017. The shortened time interval is due to the need to discard the data for February 2017 because Sections J, K, and L were affected by the shadows cast by the HVS units. This is not considered a limitation of the analysis presented above since the conclusions were based not on the absolute values of the temperature distributions, but on the comparison of the different mixes to one another.

Effect of Shoulders on Slab Temperature

In order to evaluate the effect of the shoulder on slab temperature, the temperature records measured at the slabs’ center were compared to those measured at the slabs’ shoulder corner. This comparison was conducted for the five environmental sections located in Lane 2 (J, K, M, N, and O). The shoulder edge of the slabs for these sections was located in the south, as shown in Figure 1.1. However, before construction of the granular shoulders in April and May 2016, this edge received direct radiation from the sun. For this reason, the comparison considered two time periods: the first one before shoulder construction (between February 27 and April 15), and the second after shoulder construction (between May 15 and June 30). The results of the comparison for the two time periods appears in Figure 3.10. As expected, before shoulder construction the temperatures measured at the shoulder edge were higher than those at the center of the slabs. These differences were considerably reduced after shoulder construction.



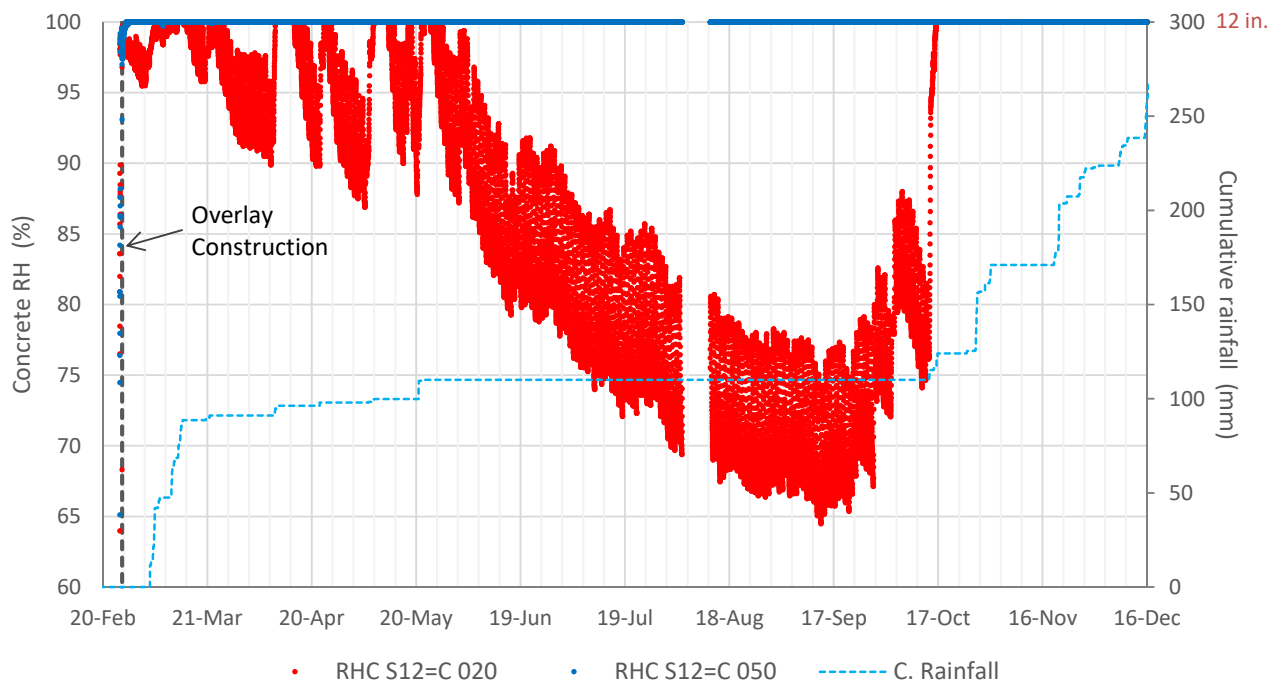
Note: Each point on the graph is the average of four depths (5, 20, 50, 115 mm) and five environmental sections, all in Lane 2.

Figure 3.10: Effect of the shoulder on slabs edge temperature.

3.2 Data Collected by the Relative Humidity Sensors

3.2.1 Examples of Collected Data

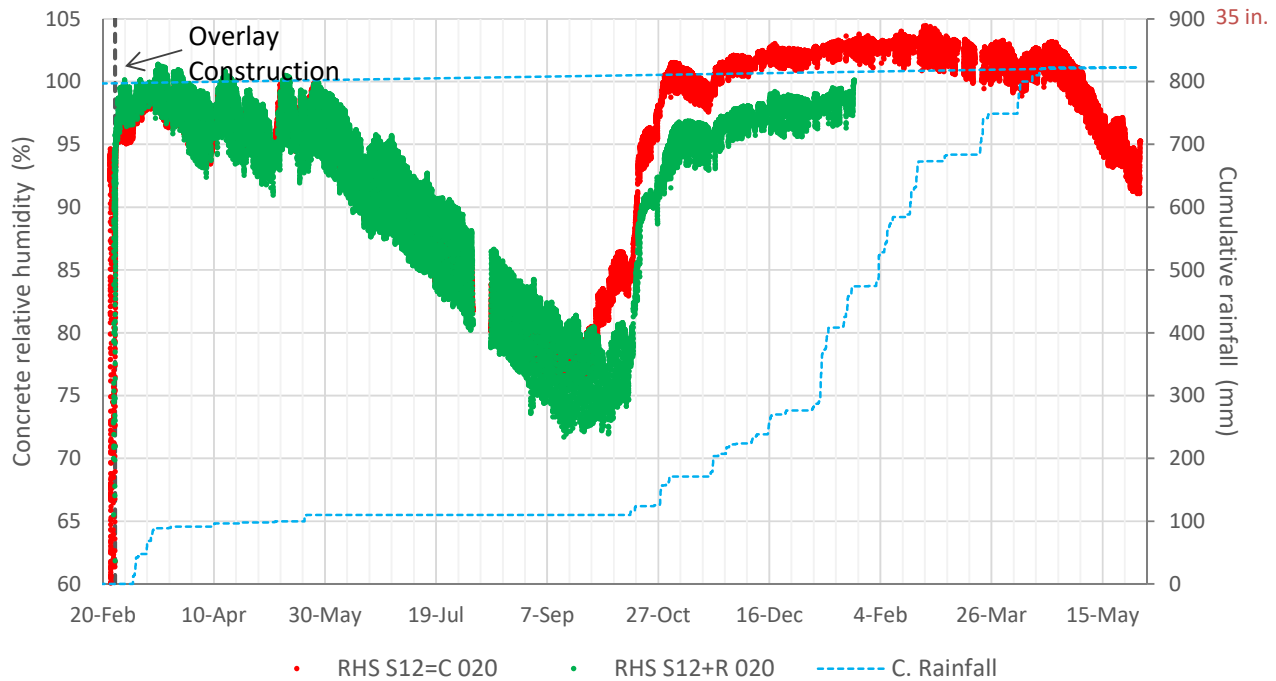
The relative humidity (RH) of the air in the concrete pores was measured using two types of sensors: the Campbell Scientific CS215-L and the Sensirion SHT75, referred to as RHC and RHS, respectively. Examples of data collected with the two types of RH sensors are presented in Figure 3.11 and Figure 3.12 for RHC and RHS sensors, respectively. Both sensor types sensors, when located at 20 mm (0.8 in.) depth, clearly show that drying takes place during periods with no rainfall and that moisture increases after periods of rainfall. These RH data also reflect diurnal changes related to temperature fluctuations.



Note: The three-digit number at the end of each sensor ID indicates the depth of the sensor in millimeters (mm). The two sensors are located at the center of the Slab 12 (=C).

Figure 3.11: Example of readings from RHC sensors at the center of the slab (Section N).

It should be noted that the RHC data in Figure 3.11 extend to December 31, 2016, while RHS data in Figure 3.12 extend to May 31, 2017 (end of the time interval analyzed in this report). The reason for this time difference is that RHC sensors stopped functioning well at the beginning of 2017, and by May 31, 2017, none of them worked properly. On the other hand, only two of the twelve RHS sensors failed before May 31, 2017. One of the RHS sensors that failed was RHS.N.S12+R.020, which corresponds to the green series in Figure 3.12.



Note: The three-digit number at the end of each sensor ID indicates the depth of the sensor in millimeters (mm). One of the sensors (red series) is located at the center of the Slab 12 (=C) and the other (green series) is located at a corner (+R).
Figure 3.12: Example of readings from RHS sensors at the center of the slab (Section N).

Both Figure 3.11 and Figure 3.12 show a gap of data at the beginning of August 2016. This data gap is the result of a power outage that affected all the data acquisition systems.

3.2.2 Data Analysis

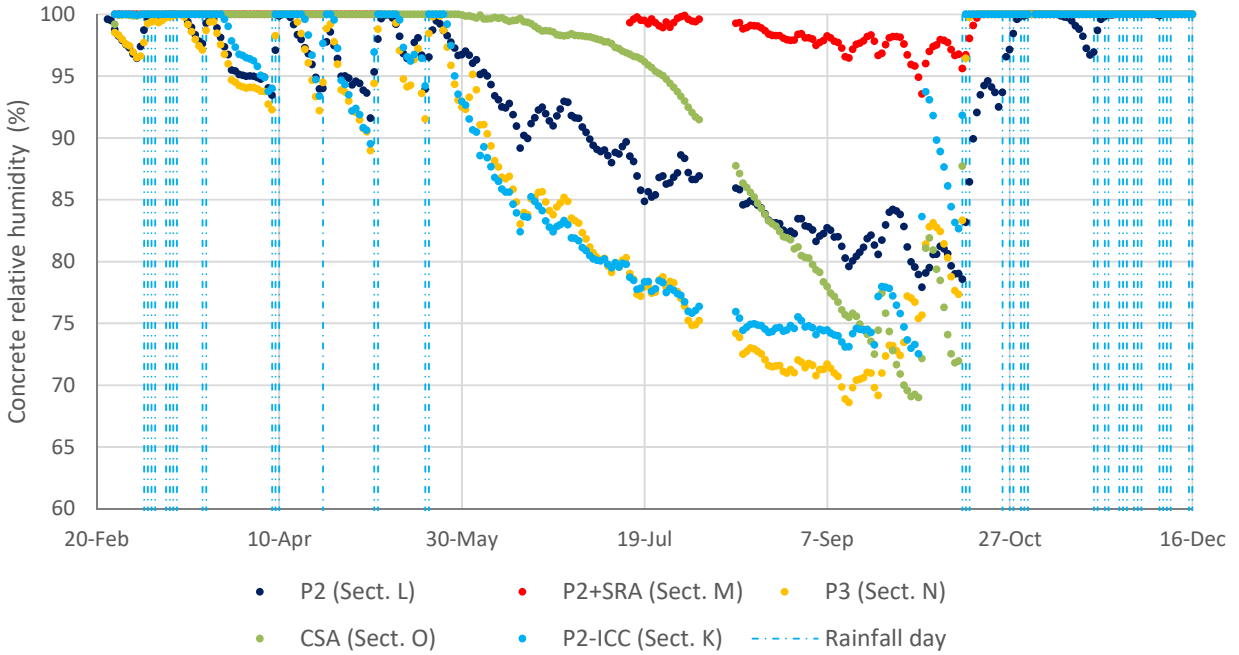
In order to conduct a preliminary analysis of the RH data, daily mean values (i.e., the mean of all the readings for a day) were computed for all the sensors. These data are the basis for part of the preliminary conclusions presented below.

RH data were also analyzed to quantify diurnal variations of the RH as a function of temperature, $\Delta RH/\Delta Temp$.

3.2.3 Preliminary Conclusions

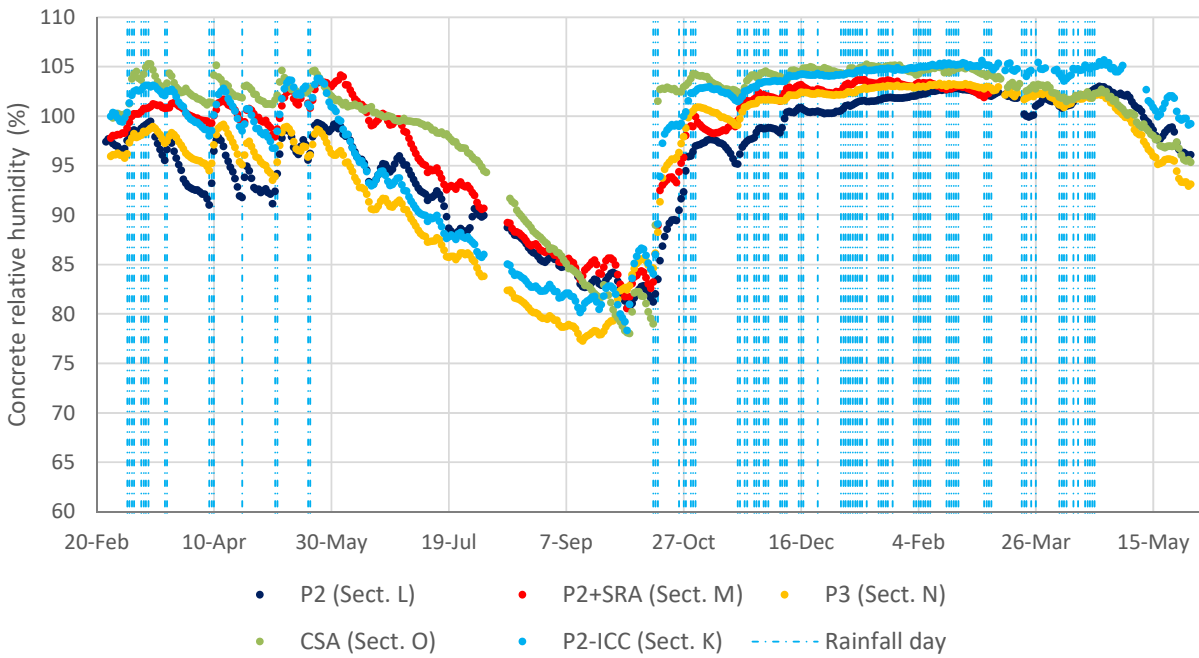
Ranking of Mixes and Curing Procedures Based on Concrete Relative Humidity

The data shown in Figure 3.13 and Figure 3.14, for RHC and RHS sensors respectively, make it possible to rank the mixes and curing procedures in terms of drying susceptibility. As noted in Section 2.1, all the sections were cured with standard curing compound except Section M, which was cured with a shrinkage-reducing admixture (SRA) solution prior to the application of the curing compound.



Note: Each point in the graph is the mean value of RH values measured in one day.

Figure 3.13: Relative humidity measured by RHC sensors at slab center at 20 mm (0.8 in.) depth.



Note: Each point in the graph is the mean value of RH values measured in one day.

Figure 3.14: Relative humidity measured by RHS sensors at slab center at 20 mm (0.8 in.) depth.

Overall, the CSA mix had the highest internal RH values. Both the RHC and RHS sensors showed that the relative humidity values for this mix were higher than for the other mixes most of the time. Specifically, the sensors in the CSA mix at 20 mm (0.8 in.) depth showed no evidence of drying until June 2016, when both sensor types started to indicate drying. This result is in line with the low drying shrinkage that has been reported for concrete using CSA cement (4). There is a caveat to the good drying performance of the CSA mix: its rate of drying during summer 2016 was higher than the rate of drying in the portland cement-based mixes. As a result, the CSA mix, along with P3 and P2-ICC mixes, presented the lowest RH among all mixes at the end of summer 2016 (Figure 3.13 and Figure 3.14).

The P2 mix cured with SRA (Section M) had very good performance against drying compared to the same mix cured with curing compound. The RHS sensor at 20 mm (0.8 in.) depth in Section M showed no evidence of drying until June, approximately the same time that the CSA mix started to show evidence of drying (Figure 3.14). The same conclusion was reached based on RH data measured with RHS sensors at the slab shoulder corners (Figure 3.15). The SRA effect is evident when Section M RH data are compared to Section L, in both Figure 3.14 and Figure 3.15. This outcome is in line with experimental studies showing that SRA decreases the surface tension of fluid in capillary pores, in addition to affecting other fluid properties such as viscosity, contact angle, and density, resulting in the alteration of absorption and desorption processes in the concrete (9). According to Reference (9), the presence of the SRA results in a shallow drying front, a few millimeters in depth (few tenths of an inch). Below this drying front, the degree of saturation of SRA-treated concrete is expected to remain at relatively high levels. Because of this high degree of saturation and because of the reduction of the surface tension of fluid in the concrete pores, RH is expected to be higher in SRA-treated concrete than in its untreated counterpart. Unfortunately, the RHC sensor at 20 mm (0.8 in.) depth in Section M stopped working properly in May 2016. Until May, however, this sensor had been recording 100 percent RH at all times. This sensor seemed to start to work properly in July 2016 (Figure 3.13), and it reported very high RH values in the P2 mix cured with SRA compared to the other mixes. These high RH values must be considered cautiously, since it is not clear if the sensor was working properly.

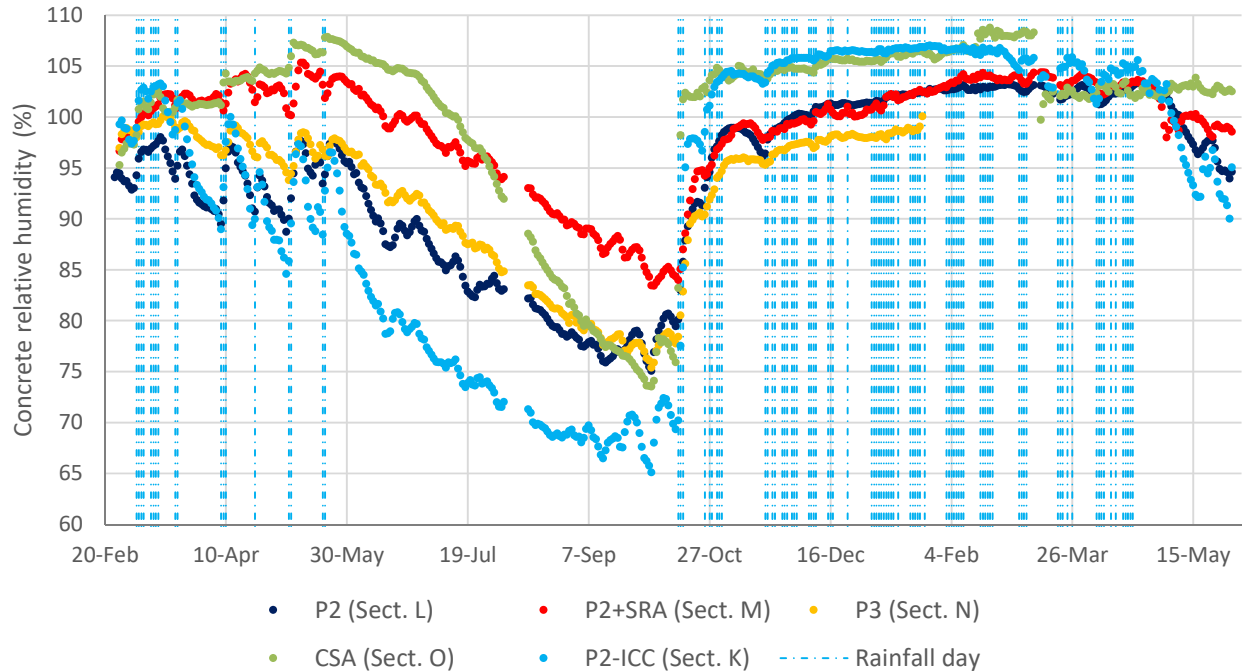


Figure 3.15: Relative humidity measured by RHS sensors at slab shoulder corners at 20 mm (0.8 in.) depth.

Data from both the RHC and RHS sensors agreed that the P3 and P2-ICC mixes had the lowest RH values. At the end of September 2016, the RHC sensors located at the slab centers indicated relative humidity values for both mixes to be around 70 to 75 percent, while the RHS sensors at the same location indicated values around 80 percent. The RHS sensors located at slab shoulder corners indicated RH values around 65 and 75 percent, respectively, for P2-ICC and P3 mixes.

Both the RHC and RHS sensors agreed that the P2-ICC presented higher relative humidity values than the P2 mix during an initial phase, but that it also had a higher rate of RH decrease during periods without rainfall. It was a surprise that P2-ICC presented worse drying performance than the P2 mix upon which its design is based. In fact, some studies showed the opposite performance (10). In theory, the water supplied by the pre-wetted lightweight aggregates (LWA) should have resulted in a lower drying shrinkage for two main reasons. First, this water serves as a reservoir that replenishes water lost through internal desiccation (the main goal of internal curing) and evaporation. Second, the increase in the degree of cement hydration was expected to reduce the porosity of the concrete, thus reducing water loss through evaporation.

In this particular project, this improvement in drying shrinkage performance was verified for the P2-ICC only in an initial phase, as can be seen in Figure 3.13, where the P2-ICC RHC sensor at 20 mm (0.8 in.) depth showed no evidence of drying during the first month after construction. It can be also observed in Figure 3.14 and Figure 3.15,

where the RHS sensors report higher RH in the internally cured mix than in the P2 mix for a few weeks after BCOA construction. This result is likely related to the water internally supplied by the pre-wetted LWA. After this initial period, drying affected this mix more than it affected the P2 mix. This outcome is likely related to the relatively low flexural strength this mix presented compared to the P2 mix, as shown in Reference (1). It is possible that the actual water content of the P2-ICC mix was higher than intended, and this would explain the relatively large decrease in the flexural strength of the P2-ICC compared to the P2 mix upon which its design is based. The 10-hour flexural strength of the P2-ICC mix used for construction of the BCOA sections was around 30 percent lower than the flexural strength of the P2 mix. This decrease in flexural strength was higher than the roughly 10 to 20 percent values that were obtained in preliminary laboratory tests. A relatively high water–cement ratio would also result in a higher porosity compared to the P2 mix, which would explain the higher drying susceptibility. This higher-than-intended water content may or may not have been related to the LWA. If the lightweight aggregates were correctly preconditioned, the water in their pores would only be released when desiccation took place, so this amount of water would not increase the water–cement ratio of the mix (10).

Effect of Environmental Conditions on Concrete Relative Humidity

As shown in Figure 3.13, the RH measurements taken at 20 mm (0.8 in.) depth clearly show the drying that takes place during periods without rainfall and the wetting after rainfall events. One of the main conclusions that can be drawn from these data is that rainfall events produced an almost immediate increase in relative humidity at this depth. Although the analysis method applied to the RH data cannot quantify the speed of this reaction, it does show, however, that the increase in RH at 20 mm depth (0.8 in.) is noticeable just a few hours after rain falls and that the RH increase will continue for several days.

Another interesting observation from Figure 3.13 is that the increase in RH after the rainfall events does not seem to be related to the amount of precipitation. For example, the amount of precipitation during April 8 to 10 (5 mm [0.2 in.]) was roughly three times the amount of precipitation from May 6 to 7 (1.8 mm [0.07 in.]). Nevertheless, both periods of rainfall produced a similar increase in RH. In fact, the increase in RH because of the second, smaller rainfall (May 6 to 7) was slightly larger than the increase due to the first one. This was probably because the concrete was dryer and, in both cases, RH increased to 100 percent. As expected, the effect of rainfall on RH is related to the amount of water the concrete can absorb. Additional precipitation beyond a minimum threshold value does not entail a further increase in the concrete’s relative humidity. Similar conclusions can be drawn from RH measurements with the RHS sensors (Figure 3.14 and Figure 3.15). These observations will have an impact for predictions of drying shrinkage for a couple of reasons. First, it does not seem that drying shrinkage can be predicted on the basis of air relative humidity exclusively as is done in the MEPDG (11) and Hiperpav (12)

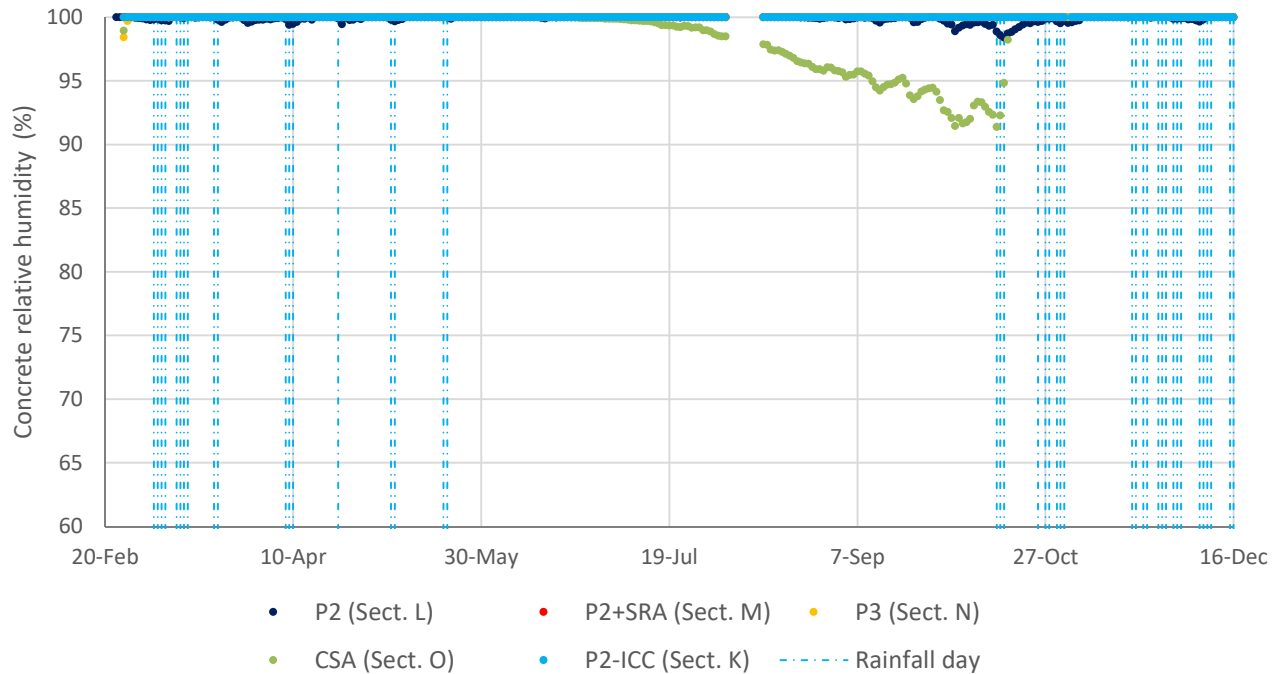
approaches. This is because although air relative humidity may be the main factor that governs drying, it is the rainfall regime that will determine wetting. Second, as far as rainfall is concerned, its distribution throughout the year may be as important, or even more important, than the annual amount of precipitation.

It should be noted that in Figure 3.13 all the RHC sensors at 20 mm (0.8 in.) depth showed an increase in RH after October 3, 2016. The UCPRC weather station (located by the test track) did not record any rainfall that day, although the solar radiation recorded indicate that it was a cloudy day. Further, the UC Davis weather station located about one mile from the test track reported 0.8 mm (0.03 in.) rainfall that day. It is believed a small rainfall may also have taken place at the test track but the UCPRC weather station was unable to capture it.

Concrete Self-Desiccation

Figure 3.16 shows the relative humidity measured with RHC sensors at 50 mm (2.0 in.) depth for the different mixes and curing procedures. All the sensors reported 100 percent RH (or close) for a few months after the overlay construction, i.e., the sensors did not show self-desiccation for any of the mixes. Nonetheless, internal desiccation due to the cement hydration process (self-desiccation) was expected for the P2 and P3 mixes due to the low water/cement ratio of these mixes, which were 0.33 and 0.31, respectively. Concrete self-desiccation was also expected for the P2-ICC, although less than in the P2 and P3 mixes. As Figure 3.16 shows, almost no self-desiccation was measured in any of these mixes. However, it is very likely that self-desiccation did take place, at least in the P2 and P3 mixes, but the RHC sensors were unable to capture it. No RHC sensor was located at 50 mm (2.0 in.) depth, so it is unknown whether or not these sensors would have been able to capture concrete self-desiccation.

Figure 3.16 also shows that the RHC sensor at 50 mm (2.0 in.) depth in the CSA section started to show drying in July 2016. It is evident this drying is not related to the cement hydration process but to external drying caused by warm and dry weather conditions during the summer.

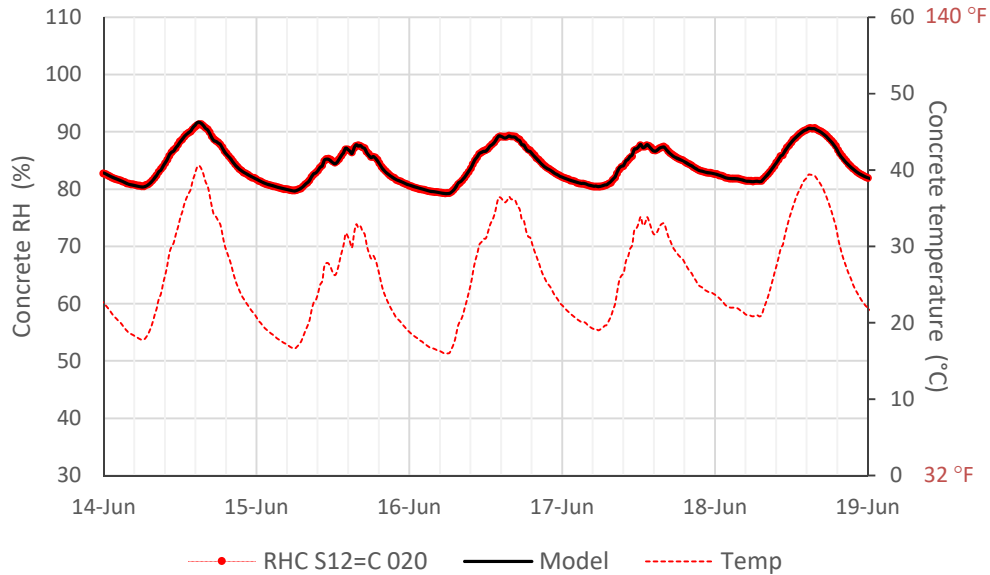


Note: Each point in the graph is the average of RH values measured in one day.

Figure 3.16: Relative humidity measured by RHC sensors at slab center at 50 mm (0.8 in.) depth.

Diurnal Variations of Concrete Relative Humidity

The relative humidity data in Figure 3.11 (RHC sensors) and Figure 3.12 (RHS sensors) reflect diurnal variations related to temperature changes. The link between these variations and temperature is easy to verify by observing both variables' evolution for a single day without rainfall. For example, Figure 3.17 shows the evolution of RH over five days, together with a simple model where RH is a linear function of temperature. The agreement between measured RH and the model is clear, which indicates that the changes in relative humidity are directly or indirectly related to changes in temperature. It should be noted that the RH in concrete air pores increases as temperature increases, which is the opposite of a scenario where the amount of water vapor in the air is constant. For constant water vapor in the air, the RH decreases as temperature increases because the RH is the ratio between water vapor pressure (in the air) and the equilibrium water vapor pressure, and the latter increases as temperature increases. Because equilibrium water vapor pressure increases with temperature, RH in the open air typically decreases as temperature increases. The opposite occurs in concrete air pores. The relationship between RH in concrete air pores and temperature has been described before (13). Reference (13) hypothesizes that this relationship is due to a number of phenomena that result in temperature-dependent changes in the RH of concrete air pores while the amount of water content in the concrete remains constant. This topic and its implications for pavement design have been studied as part of this Caltrans research project and the study is included in Reference (2).



Note: The model assumes RH has a fixed term (constant within one day) plus a variable term that is a linear function of the temperature: $RH = RH(25^{\circ}C, \text{day}) + KT \cdot (Temp - 25^{\circ}C)$. The model's parameters (RH at 25°C, for each day, and the proportionally factor KT), were determined through an error minimization iterative process.

Figure 3.17: Example of diurnal variations of RH (Section N).

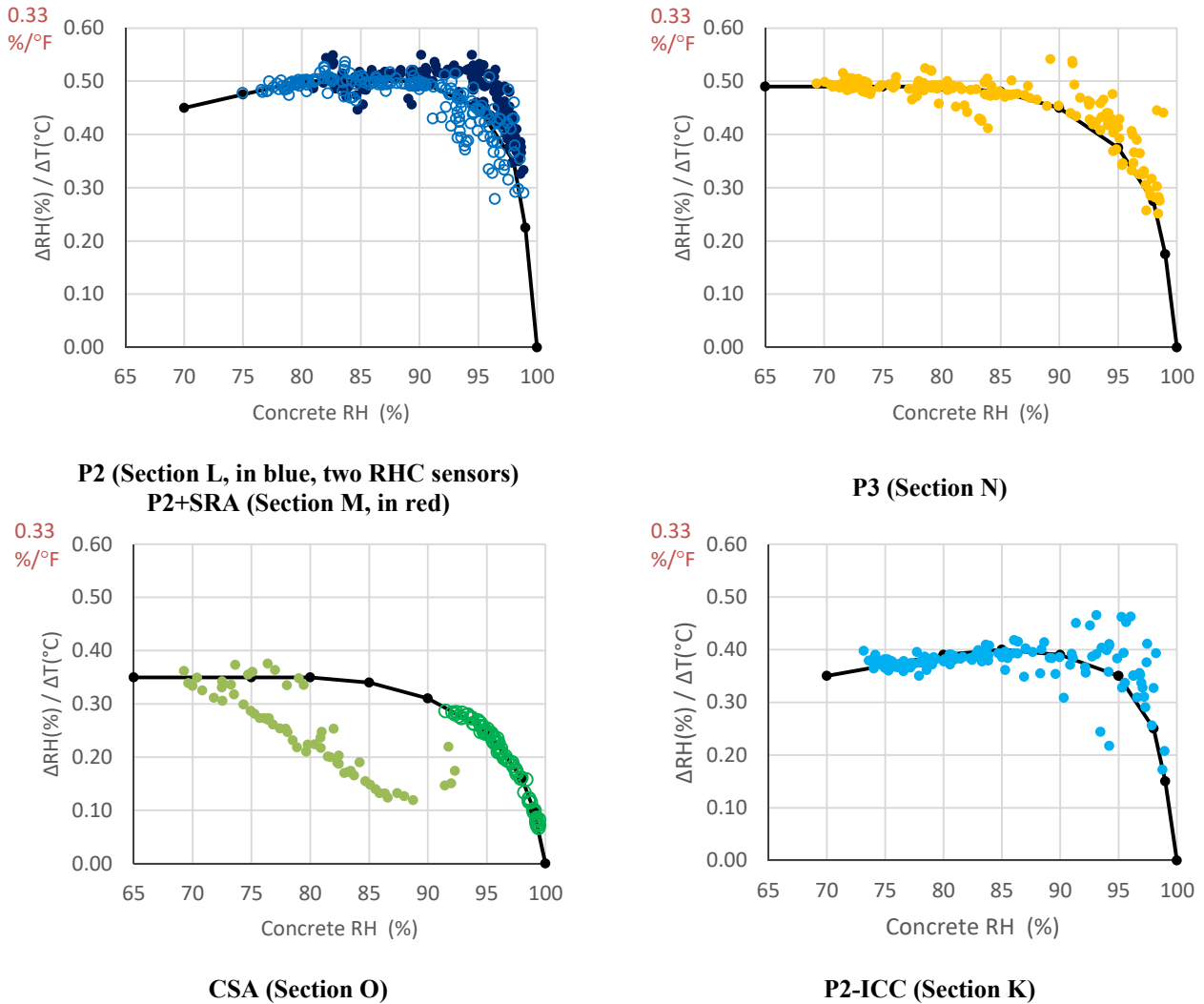
The change in relative humidity with temperature, $\Delta RH / \Delta Temp$, was calculated for the different RH sensors. A simple approach was used for this calculation, based on the maximum and minimum RH values computed for each day, as reflected in Equation [1] below. It should be noted that in this equation, temperature refers to the concrete temperature at the same location where RH is being measured. Both the RHC and RHS sensors reported RH and temperature.

$$\Delta RH / \Delta Temp_{\text{day}j} = (RH_{\text{max,day}j} - RH_{\text{min,day}j}) / (Temp_{RH_{\text{max,day}j}} - Temp_{RH_{\text{min,day}j}}) \quad [1]$$

where: $RH_{\text{max,day}j}$ is maximum RH during day j,
 $RH_{\text{min,day}j}$ is minimum RH during day j,
 $Temp_{RH_{\text{max,day}j}}$ is temperature when RH reaches its maximum value during day j, and
 $Temp_{RH_{\text{min,day}j}}$ is temperature when RH reaches its minimum value during day j.

This approach results in one value of $\Delta RH / \Delta Temp$ for each day. Ratios determined for days where rainfall took place were discarded since the changes in RH were not only related to temperature changes but to changes in concrete moisture content as well. Ratios were also discarded when the change in RH ($RH_{\text{max,day}j} - RH_{\text{min,day}j}$) was below 2 percent for the portland cement mixes and below 1 percent for the CSA concrete. The reason is that the calculated ratios were not regarded as a reliable estimate of concrete properties when RH daily variation was very small.

The ratios $\Delta RH/\Delta Temp$ calculated for the RHC sensors located at 20 mm (0.8 in.) depth are presented in Figure 3.18. As this figure shows, $\Delta RH/\Delta Temp$ ratios are mainly dependent on the internal relative humidity of the concrete, which is consistent with laboratory results reported in Reference (13). The order of magnitude of the $\Delta RH/\Delta Temp$ ratios, for the portland cement-based mixes, also agrees with the results in Reference (13). Compared to the portland cement-based mixes, the CSA concrete presented less variation of RH versus temperature.



The series of black triangles corresponds to RHC sensor located at 50 mm (2 in.) depth.

Notes:

- $\Delta RH/\Delta Temp$ were determined for Section M (P2+SRA) for a short period of time only. The reason is the RHC sensor either did not work properly or reported 100 percent RH most of the time.
- The series of black triangles in the CSA plot corresponds to the RHC sensor located at 50 mm (2 in.) depth. For all the other mixes, the RHC sensor at 50 mm (2 in.) depth reported 100 percent RH (or close) at all times, so the ratios $\Delta RH/\Delta Temp$ could not be determined.

Figure 3.18: RH dependence on temperature, based on RHC sensors at 20 mm (0.8 in.) depth.

The RHC sensors resulted in much larger $\Delta RH/\Delta Temp$ ratios than the RHS sensors. Ratios up to 0.5 percent/ $^{\circ}C$ (0.25 percent/ $^{\circ}F$) were measured with RHC sensors, while RHS sensors resulted in values approximately half of those. This means that RH measured with the Campbell Scientific CS215-L sensors showed greater sensitivity versus temperature than RH measured with the laboratory-mounted RHS sensors. This can be seen when comparing the diurnal variations of RH in Figure 3.11 (RHC) versus Figure 3.12 (RHS).

Since both types of sensors use the SHT75 unit, the differences might be related to the encapsulation and/or to the manipulation of that unit in the laboratory when producing the RHS sensors. In this case, the encapsulation is believed to be the reason behind the differences. More specifically, the size of the encapsulation is believed to have caused the differences between $\Delta RH/\Delta Temp$ ratios measured with RHC and RHS sensors. Encapsulation of both sensors can be seen in Figure 2.11. The CS215-L capsule (the white cup in Figure 2.11) lets much less air surround the SHT75 unit than the RHS capsule. The larger encapsulation of the RHS sensors might have served as a reservoir for water vapor, which would have lessened the RH changes in the concrete air pores. As already noted, with a constant amount of water vapor in the air, RH changes with temperature in the direction opposite that of the RH in portland cement concrete air pores. For reference, an increase of $1^{\circ}C$ ($1.8^{\circ}F$), from 25 to $26^{\circ}C$ (77 to $79^{\circ}F$), would result in a decrease of RH from 95 percent to 89 percent if the water vapor in the air was constant. For this reason, water vapor would migrate from concrete to the capsule when the temperature increases and in the opposite direction when the temperature decreases. Consequently, the size of the encapsulation will have an effect if temperature changes more rapidly than water vapor redistribution takes place.

RH was also measured with RHS sensors in three trial slabs that were built as part of this research project prior to the construction of the BCOA tests sections. The concrete used for building the trial slabs was very similar to the P2 concrete used for building the test sections. In the trial slabs, the SHT75 sensors were encapsulated in a 1/2 inch (12.5 mm) internal diameter PVC pipe, which encloses much more air than the plastic tube used for the instrumentation of the BCOA test sections. Probably because of this additional air surrounding the SHT75 sensor, the RH decreased as the temperature increased, which is the opposite of the tendency reflected in Figure 3.18. This result supports the hypothesis that the RHC sensors' smaller encapsulation—compared to that of the RHS sensors—is why RHC sensors yielded larger $\Delta RH/\Delta Temp$ ratios than the RHS sensors. In line with this hypothesis, the $\Delta RH/\Delta Temp$ ratios determined with RHC sensors were considered to be preferable to the smaller ratios determined with RHS sensors.

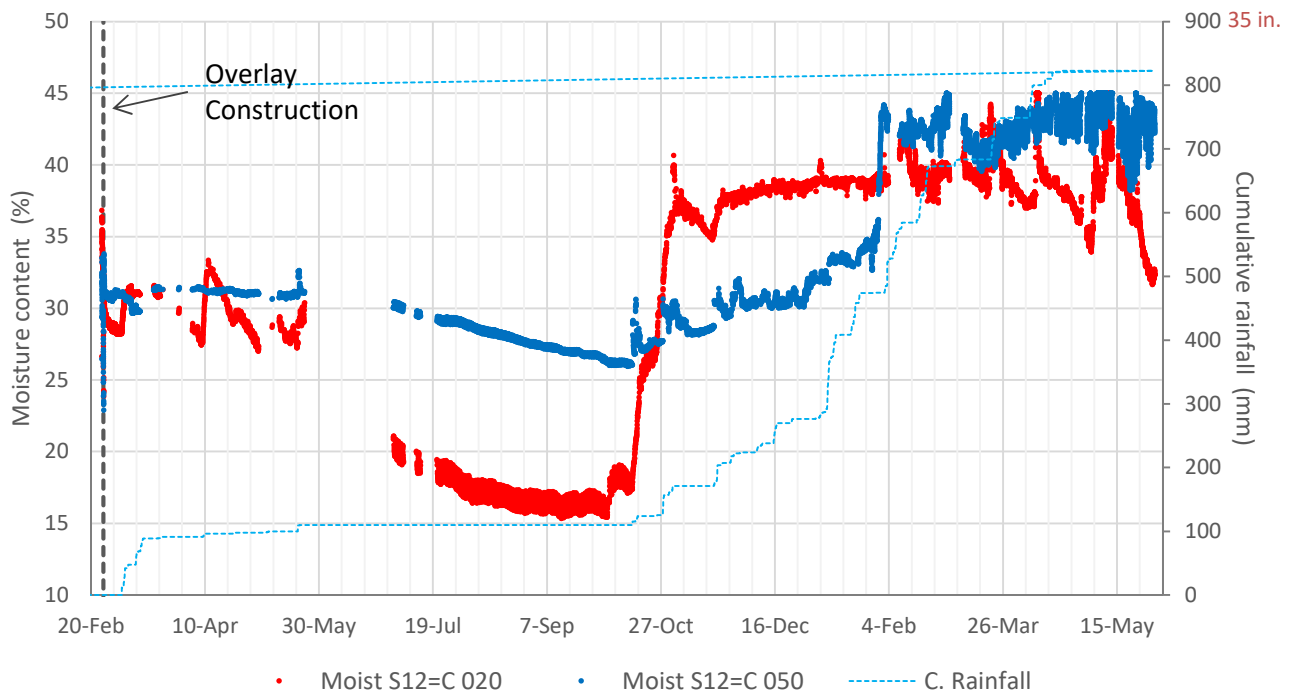
It unclear why negative $\Delta RH/\Delta Temp$ ratios were obtained for the CSA mix at 20 mm (0.8 in.) depth when RH was close to 100 percent (Figure 3.18). Further, it is also unclear why the ratios determined for the sensor located

at 20 mm (0.8 in.) depth in that mix differed from the ratios determined at 50 mm (2.0 in.) depth. The possibility of a measurement error cannot be ignored.

3.3 Data Collected by the Moisture-Content Sensors

3.3.1 Examples of Collected Data

Moisture content (MC) was measured using SMT EMC sensors. Examples of data collected with these sensors are shown in Figure 3.19. These sensors show the drying that takes place during periods with no rainfall and the increased moisture after periods of rainfall. It appears that in both wet and dry periods, the environmental effects on moisture content were not as noticeable as they were on concrete relative humidity. These MC data reflect also diurnal changes related to temperature fluctuations.



Note: The three-digit number at the end of each sensor ID indicates the depth of the sensor in millimeters (mm). The two sensors are located at the center of the Slab 12 (=C).

Figure 3.19: Example of readings from MC sensors (Section N).

3.3.2 Data Analysis

Daily mean values (i.e., the mean of all the readings for a day) were computed for all the sensors in order to conduct a preliminary analysis of the MC data. These data are the basis for the preliminary conclusions presented below.

3.3.3 Preliminary Conclusions

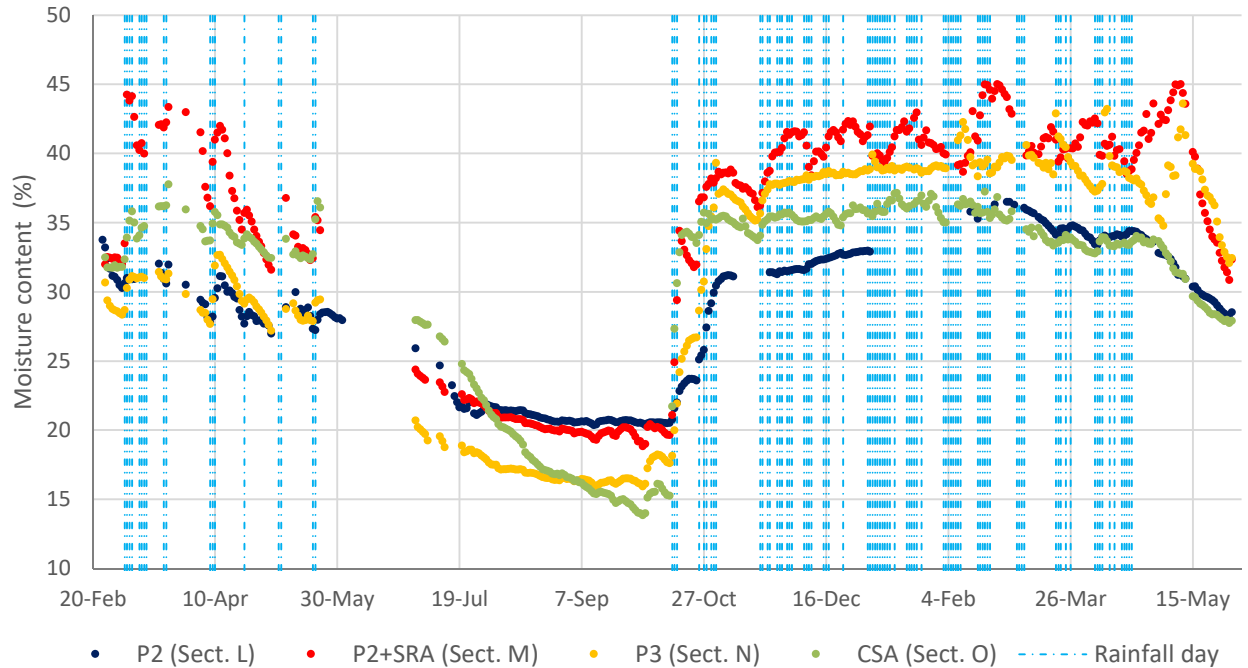
Ranking of Mixes and Curing Procedures Based on the Moisture Content

Figure 3.20 shows the moisture content at 20 mm (0.8 in.) depth for the different mixes and curing procedures. There are some similarities between evolution of MC in this figure and the evolution of RH at the same location, which is shown in Figure 3.13 (RHC) and Figure 3.14 (RHS). In particular, the good performance of the CSA mix during the early months following construction is clear in Figure 3.20. It is also clear the higher rate of drying in this mix, compared to the other mixes, from June to September 2016. Because of this high drying rate, this mix reached the lowest MC values of all the mixes by the end of September 2016.

The plots of the evolution of MC at 20 mm (0.8 in.) depth show that the P3 mix had worse drying performance than the P2 mix. Both of these mixes reached similar MC values for a few months after the overlay construction, but from June to September 2016 the P3 mix experienced more drying than the P2 mix. As a result, the MC values measured in the P3 mix at the end of that latter month were around 5 percent lower than the values measured in the P2 mix at that time. Minimizing drying shrinkage is particularly important in the early stages of hydration when strength is low, although for the rapid strength mixes used in this study the early stages of hydration passed very quickly compared to conventional concrete.

The effect of the SRA treatment was clear during the months following the overlay construction, as Figure 3.20 shows. During this initial period, the MC in Section M where P2 was cured with SRA) was much higher than in Section L where P2 mix was cured with curing compound. Nonetheless, the beneficial effect of the SRA was not clear during the summer months since the MC in both sections reached similar values at that time. However, this outcome does not agree with observations made from the RH data, where the measurements show the effects of the SRA treatment extending through the summer months.

Unfortunately, the MC sensor located at 20 mm depth in Section K (P2-ICC) did not work properly, so it is not possible to rank the P2-ICC in terms of drying susceptibility based on MC sensors.

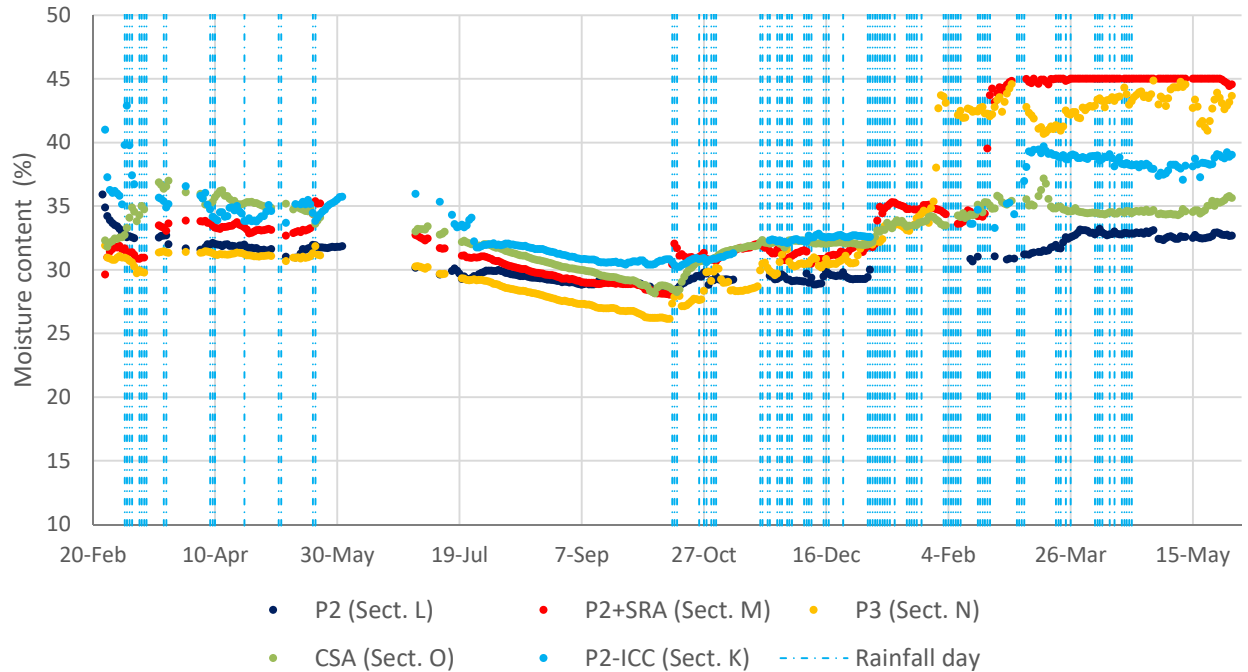


Notes:- Each point on the graph is the average of MC values measured in one day.
 - MC data were unavailable at 20 mm (0.8 in.) depth for P2-ICC mix.

Figure 3.20: Moisture content at 20 mm (0.8 in.) depth.

Concrete Self-Desiccation

As shown in Figure 3.16, the RHC sensors located at 50 mm (2.0 in.) depth in the mixes with portland cement did not show any evidence of drying following overlay construction even though drying was expected, at least in the P2 and P3 mixes, due to the internal desiccation caused by the low water/cement ratio of these mixes. The RHC sensors at 50 mm (2.0 in.) depth showed no drying during the summer months either, reporting values of 100 percent RH (or close to it) at all times. However, the MC values measured at the same location clearly indicate drying during the summer months (Figure 3.21). This result again raises questions about the RHC sensors’ ability to capture relatively low levels of drying (that is, RH values close to 100 percent).



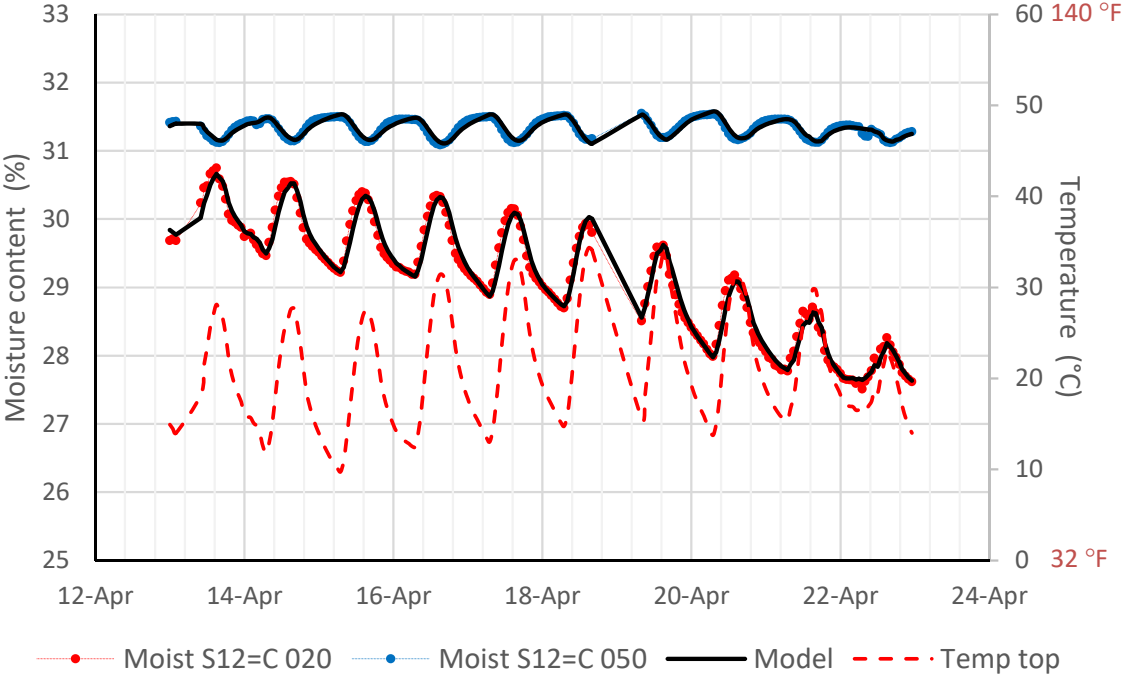
Note: Each point in the graph is the average of MC values measured in one day.
Figure 3.21: Moisture content at 50 mm (2.0 in.) depth.

Diurnal Variations of Moisture Content

The response of the moisture-content sensors at 20 and 50 mm (0.8 and 2.0 in.) depth show diurnal variations that are related to temperature changes. The temperature dependence of the MC sensors’ response can be seen in the examples shown in Figure 3.22. This dependence was also verified by the RH sensors located at 20 mm (0.8 in.) depth: RH and temperature changed in the same direction (RH increased when temperature increased). This was also the most common pattern observed for the moisture-content sensors located at 20 mm (0.8 in.) depth, although there were some exceptions. It should be noted that, overall, MC at 20 mm (0.8 in.) depth changed with temperature much less than RH did. This can be seen by comparing the MC data plotted in Figure 3.19 against the RHC data shown in Figure 3.11. The opposite occurred at 50 mm (2.0 in.) depth: MC changed versus temperature while RH did not. At 50 mm (2.0 in.) depth, the MC-temperature relationship tended to change in direction opposite that at 20 mm (2.0 in.) depth. This means that, at 50 mm (2.0 in.) depth, MC decreased when temperature increased, as in the example shown in Figure 3.22. This was the general rule although, again, there were a few exceptions.

That MC and RH would change in the same direction as temperature changes might be considered to be obvious in a first approximation, but it is not. Reference (13) shows several mechanisms that result in temperature-related changes in the internal relative humidity of the concrete while the water content (moisture) remains constant.

These mechanisms are related to water surface tension and water redistribution within the concrete. This means that the RH of the concrete would change versus temperature while the concrete moisture content would not. Again, it must be noted that the MC sensors do not measure concrete moisture content, but the moisture content of the wood surrounding the sensors (western hemlock for this particular model of MC sensor). If the relative humidity in the air pores in the concrete increases, even if the concrete moisture content does not change, water can be expected to migrate from the concrete to the sensors' wood. This would explain why both variables, RH and MC, tend to change in the same direction at 20 mm (0.8 in.) depth. In any case, the temperature changes will involve a complex process of water redistribution between the concrete and the wood of the sensor, which will affect the response of the MC sensors.



Note: The model assumes MC has a fixed term (constant within one day) plus a variable term that is a linear function of the temperature: $MC = MC(25^{\circ}C, \text{ day}) + GT \cdot (\text{Temp} - 25^{\circ}C)$. The model's parameters (MC at 25°C, for each day, and the proportionally factor GT), were determined through an error minimization iterative process. A set of parameters was determined for the top MC sensor and a different set for the bottom sensor.

Figure 3.22: Example of diurnal variations of MC (Section L).

Specifically, concrete moisture-content and the RH of the air in concrete pores are strongly related. In fact, concrete moisture-content together with temperature determine the relative humidity in the concrete air pores in the following way:

1. The free water content of the concrete (that is, concrete moisture) determines how much of the concrete pores' volume is occupied by water (the greater the amount of moisture, the greater the total volume of the pores filled with water) and, consequently, the volume of the remaining fully saturated pores (assuming the larger pores empty first) and the radius of the pores that are partly full;
2. The radius of the pores partly filled with water, combined with temperature, determines the amount of pore water suction; and
3. That pore water suction—again, combined with temperature—determines the concrete air pore RH.

3.4 Data Collected by the Vibrating Wire Strain Gages

3.4.1 Examples of Collected Data

Figure 3.23 shows examples of data collected with the vibrating wire strain gages (VWSGs). In particular, the data correspond to the two strain gages located close to an interior corner of Slab 13 in Section N (the sensor-naming convention is included in the Appendix). The two strain gages were placed in the longitudinal direction, one at the top of the concrete slab, 20 mm (0.8 in.) below the surface, and the other at the bottom of the concrete slab, 95 mm (3.7 in.) below the surface, i.e., 20 mm (0.8 in.) above the slab bottom (overlays of all ENV sections are 115 mm [4.5 in.] thick). A baseline for strain was determined after concrete field setting time (FST), i.e., strain was assumed to be zero at the FST of each ENV section.

The data in Figure 3.23 reflect moisture-related shrinkage (both drying and autogenous) and thermal deformations of the concrete. The drying shrinkage is evident as the strains measured with the top strain gage are much higher (in absolute value) than the strains measured with the bottom strain gage.

As noted in Section 2.2, eight unrestrained shrinkage beams were fabricated using the same mixes and curing procedures used in the BCOA sections (Figure 2.12). Figure 3.24 shows examples of the data collected with the VWSGs in these beams.

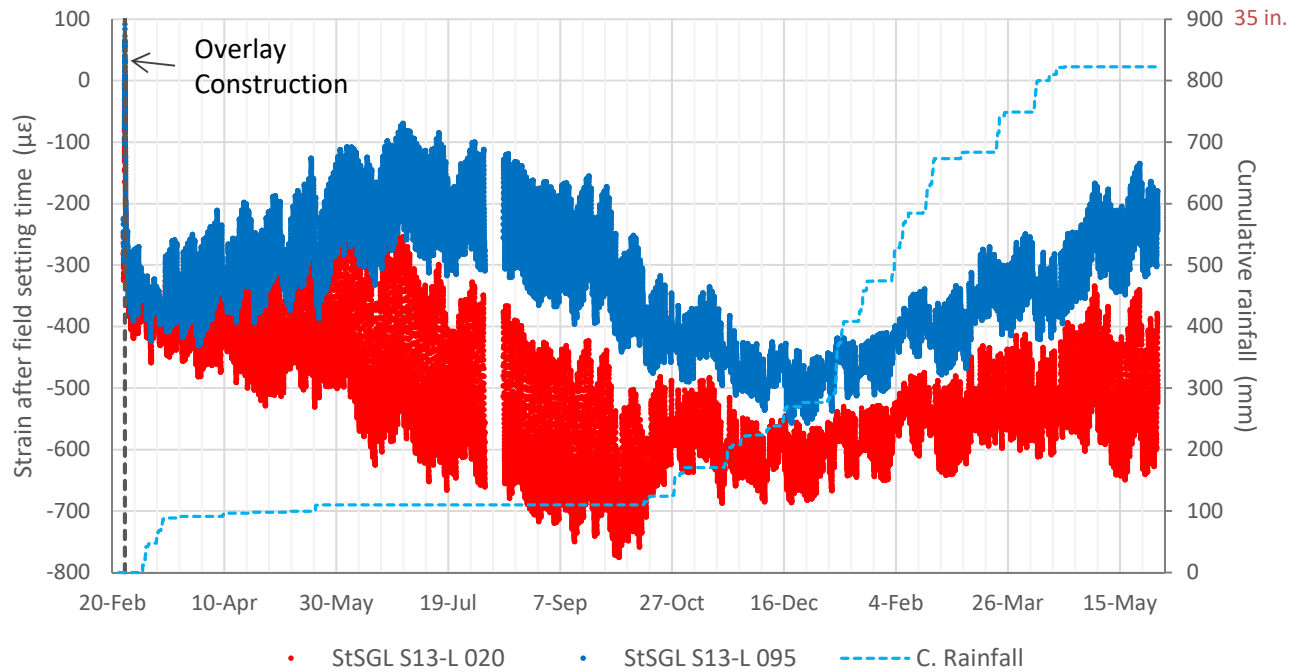


Figure 3.23: Example of readings from VWSG sensors (Section N).

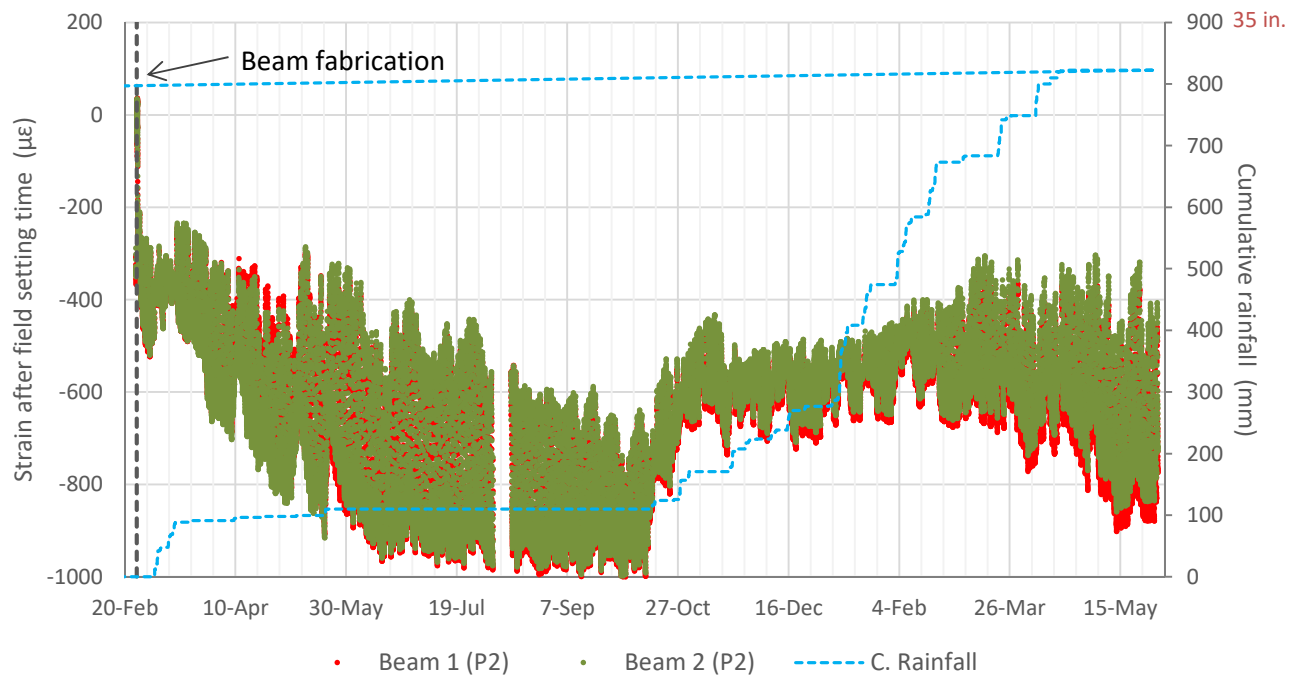


Figure 3.24: Example of readings from VWSG sensors (unrestrained shrinkage beams).

3.4.2 Data Analysis

The strain data collected by the VWSG sensors in the BCOA sections were analyzed by considering the mean and the differential strains, ϵ_{MEAN} and ϵ_{DIFF} , calculated for the pair of gages at each location as shown in Figure 3.25 and Figure 3.26. ϵ_{MEAN} quantifies slab expansion-contraction, while ϵ_{DIFF} quantifies slab bending. The field setting time was used as a reference for determining strain, which means that ϵ_{MEAN} and ϵ_{DIFF} are zero at that time. It is assumed that both ϵ_{MEAN} and ϵ_{DIFF} have two components, one related to temperature changes and one related to moisture-related shrinkage. The same assumption applies to the strain measured with VWSGs in the unrestrained shrinkage beams (ϵ). The approach used for determining the field setting time and the models used for fitting the strain in the unrestrained shrinkage beams (ϵ) and in the BCOA sections (ϵ_{MEAN} and ϵ_{DIFF}) are described below.

The mean strain ϵ_{MEAN} is important because mean contraction causes tensile stresses due to friction with the base. The differential strain ϵ_{DIFF} is important because it causes bending stresses resulting in tensile stresses at the top of the slab if the top contracts more than the bottom and at the bottom of the slab if the bottom contracts more than the top.

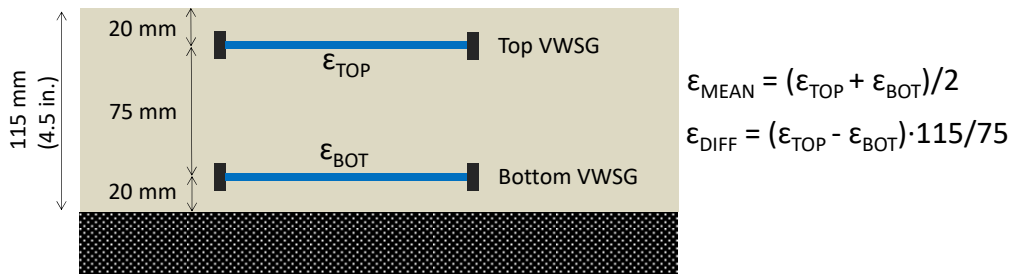
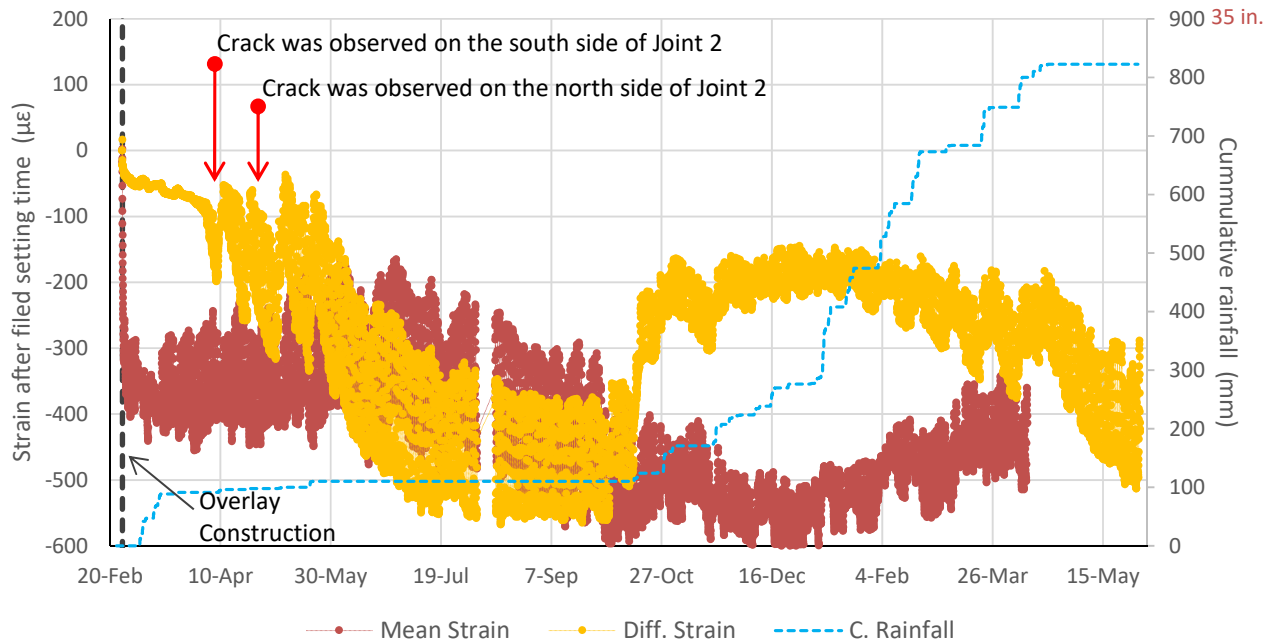


Figure 3.25: Strain composition for analysis of VWSG data.

Determination of Concrete Field Setting Time

Field setting time (FST) is defined here as the time at which the concrete is first able to develop stress when it is subjected to imposed deformations in the field. This time is of critical importance for mechanical analysis because any deformation imposed after that time can produce stress and, consequently, can produce damage to the material. This also means that the strain history up to this time can be ignored as far as stress and damage are concerned.



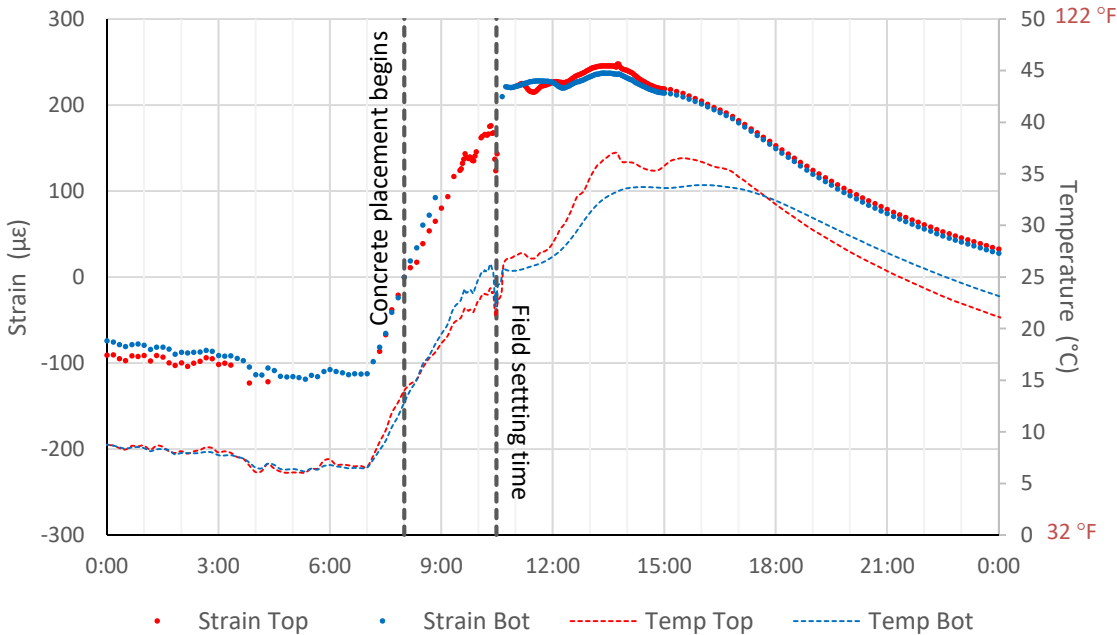
Note: Data in this figure come from two VWSGs located close to Joint 2 in Section N. For this joint, a crack propagating through the overlay thickness (joint deployment) was observed on April 5, on the south side, and on April 26, on the north side. As this figure shows, joint deployment resulted in the onset of differential strain.

Figure 3.26: Example of mean and differential strain calculated from VWSG sensors (Section N, Slab 13-L, Figure 3.23 data).

The field setting time delimits two states in the concrete: fresh and hardened. In practice, the delimitation between these two states is not a single point but a time interval. Nonetheless, defining a single time as a reference to determine strain is very convenient, and it is considered to be accurate enough for the analysis presented in this report. Except for the CSA mix, the field setting time of the different mixes was determined on the basis of the strains and temperatures measured by the VWSG sensors (determination of field setting time for the CSA mix is discussed at the end of this section). The procedure is illustrated below, by analyzing the strains measured with a pair of strain gages in Section J.

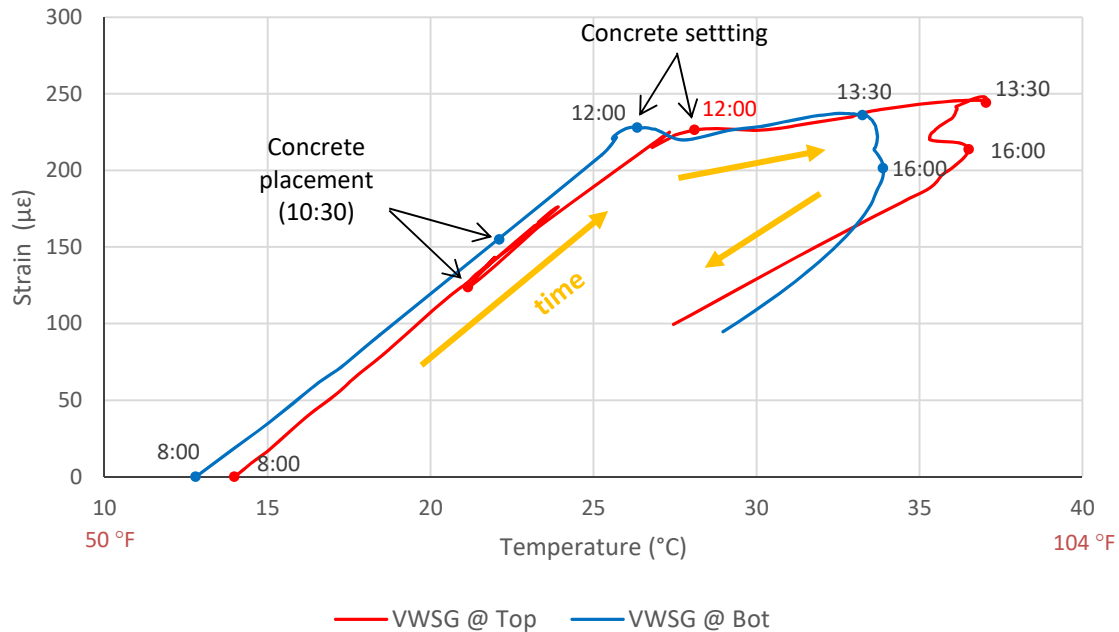
Figure 3.27 shows strain measured with the top and bottom strain gages located at the interior corner of Section J on the day that concrete overlay was placed on this section (February 25, 2016). The strain and temperature followed the same pattern before concrete placement, i.e., there was a linear relationship between strain and temperature, as can be seen in Figure 3.28. This is because the strain measured by the gages was actually the thermal deformation of the gages. The gages were supported by fiberglass chairs before overlay construction, and they were free to expand and contract due to temperature changes. In Figure 3.27 and Figure 3.28 an arbitrary time (8:00 a.m.) was selected to calculate strain. Overlay placement took place between 10:30 a.m. and 10:40 a.m. For approximately one and a half hours after concrete was placed, temperature and strain continued to increase

while maintaining the same relative proportion (that is, increase in strain versus increase in temperature), and continued the same straight-line relationship of strain versus temperature that existed before the concrete was placed (Figure 3.28). This is compatible with the concrete being still fluid, so the strain gages were free to expand due to the increasing temperature. Nonetheless, temperature versus strain started to follow a different evolution pattern after approximately 12:00 p.m. After this time, the strain measured by top and bottom strain gages was relatively stable while the temperature was increasing, as seen in Figure 3.27 and Figure 3.28. This means the gages were not free to expand, which indicates the concrete was restricting their movements. This is considered an indication that the concrete was able to develop stress and, consequently, this time was selected as the field setting time of that particular pair of strain gages. A unique *field setting time* was defined for each ENV section based on the field setting times of all the gages in the section. As was expected, the differences between gages within the same section were minimal.



Note: An arbitrary time, 8:00 a.m., was selected for calculation of strain in this figure.

Figure 3.27: Example of early strain development (Section J, Slab 12-L).



Note: An arbitrary time, 8:00 a.m., was selected for calculation of strain in this figure.
Figure 3.28: Example of determination of concrete field setting time (Section J, Slab 12-L).

As noted, both VWSG sensors (top and bottom) in Figure 3.28 show little expansion after the setting time, even though the temperature was still increasing. This can be seen in Figure 3.28, as the strain-versus-temperature plots lie close to a horizontal line between approximately 12:00 p.m. and 1:30 p.m. The temperature becomes stable after this initial period, while the strain continues decreasing. This is reflected in the strain-versus-temperature plots lying close to a vertical line between approximately 1:30 p.m. and 4:00 p.m. The same pattern was observed in all portland cement-based mixes, and it was not observed in the CSA concrete. These results indicate that another phenomenon exists—for the portland cement-based mixes—that results in shrinkage of the concrete. This phenomenon is likely to be autogenous shrinkage. Autogenous shrinkage is the result of the internal desiccation of the concrete as a consequence of cement hydration water demand and the net volume reduction resulting from the cement hydration reaction. The fact that this early-age shrinkage was not observed for the CSA mix is an indication that it is caused by autogenous shrinkage. As explained earlier, CSA cement is known to result in low moisture-related shrinkage (4), while the low water-cement ratio of all the portland cement-based mixes used for the BCOA construction is known to result in autogenous shrinkage (10).

The initial and final setting times of the different mixes, determined according to ASTM C403, were supplied by the mixes' producers. These values were compared to the field setting times determined for the portland cement-based mixes on the basis of VWSG sensor data, as shown in Figure 3.29. Overall, good agreement exists between lab and field results. In all cases, the field setting times fell between the initial lab setting time, which corresponds

to 3.5 MPa (500 psi) penetration resistance, and the final lab setting time, which corresponds to 27.6 MPa (4,000 psi) penetration resistance. The field setting time of portland cement-based mixes was metered starting when the accelerator was dosed to the ready-mix truck.

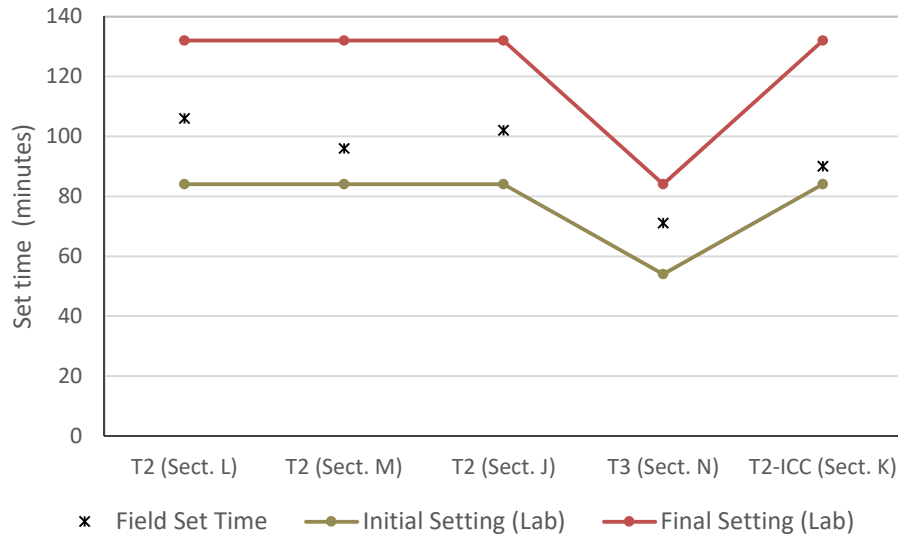


Figure 3.29: Correlation between lab and field setting times for the portland cement mixes.

The field setting time of the CSA mix was determined by using the average of the initial and final setting times determined in the laboratory according to ASTM C403, as supplied by CTS Cement. The initial setting time of this mix was between 20 and 25 minutes, and final setting occurred around 5 minutes later. The field setting time, used as a reference for strain calculation, was set to 25 minutes.

Uniaxial Strain Model for the Unrestrained Shrinkage Beams

A uniaxial strain model was used to analyze the strain collected with the VWSGs inside the unrestrained shrinkage beams (USB). The model is shown in Equation [2] and described below.

$$\epsilon_{USB} = \epsilon_{Sh} + \epsilon_{Ther1} = \epsilon_{Sh,T0} + \epsilon_{Sh,T-T0} + \epsilon_{Ther1} \quad [2]$$

- where:
- ϵ_{USB} is strain measured with the VWSG ($\epsilon_{USB}=0$ at FST);
 - ϵ_{Sh} is the moisture-related shrinkage;
 - $\epsilon_{Sh,T0}$ is the moisture-related shrinkage at the temperature T_0 ;
 - $\epsilon_{Sh,T-T0}$ reflects temperature dependence of ϵ_{Sh} : $\epsilon_{Sh,T-T0} = \epsilon_{Sh} - \epsilon_{Sh,T0}$ and it is assumed $\Delta\epsilon_{Sh,T-T0} = \gamma(t) \cdot \Delta T$;
 - ϵ_{Ther1} is $CTE_{SAT} \cdot (T-T_0)$, where CTE_{SAT} is the coefficient of thermal expansion determined in the laboratory under saturated conditions (AASHTO T 336-15);
 - t is time;
 - T is beam temperature; and
 - T_0 is beam temperature when concrete sets (FST)

The model assumes that the strain has two components, one related to the temperature changes (changes versus T_0 , the temperature when concrete sets) and another related to the moisture. The moisture-related strain (shrinkage) is divided into two components as well: ϵ_{Sh,T_0} and $\epsilon_{Sh,T-T_0}$. The former is the moisture-related shrinkage for the constant temperature T_0 . The latter is the thermal component of the moisture-related shrinkage. This component is assumed to be linearly related to the temperature, with the proportionality factor changing with time. After these assumptions, the model can be formulated incrementally, as indicated in Equation [3].

$$\begin{aligned}\Delta\epsilon_{USB} &= \Delta\epsilon_{Sh,T_0} + \gamma(t) \cdot \Delta T + CTE_{SAT} \cdot \Delta T = \\ &= \Delta\epsilon_{Sh,T_0} + [\gamma(t) + CTE_{SAT}] \cdot \Delta T = \\ &= \Delta\epsilon_{Sh,T_0} + CTE(t) \cdot \Delta T\end{aligned}\quad [3]$$

where: $CTE(t)$ is time-dependent concrete CTE.

The rest of the terms in this equation are defined in Equation [2] above.

It should be noted that Equation [3] assumes that the changes in strain recorded with VWSGs have two components. The first component is exclusively moisture-related (for constant temperature) and the second component is directly related to temperature changes. The second component takes into account concrete conditions through the CTE variable. Concrete CTE is expected to change versus time because of the changing moisture conditions. It has been known for a long time that moisture conditions significantly impact the CTE of concrete (14).

Two more assumptions were made, as Figure 3.30 shows:

- 1) ϵ_{Sh,T_0} changes linearly within a day.
- 2) The CTE is constant within a day.

The model's parameters (two parameters, $\epsilon_{Sh,T_0 i}$ and CTE_i , per day) were determined through an iterative process of error minimization, where the goal was fitting the strain recorded with the VWSGs. The mean square error (MSE) of the model (pooled MSE of all beams) was $7.2 \mu\epsilon$. An example of this fitting is shown in Figure 3.31.

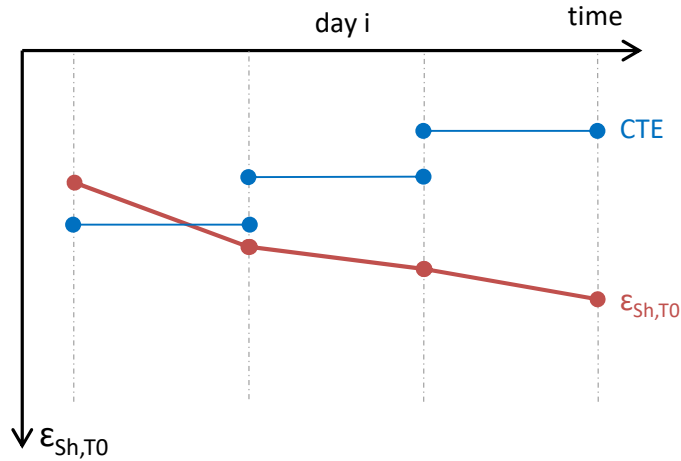
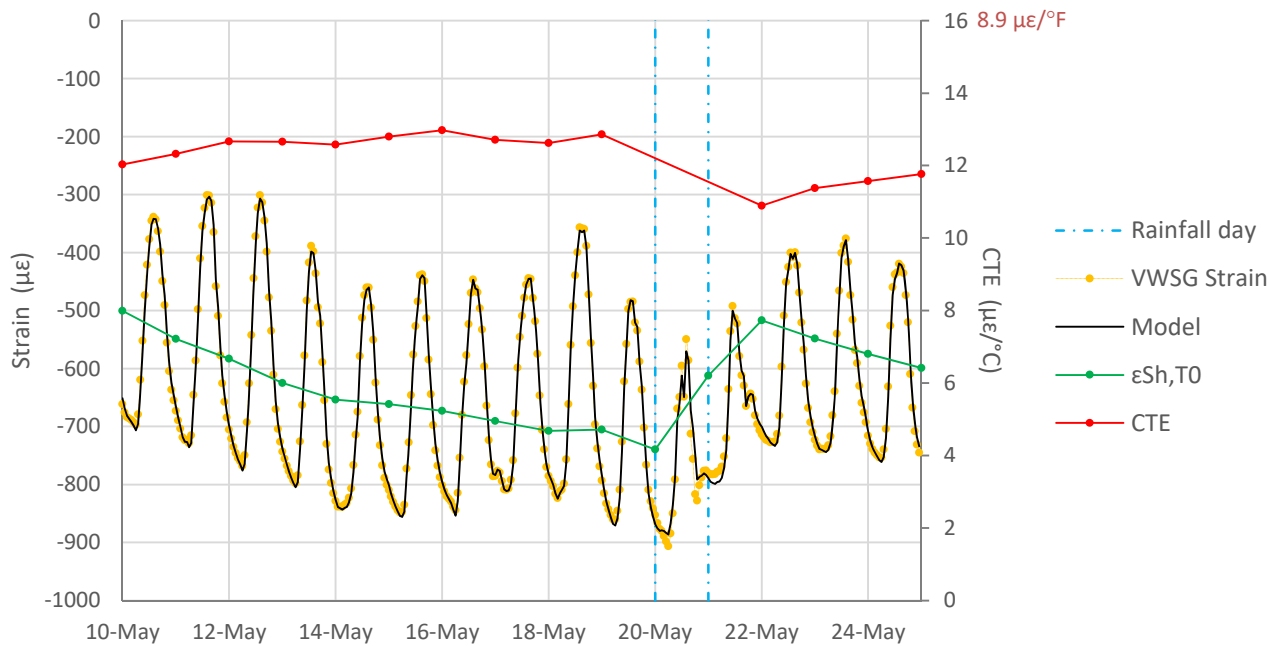


Figure 3.30: The evolution of moisture-related shrinkage and CTE in the USB strain model.



Note: The series “Rainfall day” indicates days where any rainfall took place. The two vertical lines in the figure, one on May 20 and the other on May 21, indicate some rainfall took place on May 20 and May 21, respectively.

Figure 3.31: Example of fitting with the uniaxial strain model (Beam 1, P2 mix).

The model’s assumptions related to the linearity of $\epsilon_{Sh,T0}$ and the constant CTE, both within a day, are not accurate for days with rainfall events. After the rainfall events, a quick recovery of the moisture-related shrinkage was observed for all mixes (1) and, consequently, assuming a linear evolution of $\epsilon_{Sh,T0}$ is not realistic. Further, the CTE of the concrete is expected to change as a consequence of the rapid hydration that the concrete experiences. For

these reasons, two considerations are required for rainfall days: 1) the fitted $\epsilon_{Sh,T0}$ must not be considered a prediction of the actual moisture related shrinkage but a best-fit linear estimation (Figure 3.32), and 2) the CTE values determined for days with rainfall events must not be regarded as estimates of the material's CTE. Consequently, they were discarded from further analysis (note that the CTE series in Figure 3.31 does not have data on May 20 and 21).

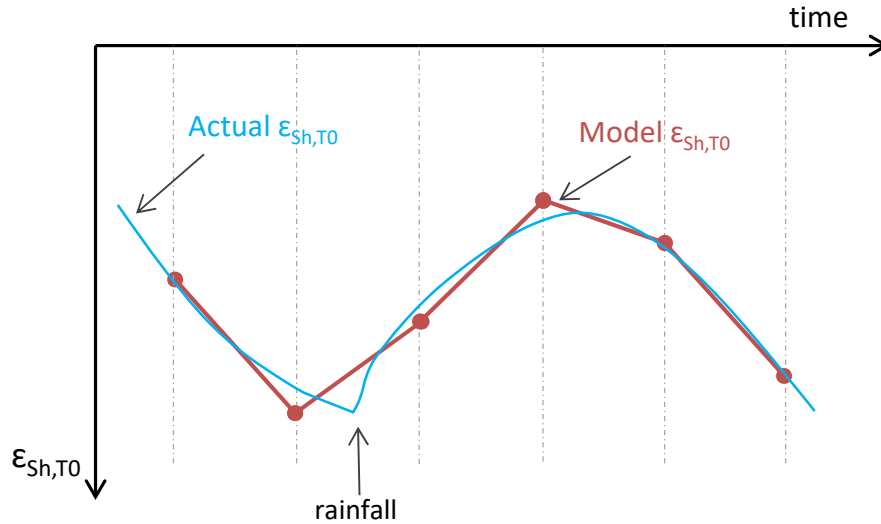


Figure 3.32: Model's limitations during rainfall events.

Strain Model for the BCOA Sections

The strain data collected by VWSGs in the BCOA sections were analyzed by considering the mean and the differential strains, ϵ_{MEAN} and ϵ_{DIFF} , calculated for the pair of gages at each location (Figure 3.25). The models used to analyze each of these two components of the slabs' deformation are shown in Equations [4] and [5], respectively, and described below.

$$\epsilon_{MEAN} = \epsilon_{MEAN,Sh} + \epsilon_{MEAN,Ther1} = \epsilon_{MEAN,Sh,T0} + \epsilon_{MEAN,Sh,T-T0} + \epsilon_{MEAN,Ther1} \quad [4]$$

- where:
- ϵ_{MEAN} is the average strain measured with top and bottom VWSGs ($\epsilon_{MEAN}=0$ at FST);
 - $\epsilon_{MEAN,Sh}$ is the moisture-related shrinkage component of ϵ_{MEAN} ;
 - $\epsilon_{MEAN,Sh,T0}$ is the moisture-related shrinkage component of ϵ_{MEAN} when the temperature profile in the slab is equal to $T0(z)$;
 - $\epsilon_{MEAN,Sh,T-T0}$ reflects temperature dependence of $\epsilon_{MEAN,Sh}$: $\epsilon_{MEAN,Sh,T-T0} = \epsilon_{MEAN,Sh} - \epsilon_{MEAN,Sh,T0}$ and it is assumed $\Delta\epsilon_{MEAN,Sh,T-T0} = \alpha \cdot \gamma(t) \cdot \Delta T_{MEAN}$
 - $\epsilon_{MEAN,Ther1}$ is $\alpha \cdot CTE_{SAT} \cdot (T_{MEAN} - T_{MEAN,0})$, where CTE_{SAT} is the CTE determined in the laboratory under saturated conditions (AASHTO T 336-15);
 - α is a coefficient that accounts for the restriction to slab expansion-contraction due to slab weight and slab interaction with the asphalt base;

t is time;
 $T_0(z)$ is slab temperature profile when the concrete sets (FST), where z is the depth measured from the top surface;
 T_{MEAN} is the mean slab temperature; and
 $T_{MEAN,0}$ is the mean slab temperature when concrete sets (FST)

$$\epsilon_{DIFF} = \epsilon_{DIFF,Sh} + \epsilon_{DIFF,Ther1} = \epsilon_{DIFF,Sh,T_0} + \epsilon_{DIFF,Sh,T-T_0} + \epsilon_{DIFF,Ther1} \quad [5]$$

where: ϵ_{DIFF} differential strain measured with top and bottom VWSGs ($\epsilon_{DIFF}=0$ at FST);
 $\epsilon_{DIFF,Sh}$ is the moisture-related shrinkage component of ϵ_{DIFF} ;
 ϵ_{DIFF,Sh,T_0} is the moisture-related shrinkage component of ϵ_{DIFF} when the temperature profile in the slab is equal to $T_0(z)$;
 $\epsilon_{DIFF,Sh,T-T_0}$ reflects temperature dependence of $\epsilon_{DIFF,Sh}$: $\epsilon_{DIFF,Sh,T-T_0} = \epsilon_{DIFF,Sh} - \epsilon_{DIFF,Sh,T_0}$ and it is assumed $\Delta\epsilon_{DIFF,Sh,T-T_0} = \beta \cdot \varphi(t) \cdot \Delta ELTD$;
 $\epsilon_{DIFF,Ther1}$ is $\beta \cdot CTE_{SAT} \cdot (ELTD - ELTD_0)$, where CTE_{SAT} is the CTE determined in the laboratory under saturated conditions (AASHTO T 336-15);
 β is a coefficient that accounts for the restriction to slab bending due to slab weight, slab interaction with the asphalt base, and transverse joint locking or lack of deployment;
 t is time;
 $T_0(z)$ is slab temperature profile when the concrete sets (FST), where z is depth measured from the top surface;
 $ELTD$ is the equivalent linear temperature difference in the slab (for a given temperature profile, the $ELTD$ is the temperature difference between the top and bottom of the slab for the “equivalent linear temperature profile,” the “equivalent linear temperature profile” is the temperature profile that is linear versus depth and produces the same slab bending produced by the actual vertical temperature profile); and
 $ELTD_0$ is the equivalent linear temperature difference when concrete sets (FST).

The models assume strain has two components, one related to the temperature change (change versus temperature profile in the slab when concrete sets) and one related to the moisture. The moisture-related strain (shrinkage) is divided into two components as well. The first is the moisture-related shrinkage for constant temperature, i.e., if the temperature profile in the slab were to be the same as it was at the FST. The second is the thermal component of the moisture-related shrinkage. This component is assumed to be linearly related to either the mean temperature of the slab (ϵ_{MEAN} model) or the equivalent linear temperature difference (ϵ_{DIFF} model), with the proportionality factors changing with time.

Unlike the model used for the unrestrained shrinkage beams, the models used for ϵ_{MEAN} and ϵ_{DIFF} include α and β coefficients, respectively, that represent the locking or restriction to slab deformation due to slab weight, slab interaction with the asphalt base, and locking or lack of deployment of the transverse joints. If the slab was free to expand and contract without any restriction from the asphalt base α would equal 1. Similarly, β would equal 1 if the transverse joint was fully deployed and the slab was weightless and also free to bend without any restriction from the asphalt base.

Another simplification behind Equation [4] is that changes in the slab's mean temperature produce expansion-contraction of the slab exclusively, i.e., no bending. Similarly, a simplification behind Equation [5] is that changes in the ELTD produce slab bending exclusively, i.e., no expansion-contraction. Both simplifications are realistic, for a homogeneous slab, when the stiffness of the base is much smaller than the stiffness of the concrete overlay, as in BCOA.

After these assumptions are made, ϵ_{MEAN} and ϵ_{DIFF} models can be formulated incrementally, as indicated in Equations [6] and [7] below.

$$\begin{aligned}\Delta\epsilon_{\text{MEAN}} &= \Delta\epsilon_{\text{MEAN,Sh,T0}} + \alpha \cdot \gamma(t) \cdot \Delta T_{\text{MEAN}} + \alpha \cdot \text{CTE}_{\text{SAT}} \cdot \Delta T_{\text{MEAN}} = \\ &= \Delta\epsilon_{\text{MEAN,Sh,T0}} + \alpha \cdot [\gamma(t) + \text{CTE}_{\text{SAT}}] \cdot \Delta T_{\text{MEAN}} = \\ &= \Delta\epsilon_{\text{MEAN,Sh,T0}} + \alpha \cdot \text{CTE1}(t) \cdot \Delta T_{\text{MEAN}}\end{aligned}\quad [6]$$

where: $\text{CTE1}(t)$ is time-dependent equivalent CTE of the concrete slab
 α is a coefficient that reflects the restriction to slab expansion-contraction due to slab weight and slab interaction with the asphalt base

The rest of the terms in this equation are defined in Equation [4] above.

$$\begin{aligned}\Delta\epsilon_{\text{DIFF}} &= \Delta\epsilon_{\text{DIFF,Sh,T0}} + \beta \cdot \varphi(t) \cdot \Delta\text{ELTD} + \beta \cdot \text{CTE}_{\text{SAT}} \cdot \Delta\text{ELTD} = \\ &= \Delta\epsilon_{\text{DIFF,Sh,T0}} + \beta \cdot [\varphi(t) + \text{CTE}_{\text{SAT}}] \cdot \Delta\text{ELTD} = \\ &= \Delta\epsilon_{\text{DIFF,Sh,T0}} + \beta \cdot \text{CTE2}(t) \cdot \Delta\text{ELTD}\end{aligned}\quad [7]$$

where: $\text{CTE2}(t)$ is time-dependent equivalent CTE of the concrete slab, and
 β is a coefficient that reflects the restriction to slab bending due to slab weight, slab interaction with the asphalt base, and transverse joint locking or lack of deployment.

The rest of the terms in this equation are defined in Equation [5] above.

Note that CTE_1 and CTE_2 in Equations [6] and [7], respectively, do not have to be equal. In fact, typically they will be different from each other since a specific CTE profile will impact thermal expansion-contraction and thermal bending in a different way.

Two more assumptions are made, as Figure 3.33 shows:

- 1) $\epsilon_{\text{MEAN,Sh,T0}}$ and $\epsilon_{\text{DIFF,Sh,T0}}$ change linearly within a day.
- 2) $\alpha \cdot \text{CTE}_1$ and $\beta \cdot \text{CTE}_2$ are constant within a day.

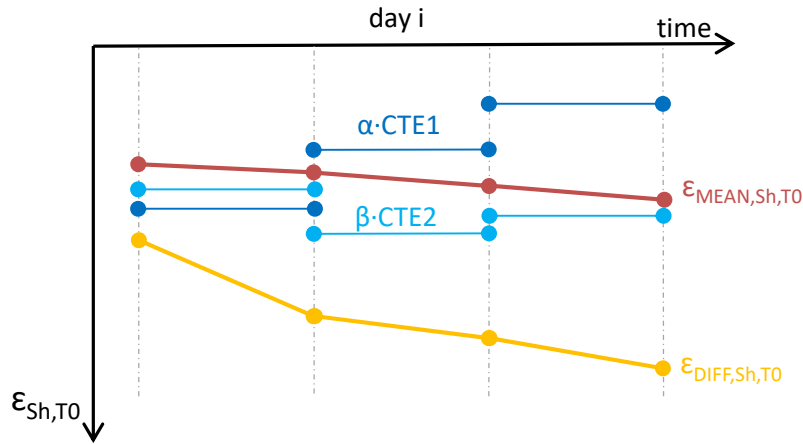


Figure 3.33: Evolution of the moisture-related shrinkage and CTE in the BCOA strains models.

The parameters of each ϵ_{MEAN} and ϵ_{DIFF} model were determined through an iterative process of error minimization, where the goal was fitting the strain calculated for each pair of VWSGs. Each of the models has two parameters per day: $\epsilon_{\text{MEAN,Sh,T0}i}$ and $\alpha\text{-CTE}1_i$ are parameters of ϵ_{MEAN} model, while $\epsilon_{\text{DIFF,Sh,T0}i}$ and $\beta\text{-CTE}2_i$ are parameters of ϵ_{DIFF} model. The mean square errors of the ϵ_{MEAN} and ϵ_{DIFF} models (pooled MSE of all locations of all sections) were 2.8 and 7.0 $\mu\epsilon$, respectively. Examples of this fitting are shown in Figure 3.34 and Figure 3.35.

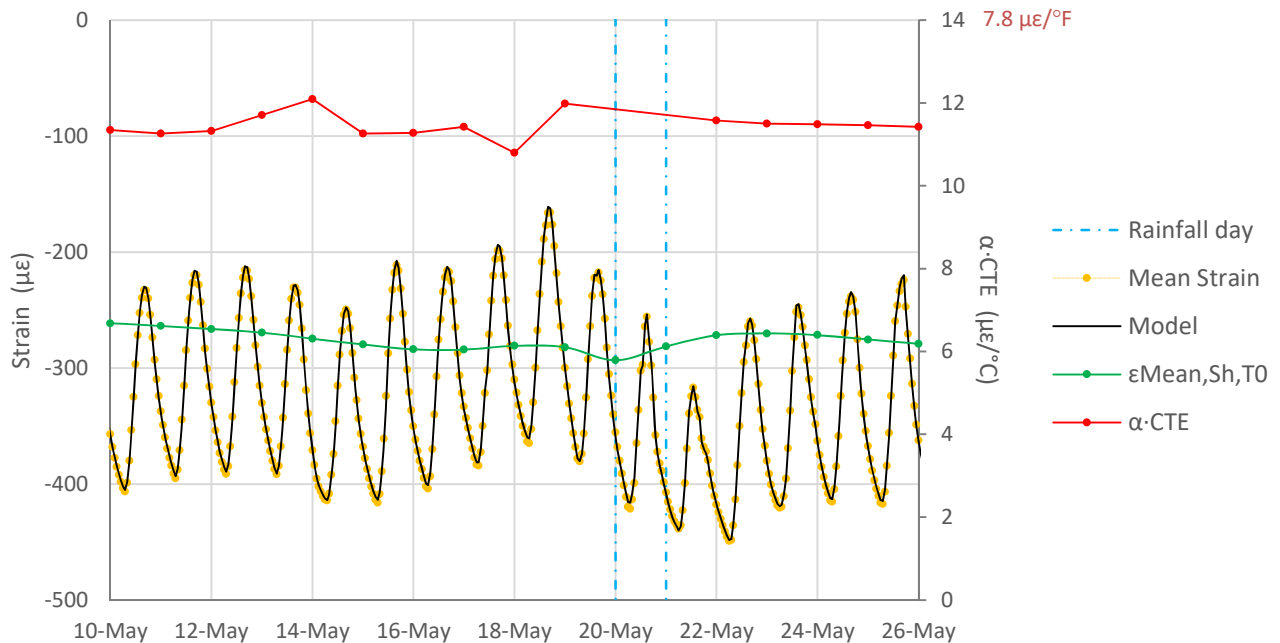


Figure 3.34: Example of fitting with the BCOA strain model (ϵ_{MEAN} , Section N, Slab 13-L).

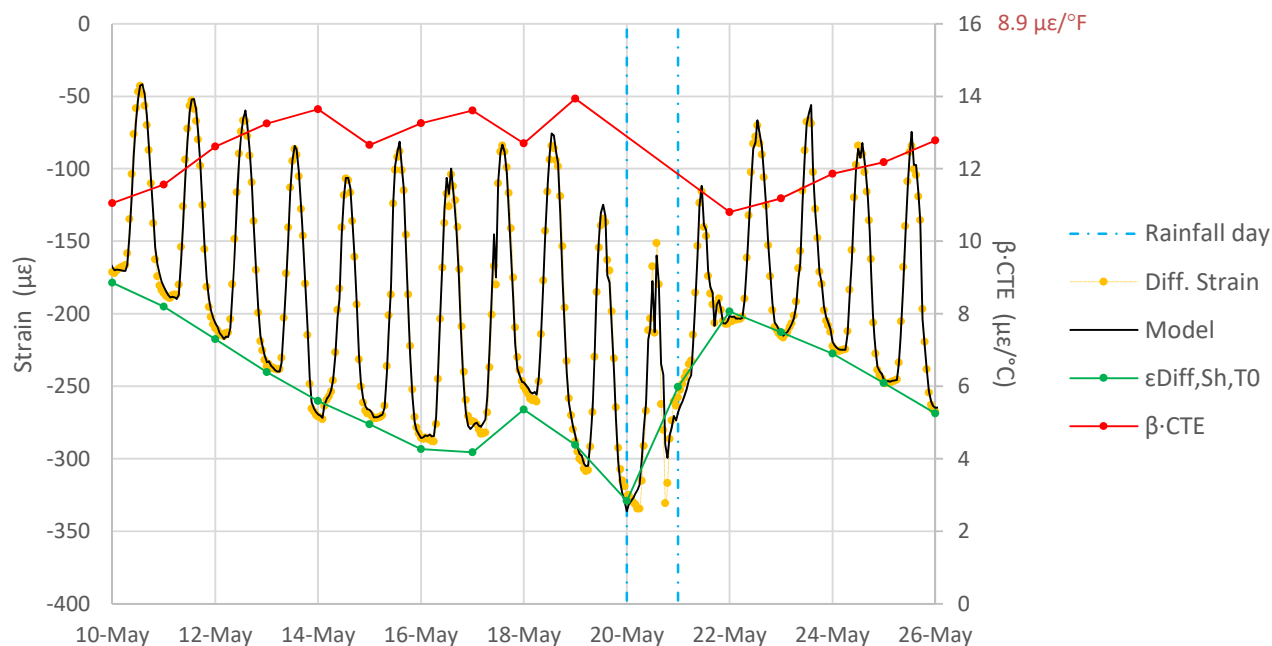


Figure 3.35: Example of fitting with the BCOA strain model (ϵ_{DIFF} , Section N, Slab 13-L).

It should be noted that the α and β parameters are not determined independently from CTE1 and CTE2, respectively. On the contrary, the products $\alpha \cdot CTE1$ are $\beta \cdot CTE2$ are actually the values backcalculated through the iterative process of error minimization. Both $\alpha \cdot CTE1$ are $\beta \cdot CTE2$ have a clear mechanical meaning. $\alpha \cdot CTE1$ is the ratio between slab expansion-contraction (quantified as the average of the strains at the top and bottom of the slab) and the changes in slab mean temperature. $\beta \cdot CTE2$ is the ratio between slab bending (quantified as the difference between the strains at the top and bottom of the slab) and the changes in the equivalent linear temperature difference. For these reasons, the terms “thermal expansion-contraction compliance” and “thermal bending compliance” are also used in this report to refer to $\alpha \cdot CTE1$ are $\beta \cdot CTE2$, respectively. For the unrestrained shrinkage beams, the backcalculated-calculated CTE is actually an estimation of the CTE of the concrete since the beams are free to expand and contract ($\alpha=1$).

Two assumptions were made above: the first is that $\epsilon_{MEAN,Sh,T0}$ and $\epsilon_{DIFF,Sh,T0}$ change linearly within a day; the second is that $\alpha \cdot CTE1$ and $\beta \cdot CTE2$ are constant within a day. These two assumptions are not accurate for days with rainfall events for the same reasons that were argued for the unrestrained shrinkage beams. During rainfall days, the fitted $\epsilon_{MEAN,Sh,T0}$ and $\epsilon_{DIFF,Sh,T0}$ must not be considered as predictions of the actual moisture-related shrinkage but as best-fit linear estimations. For the same reason, the $\alpha \cdot CTE1$ and $\beta \cdot CTE2$ determined for days with rainfall events are not regarded as estimations of the thermal compliance of the slabs, and they were discarded

for further analysis (note that the α -CTE and β -CTE series in Figure 3.34 and Figure 3.35, respectively, do not include data on May 20 and 21).

It should be mentioned that the underlying goal of these models is to remove the thermal component of the strain measured with the VWSG sensors. It is assumed the strain remaining after removal of the thermal strains is the moisture-related shrinkage. This assumption overlooks concrete time-dependent mechanical behavior (creep/relaxation). In practice, the strain that remains after the removal of thermal deformations is an estimation of the effects of moisture-related shrinkage and concrete creep/relaxation. Similarly, the parameters α -CTE1 and β -CTE2 would capture any concrete creep/relaxation deformations that may take place as a consequence of the daily changes in the slab temperature.

A final observation is made in relation to the models presented in this section of the report. The goal of the models is not actually to formulate predictions. Rather, the goal is to determine the parameters of the models. These parameters are the basis for the preliminary conclusions presented below.

3.4.3 Preliminary Conclusions

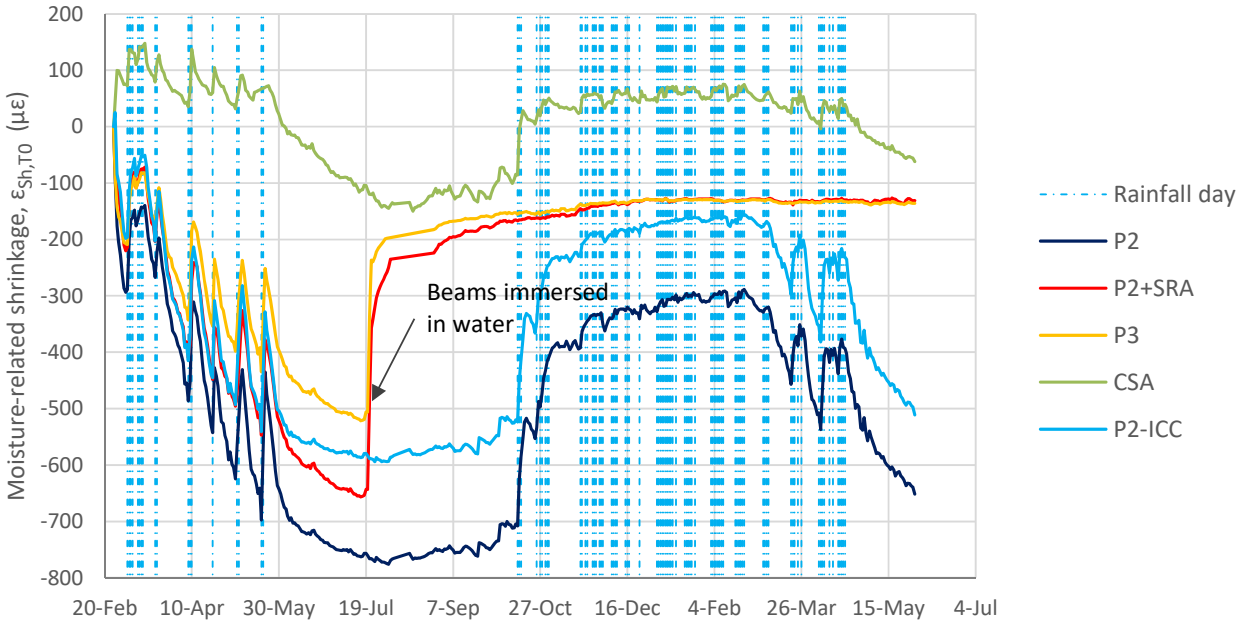
Ranking of Mixes and Curing Procedures Based on Unrestrained Shrinkage Beams

Eight beams were instrumented with VWSG sensors in order to measure the unrestrained expansion-contraction of the concrete (Figure 2.12). The moisture-related shrinkage at constant temperature of these beams ($\epsilon_{Sh,T0}$) was determined according to the procedure outlined in Section 3.4.2. The results for the different mixes and curing procedures are presented in Figure 3.36.

The first observation that can be made from Figure 3.36 is that high levels of moisture-related shrinkage occurred in all the materials other than the CSA concrete. When partially restricted, that shrinkage will potentially result in very high tensile stresses, especially considering the high stiffness of the mixes (1).

Moisture-related shrinkage was also measured on specimens prepared in the laboratory. These specimens were conditioned and tested according to the procedures in ASTM C157-08—except for how long the specimens were immersed in water before being exposed to dry air. Instead of the ASTM's specified standard of 28 days of immersion, for this laboratory characterization the beams were immersed for 3 days. Results of the laboratory characterization are presented in Figure 3.37. Results from both the lab and the field beams yielded a similar ranking of the mixes in terms of drying susceptibility, from best to worst: CSA / P3 / P2-ICC / P2. Further, the ultimate values of the moisture-related shrinkage measured on the field beams were very similar to those measured

in the laboratory (Figure 3.36 versus Figure 3.37). It should be noted that the field unrestrained shrinkage beams were subjected to outdoor environmental conditions while the laboratory beams dried under constant temperature of 23°C (73°F) and 50 percent relative humidity.



Note: P2+SRA and P3 beams were immersed in water on July 20, 2016.

Figure 3.36: Moisture-related shrinkage determined for the unrestrained shrinkage beams ($\epsilon_{sh,t0}$).

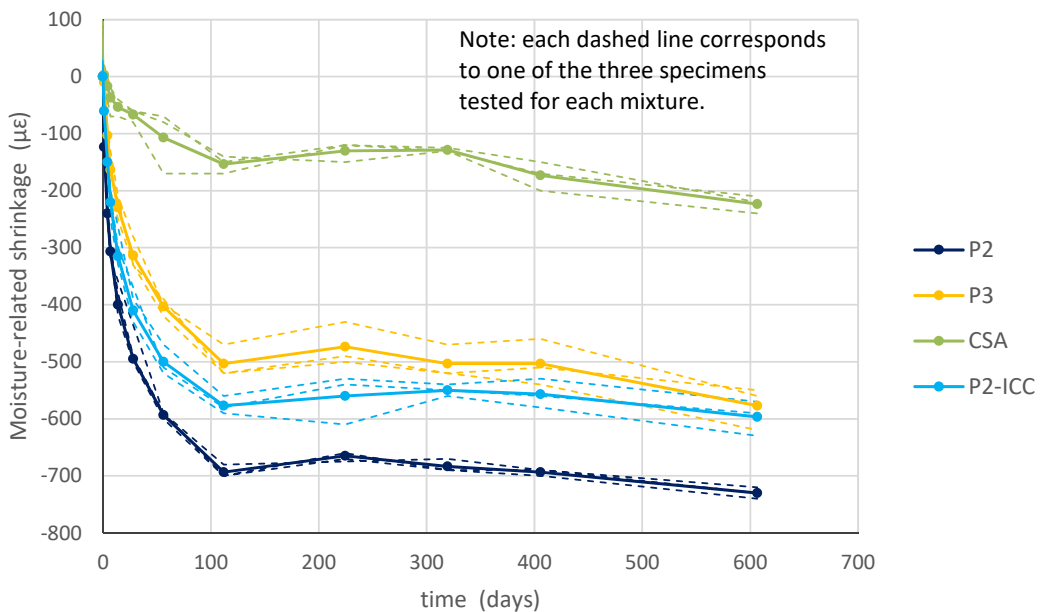
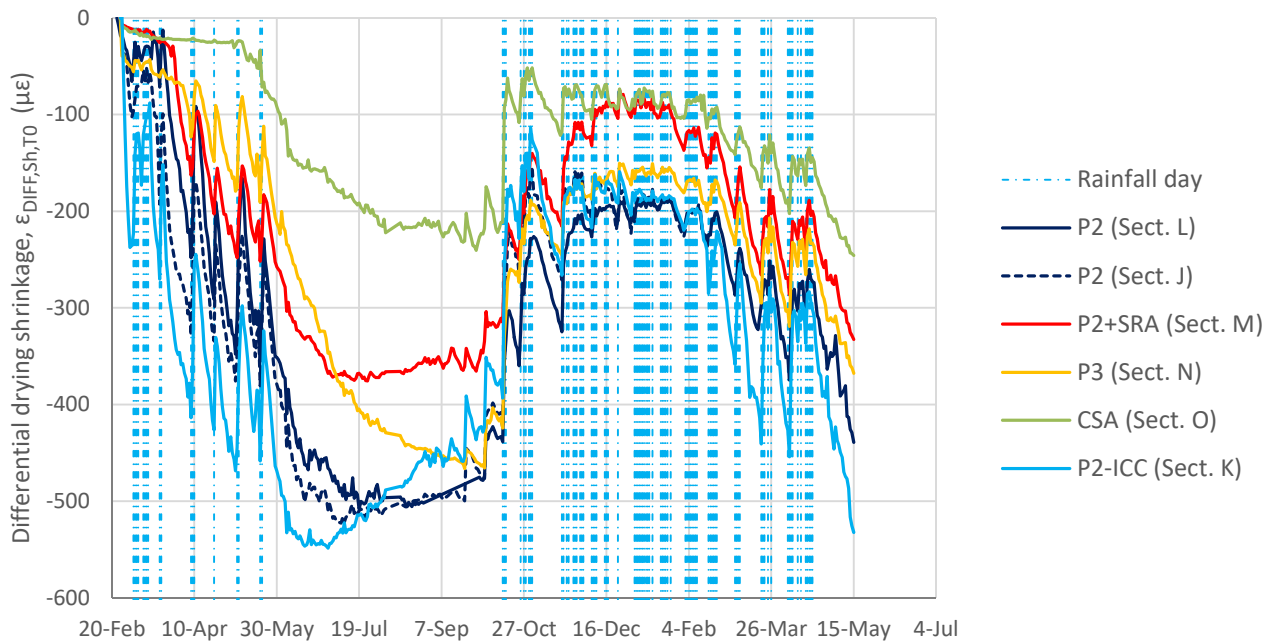


Figure 3.37: Moisture-related shrinkage determined in the laboratory (ASTM C157-08).

Ranking of Mixes and Curing Procedures Based on Differential Drying Shrinkage

Strain was measured with vibrating wire strain gages (VWSGs) located at the top and bottom of the concrete overlay, at three different locations within one slab in each environmental section (and two slabs in Section L). Differential strain is the difference between the strains at the top and bottom of the slab, and it was calculated for each pair of strain gages as indicated in Figure 3.25. As noted earlier, differential strain is assumed to have two components, one related to temperature gradients and one related to moisture. The moisture-related component, $\epsilon_{DIFF,Sh,T0}$, is referred to as *differential drying shrinkage* in this report, since it is caused by top-down drying of the concrete.

The differential drying shrinkage can be used as an indication of the drying susceptibility of the different mixes and curing procedures. It should be noted that the differential drying shrinkage is not exclusively related to the mix and curing procedure since it is also determined by the locking or lack of deployment of the transverse joints and the restriction imposed by the slab's weight and the slab's interaction with the asphalt base. This restriction is lower at the corners than at the center of the slabs, and so the differential drying shrinkage values determined for the pairs of longitudinal strain gages located at the corners have been used here to evaluate the drying shrinkage of the mixes and curing procedures. The results of this evaluation are shown in Figure 3.38.



Note: For each section, the plot reflects the average outcome determined for the two pairs of longitudinal strain gages located at the corners (four pairs of strain gages for Section L).

Figure 3.38: Differential drying shrinkage of the BCOA sections ($\epsilon_{DIFF,Sh,T0}$).

An important point to remember to understand Figure 3.38 data is that the slabs are almost fully restricted to bend in the longitudinal direction before the transverse joints deploy. This is why, for example, the results for Section N, with P3 concrete, show minimal differential drying shrinkage until April, when its transverse joints started to deploy.

A main conclusion to be drawn from Figure 3.38 is that the estimates of differential drying shrinkage for all the mixes were very high, except for the CSA concrete. When partially restricted, this differential strain will potentially result in very high tensile stresses at the top of the slabs.

The CSA mix had the best moisture-related performance in terms of differential drying shrinkage. The same conclusion was reached based on the unrestrained shrinkage beams. Differential drying shrinkage started to grow in Section O (CSA) on June 2016, at the same time that the relative humidity sensors located at 20 mm (0.8 in.) depth in this section started showing evidence of desiccation (Figure 3.13 and Figure 3.14). The differential drying shrinkage in this mix increased relatively fast compared to the portland cement-based mixes during summer 2016. This conclusion was also reached in terms of internal relative humidity (Figure 3.13 and Figure 3.14). Because of the high drying rate during the summer, the CSA mix, along with P3 and P2-ICC mixes, presented the lowest RH among all the mixes at the end of September 2016. Nonetheless, the differential drying shrinkage was still much lower in the CSA mix than in the portland cement-based mixes at that time. These results are not necessarily contradictory, since the relationship between relative humidity and moisture-related shrinkage is mix dependent.

The internally cured mix, P2-ICC, presented the worse drying performance. In particular, the differential drying shrinkage in Section K (P2-ICC) was larger than in Section J (P2, same slab size, same curing approach). This outcome agrees with the conclusion reached on the basis of relative humidity measurements. As Figure 3.13 shows, the relative humidity at 20 mm (0.8 in.) depth was lower in the P2-ICC mix than in the P2 mix upon which its design is based.

The differential drying shrinkage was smaller in the P3 mix than in the P2 mix, both of which were cured with curing compound. This result was also obtained for the shrinkage beams, but it is not in line with relative humidity measured in the corresponding sections at 20 mm depth. As Figure 3.13 and Figure 3.14 show, RH at 20 mm depth was higher for the P2 mix than for the P3 mix. As explained above, however, these outcomes are not necessarily contradictory since the relationship between internal RH and moisture-related shrinkage is mix dependent.

The differential drying shrinkage was much smaller in Section M (P2 cured with SRA) than in the other sections where the P2 mix was cured with standard curing compound (Sections J and L). The beneficial effect of the topical SRA treatment in Section M was also verified in terms of internal relative humidity (Figure 3.13 to Figure 3.15). These outcomes were somewhat different from the result obtained on the unrestrained shrinkage beams (Figure 3.36). Based on results from these beams, the SRA treatment did not produce such a remarkable effect on the drying performance of the P2 mix. A definitive explanation has not been found for the fact that the SRA seemed to produce a different result in the BCOA section compared to the shrinkage beams. A possible explanation is that while the shrinkage beams were only cured on the top, they might also have been drying on the sides and bottom as well. This might have resulted in a lower effect of the SRA application compared to the BCOA sections where drying was exclusively top-down.

Except for Section N (P3), the differential drying shrinkage reached a plateau value during summer 2016 and then it started to decrease. This pattern was unrelated to lack of drying, as reflected by the relative humidity sensors located at 20 mm (0.8 in.) depth in these sections (Figure 3.13 to Figure 3.15). The pattern is related, at least in part, to the plateau that the drying shrinkage presented for all mixes in the laboratory (Figure 3.37). As Figure 3.37 shows, the drying shrinkage measured in the laboratory (23°C [73°F], 50 percent RH) remained relatively stable after 100 days of drying exposure. A possible explanation for the drop of differential drying shrinkage could be that the drying affected the bottom half of the slabs. Another possible explanation is creep/relaxation in the concrete. Differential drying shrinkage produces tensile stresses at the top of the slabs due to self-weight of the slabs. Because these tensile stresses are maintained over time, the concrete is expected to creep/relax. This creeping/relaxation results in a decrease in the absolute value of the differential strain.

Ranking of Mixes and Curing Procedures Based on Estimated Autogenous Shrinkage

Preliminary modeling of the BCOA sections indicated that drying shrinkage should not considerably affect the strain measured with the bottom strain gage of the 6×6 slabs. Drying shrinkage was modeled as an equivalent temperature reduction that has its maximum value (in absolute terms) at the overlay surface and decreases linearly versus depth until reaching zero at overlay half-depth (Figure 3.39). This approach is used in Hiperpav (12) and, for a 115 mm (4.5 in.) overlay thickness, it is similar to the MEPDG (11) approach. For the calculations, different asphalt base stiffnesses were used, all of which were within the range that might be expected for an asphalt base subjected to stresses caused by relatively slow moisture-related shrinkage in the concrete to which it is bonded. In all cases, the strain calculated at the location of the bottom strain gage was very small, as reflected in Figure 3.39. Based on this preliminary modeling, it was assumed that the moisture-related shrinkage measured with the bottom strain gages was mainly caused by autogenous shrinkage. The modeling resulted in the same

conclusion at the corner of the larger 12×12 slabs, i.e., drying shrinkage was not expected to considerably affect the strain measured with the bottom strain gages. However, slightly different results were obtained at the center of these full lane-width slabs. At this location, the models indicated that drying shrinkage would have some effect on the strain measured with the bottom strain gage. For this reason, autogenous shrinkage was estimated for these sections using only the VWSGs located at the corners.

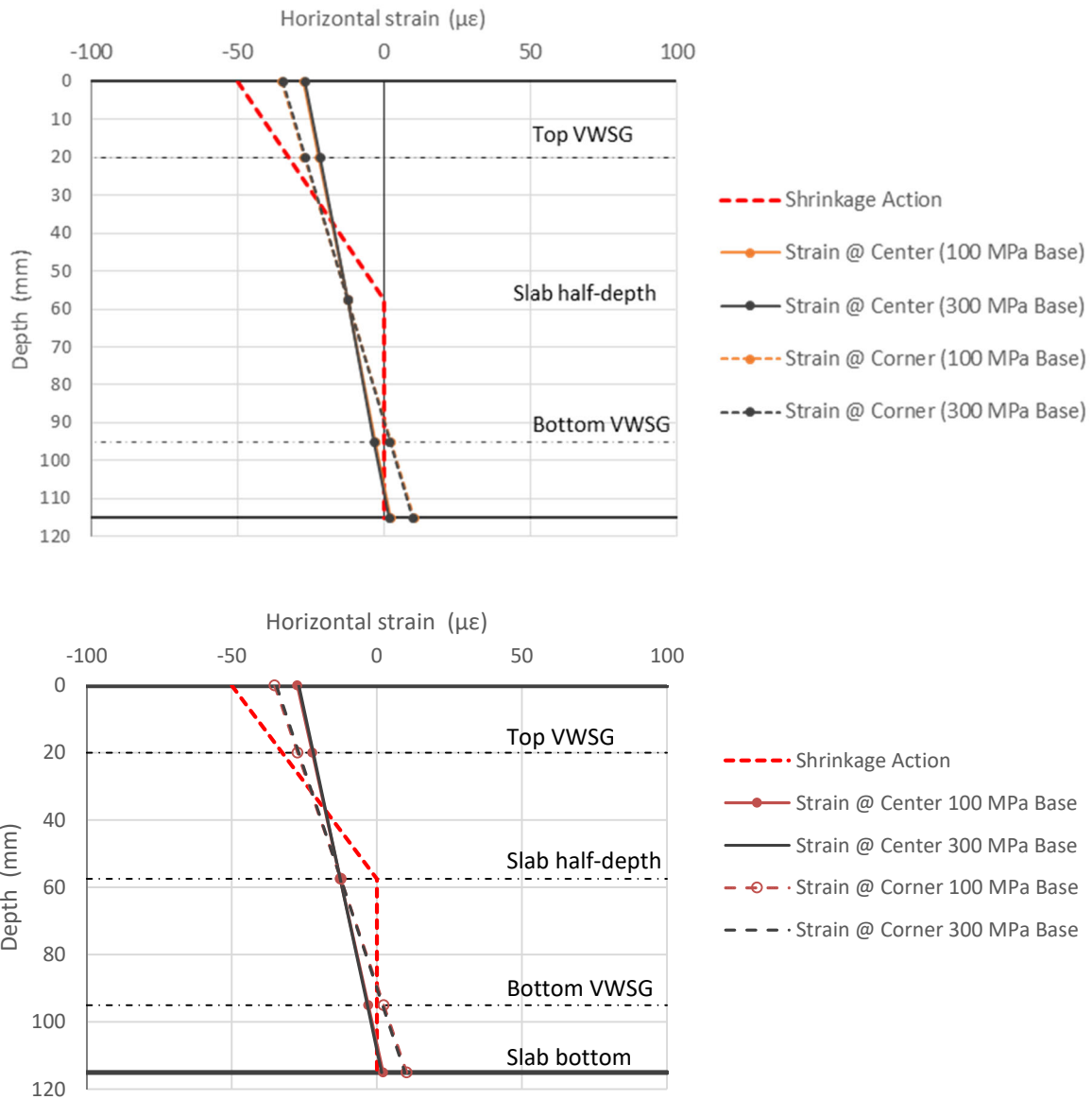
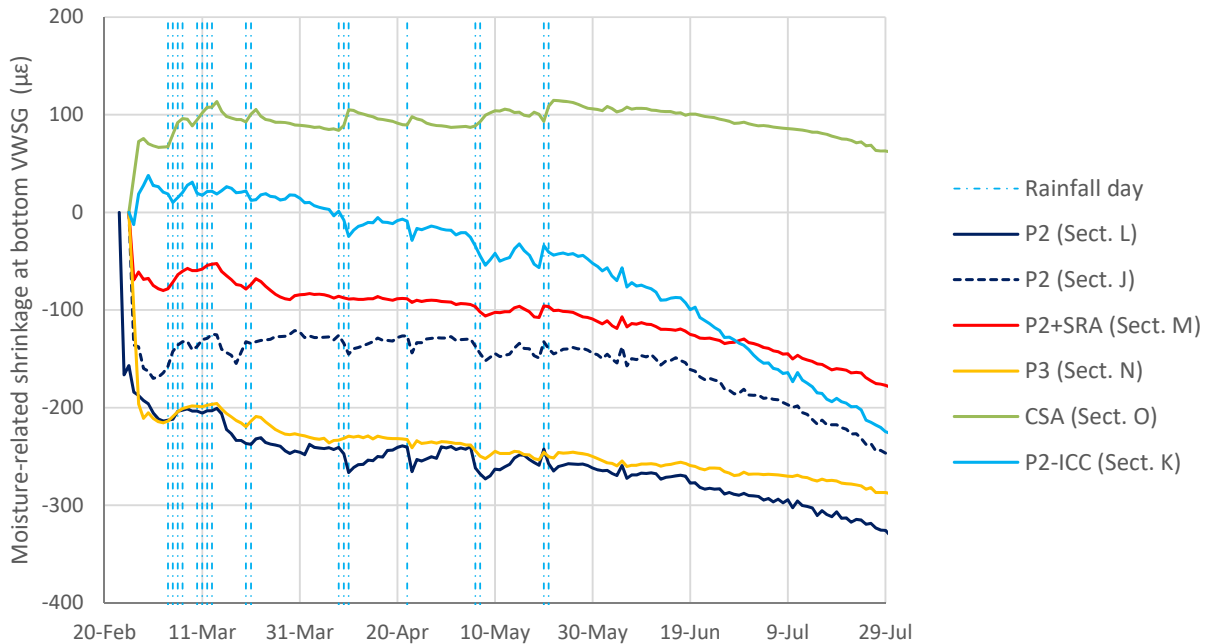


Figure 3.39: Preliminary modeling of slab response to drying shrinkage (6×6 slab).

Figure 3.40 shows the moisture-related component of the strain measured with the bottom strain gages in the different sections. As described above, this strain is regarded as an estimation of the autogenous shrinkage of the

mix for the preliminary analysis presented in this report. This strain is calculated using mean and differential moisture-related shrinkage ($\epsilon_{BOT-VWSG,Sh,T0} = \epsilon_{MEAN,Sh,T0} - 1/2 \cdot \epsilon_{DIFF,Sh,T0} \cdot 75/115$, see Figure 3.25), which were estimated following the procedure outlined in Section 3.4.2 of this report.



Notes: - For the 6×6 sections, the plot reflects the average outcome determined for all the bottom strain gages (eight VWSGs for Section L, four VWSGs for the rest of the sections). For Section J and K (12×12 slabs), the plot reflects the average of the bottom strain gages located at the corners (four VWSGs). Strain in this figure can be regarded, in a preliminary analysis, as an estimation of autogenous shrinkage.
 - Only data for 100 days are included in the figure since most autogenous shrinkage is expected to take place in the short term.

Figure 3.40: Moisture-related shrinkage at the bottom of the slabs.

As Figure 3.40 shows, the lowest autogenous shrinkage was obtained on the CSA mix. This mix actually resulted in a slight expansion. The highest autogenous shrinkage was obtained on the P2 and P3 mixes.

The estimated autogenous shrinkage in Section K (P2-ICC) was close to zero for approximately one month after overlay construction. This indicates that internal curing was effective in reducing autogenous shrinkage.

The estimated autogenous shrinkage was smaller in Section J than in Section L, both of which have P2 cured with curing compound. This result may be related to the relatively high water content of the P2 mix used in Section J. This hypothesis was also formulated in relation to the relatively low flexural strength that was measured for the mix used to build this section (the flexural strength of this mix was smaller than the flexural strength of the mix that was used to build Section L) (1). Also, the slump measured for the Section J mix, 11.5 inches, was clearly

over the maximum specified value of 9 inches (1). A relatively high water content would explain the lower autogenous shrinkage that resulted for the P2 mix in Section J compared to the P2 mix in Section L. As explained above, autogenous shrinkage is the result of the internal desiccation of the concrete due to cement hydration water demand and the net volume reduction resulting from cement hydration (chemical shrinkage). This self-desiccation increases as the water/cement ratio decreases.

The good performance of the P2 mix cured with SRA in Section M was unexpected. As Figure 3.40 shows, the estimated autogenous shrinkage in Section M was much smaller than in Sections J and L, where the same mix was cured with curing compound. The SRA supplied with the surface treatment was only expected to reach concrete in the top few millimeters (few in./10) of the slab, so a significant effect on overall slab contraction due to autogenous shrinkage was not expected. A definitive explanation was not found for this outcome.

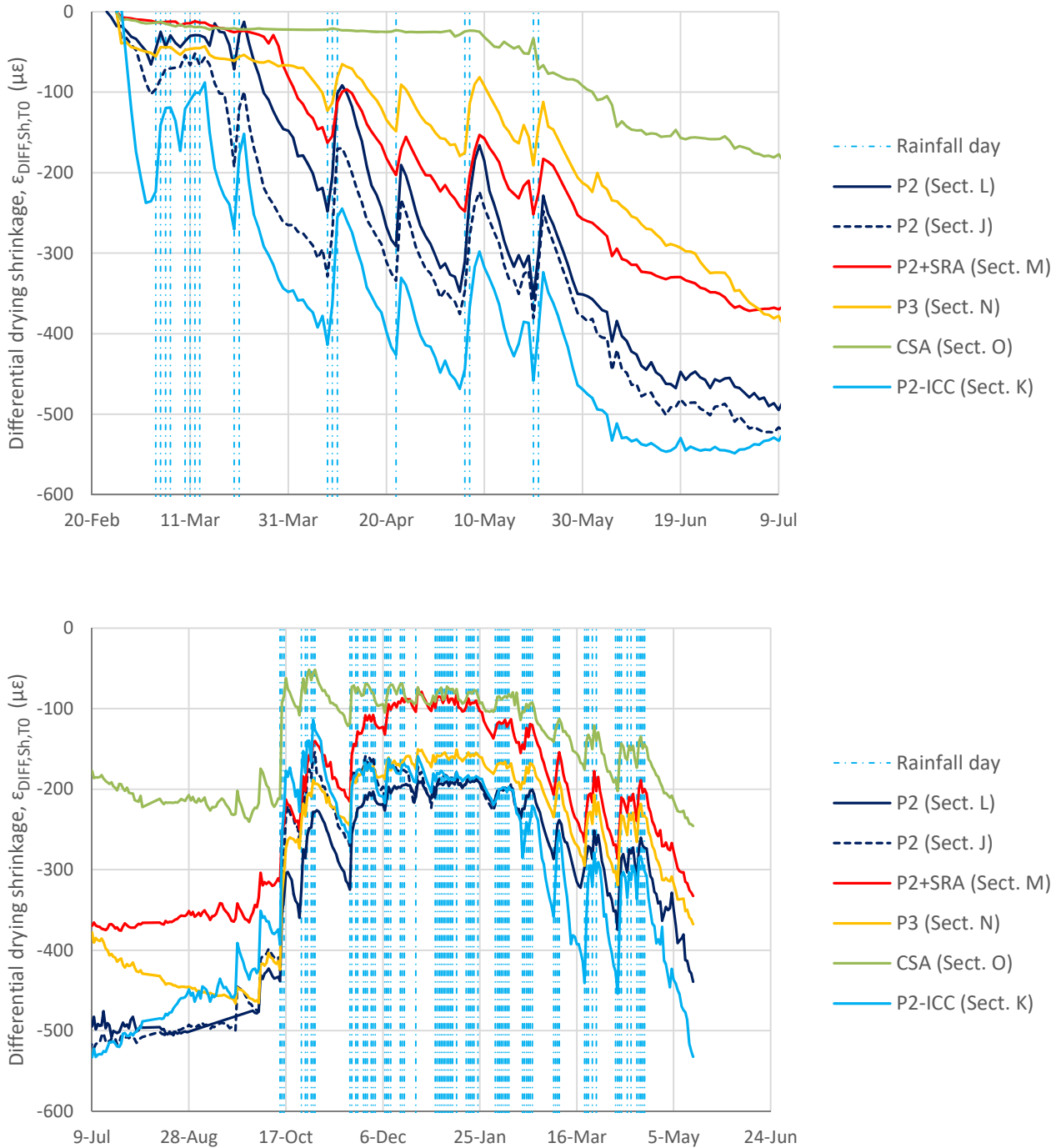
It should be noted that in Figure 3.40 most of the autogenous shrinkage developed within the first 24 hours after overlay placement. It should also be noted that 24 hours is the time at which the Jonasson and Hedlund autogenous shrinkage model (15), implemented in Hiperpav, assumes that autogenous shrinkage begins. However, it is clear that this hypothesis is not valid for the early high-strength mixes used for this BCOA construction. Moisture-related shrinkage at the bottom strain gages seemed to remain relatively stable for a few months after this initial growth, but this shrinkage started to increase during the summer. This increase is not related to autogenous shrinkage.

Based on the data in Figure 3.40, an autogenous shrinkage between 200 and 250 $\mu\epsilon$ was estimated for the P2 and P3 mixes. These values are in line with estimations based on the Jonasson and Hedlund autogenous shrinkage model (15), which is based on the water/cement ratio of the mix. This model results in 220 and 245 $\mu\epsilon$, respectively, for the P2 and P3 mixes.

Effect of Environmental Conditions on Differential Drying Shrinkage

Figure 3.38 above shows differential drying shrinkage estimated for the environmental sections using the approach described in Section 3.4.2 of this report. A close-up of the data in this figure is presented in Figure 3.41 below, where the impact of the environmental conditions can be better observed. The first conclusion is that rainfall events produce an almost immediate decrease in the magnitude of differential drying shrinkage. The same quick reaction was observed in terms of the relative humidity measured at 20 mm (0.8 in.) depth (Figure 3.13). However, because of the way the data have been analyzed it was not possible to better quantify the speed of this reaction

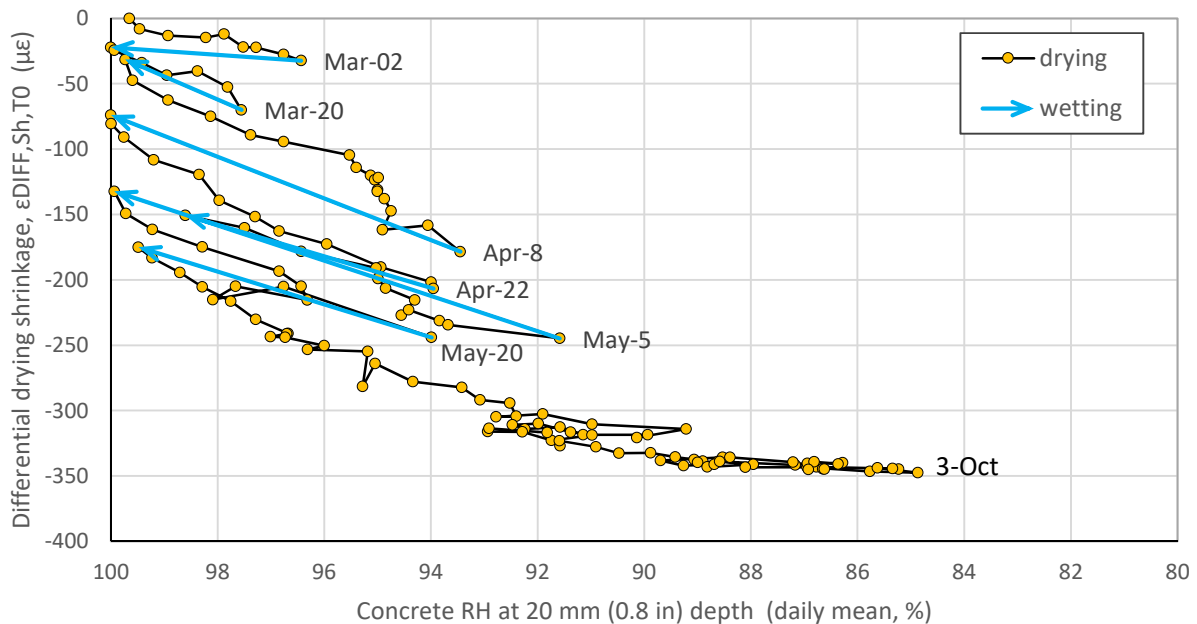
time. Also, the effect of rainfall on differential drying shrinkage did not seem to be related to the amount of precipitation, a fact that was also observed for relative humidity.



Note: For each section, the plot reflects the average outcome determined for the two pairs of longitudinal strain gages located close to the joints (four pairs of strain gages for Section L).

Figure 3.41: Differential drying shrinkage of the BCOA sections ($\epsilon_{DIFF,Sh,T0}$) (close-up of Figure 3.38).

One important difference was observed between the slabs' response in terms of differential drying shrinkage (Figure 3.41) and relative humidity (Figure 3.13); that is, after most periods of rainfall the relative humidity in the slabs fully recovered but differential drying shrinkage did not. Specifically, differential drying shrinkage did not disappear when the relative humidity, at 20 mm [0.8 in.] depth, returned to 100 percent. This phenomenon indicates that drying shrinkage is not an elastic deformation, a result that is in line with the results shown in laboratory experimental studies (16). This mechanical behavior also implies that a direct relationship between RH and drying shrinkage does not exist. An example of this can be seen in Figure 3.42, which shows differential drying shrinkage versus relative humidity measured at 20 mm (0.8 in.) depth in Section L (P2 mix). The figure shows wet periods, which are defined as days where average RH increased versus previous day, as blue arrows. This figure clearly shows that the response of the slabs to drying (that is, a decrease in the relative humidity of the concrete) is not elastic.



Notes: - Wetting data correspond to days when RH increased, while drying data include the rest of the days. All wetting periods are related to rainfall events.

- Each point in the graph corresponds to one day. RH is average during each day.

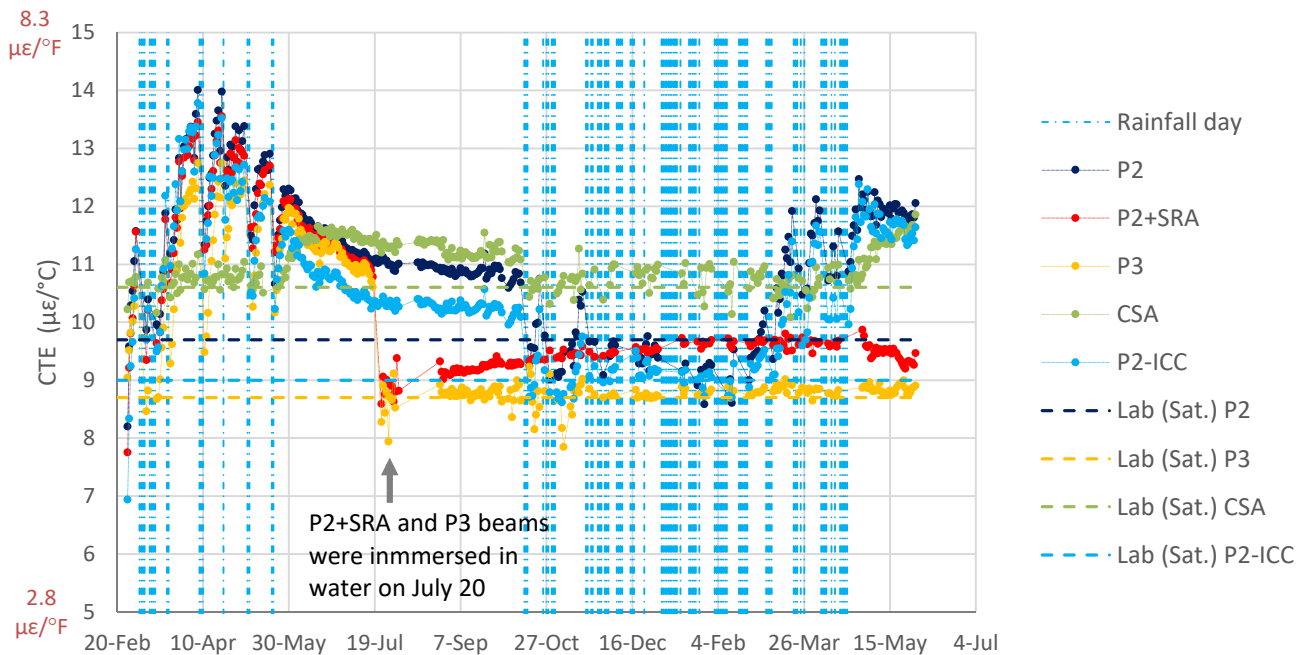
Figure 3.42: Differential drying shrinkage versus relative humidity (Section L).

Effect of Environmental Conditions on Concrete Coefficient of Thermal Expansion

As was discussed in Section 3.4.2, a model was used to fit the strains measured with the VWSG sensors in the unrestrained shrinkage beams. In that model, the CTE of the concrete was assumed to be constant during a single day, but it was allowed to change from one day to another. Also, since the unrestrained shrinkage beams were free

to expand and contract, the CTE value backcalculated for each day can be regarded as an estimate of the average coefficient of thermal expansion of the concrete in the beam for the moisture conditions during that specific day. The CTE values backcalculated for each type of mix and curing procedure are shown in Figure 3.43. A close-up of the data in this figure is presented in Figure 3.44, where the impact of the environmental conditions can be better observed.

Figure 3.43 and Figure 3.44 clearly show that the CTE of concrete changes in parallel with environmental conditions. The CTE repeatedly increased during periods without rainfall, except for the summer. The same pattern has been shown in laboratory studies, where the CTE of concrete increased as the concrete moisture decreased, up to a certain point. Beyond that point, where the CTE reached a maximum, the CTE decreased with further drying (14). A relative maximum was seen for all the portland cement-based mixes at the beginning of June and somewhat later for the CSA concrete. It is very likely that the same phenomena are behind this relative maximum and the absolute maximum that the laboratory studies showed.



Notes: - Lab CTE was determined under saturated conditions, following AASHTO T 336-15.
 - The backcalculated CTE are not shown for the days when rainfall occurred. The strain model assumes moisture-related shrinkage changes linearly during each day. It also assumes that CTE is constant during each day. The two hypotheses may be very unrealistic if rainfall takes place. For this reason, the backcalculated CTE parameters were not regarded as a reliable estimate of concrete CTE for these specific days. For similar reasons, the backcalculated CTE are not shown for those days where temperature fluctuation inside the unrestrained shrinkage beams was lower than 5°C (9°F).

Figure 3.43: CTE backcalculated for the unrestrained shrinkage beams.

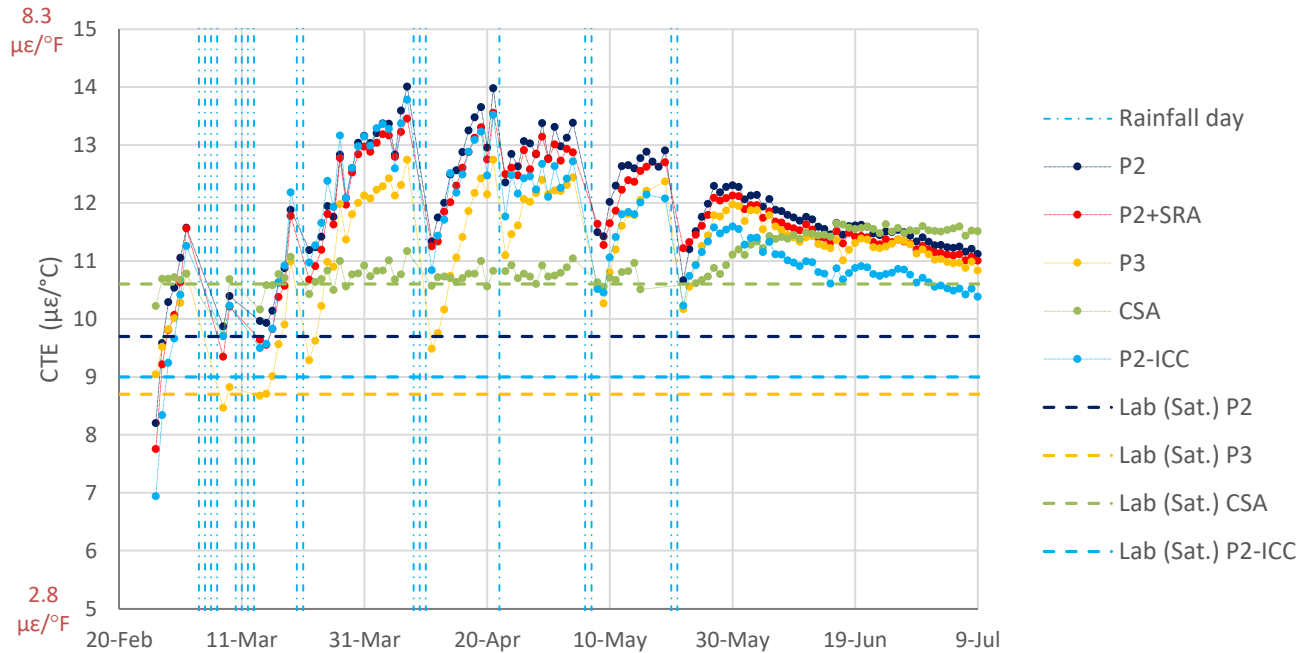


Figure 3.44: CTE backcalculated for the unrestrained shrinkage beams (close-up of Figure 3.43).

Figure 3.43 and Figure 3.44 show that CTE decreased after the periods of rainfall. The quick decrease in CTE after rainfall events is likely related to the rapid reaction to rainfall events that was observed in terms of relative humidity at 20 mm (0.8 in.) depth (Figure 3.13) and also in terms of differential drying shrinkage (Figure 3.38).

Figure 3.43 and Figure 3.44 also show that the backcalculated CTE was repeatedly higher than lab CTE, particularly after dry periods. This result was expected, since the lab CTE was determined under saturated conditions, following AASHTO T 336-15. An obvious but very important conclusion that can be drawn from Figure 3.43 and Figure 3.44 is that thermal deformations of the beams were much higher, up to 50 percent higher, than the values that would have been predicted using the CTE determined in the laboratory under saturated conditions.

An interesting observation from Figure 3.43 and Figure 3.44 is that the backcalculated CTE of the CSA mix remained very close to the laboratory (saturated) CTE up until the beginning of June 2016, when it started to increase. The beginning of June is when the relative humidity sensors located at 20 mm (0.8 in.) depth in Section O (CSA) started showing evidence of desiccation (Figure 3.13 and Figure 3.14), and also when the differential drying shrinkage in the same section started to grow. As expected, the backcalculated CTE returned to the laboratory value when the rainfall season started in October 2016.

The unrestrained shrinkage beams of the P2 mix cured with SRA and the P3 mixes were immersed in water on July 20, 2016. The water bath was outdoors, at the same location where the rest of shrinkage beams were placed. This allowed the P2+SRA and P3 beams to be subjected to diurnal temperature changes so that the same model described in Section 3.4.2 could be used to backcalculate the moisture-related shrinkage and the CTE. It turned out that the CTE of these specimens was drastically reduced after immersion, down to values that were very close to the CTE for saturated conditions determined in the laboratory. This result was expected, since in both cases the concrete was saturated.

Deployment of Transverse Joints

The deployment of the transverse joints was evaluated by conducting periodic visual assessments. As an example, a crack propagating down at Joint 1 of Section K is presented in Figure 3.45.

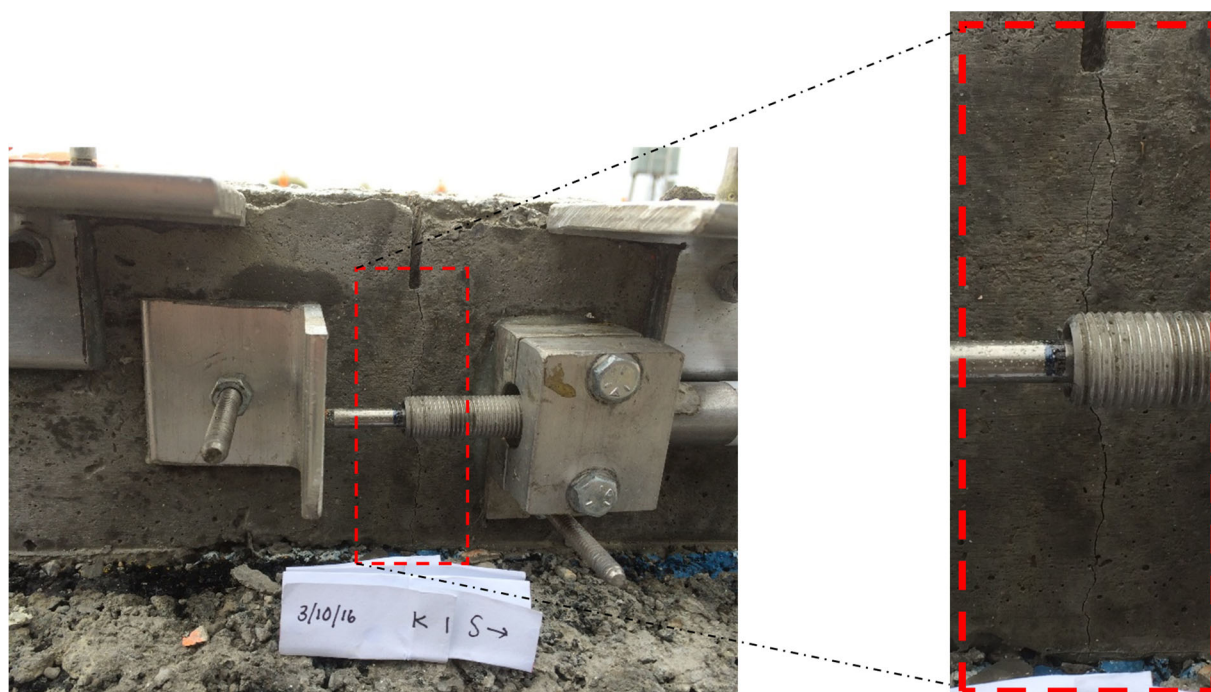
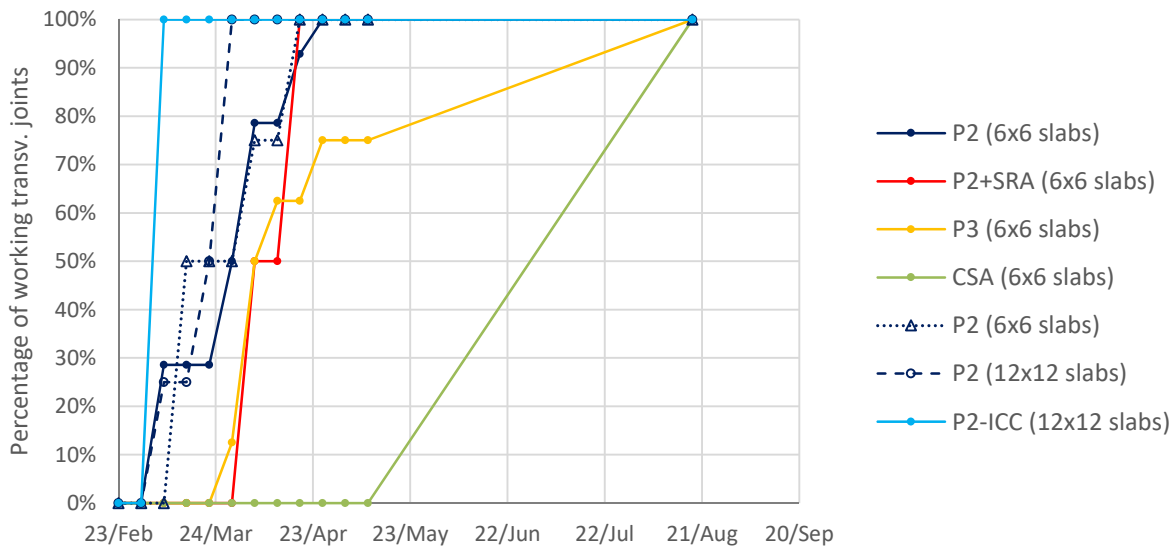


Figure 3.45: Example of active joint (Section K).

As Figure 1.1 shows, the BCOA sections were relatively short. The sections with 6×6 slabs were 9 m (30 ft) long to accommodate five slabs in the longitudinal direction. The two sections with 12×12 slabs were 10.8 m (36 ft) long to accommodate three slabs in the longitudinal direction. The sections' ends were intentionally disconnected from the intermediate slabs between sections to prevent the performance and structural response of one section from interfering with the adjacent sections. For this reason, the first and last transverse joints of all the sections were full-depth joints made by either disposing of one of the wooden forms used in construction before the

placement of the concrete, or by cutting a full-depth joint after the concrete had set. Because of the sections' short length—compared to a standard road—it was expected that not all the joints in the 6×6 sections would deploy. Nonetheless, it turned out that all joints deployed, as shown below.

The percentage of active joints in each section type is presented in Figure 3.46. In determining the values shown in this figure, all the test track sections of each section type were included. For example, the percentage of working joints shown for the P3 mix, 6×6 slabs, are the results averaged from Section G (HVS type) and Section N (ENV type). Similarly, the percentages for the P2 mix with 6×6 slabs are an average of ENV Section L and HVS Sections A, B, C, E, F, and I. The results shown in Figure 3.46 only include the two transverse joints of the mid-slabs of each section. Although the sections with 6×6 slabs have four transverse joints (five slabs in the longitudinal direction), only the deployment of transverse joints 2 and 3 is presented in the figure (the naming convention is shown in the appendix of this report). The reason to report joint deployment only for these locations that is it is believed that they better represent field BCOA than the joints at the beginning and end of the sections.



Note: No visual assessment was conducted between May 5 and August 8, 2016.

Figure 3.46: Transverse joint deployments in the BCOA sections.

As Figure 3.46 shows, all the joints deployed by August 2016. The first section where joints deployed was Section K, a full lane-width design with P2-ICC. As was shown in Figure 3.38, the differential drying shrinkage was somewhat higher for the P2-ICC mix than for the P2 mix. The strength of the P2-ICC mix was less than that of the P2 mix (1). These two facts, together with the slab size, explain why Section K was the first one where joints deployed.

The P2 sections cured with curing compound showed joint deployment after Section K. As expected, the order in which the P2 sections showed that joints deployed was determined by the size of the slabs. Section M, where the P2 mix was cured with SRA, showed joint deployment later than sections that had the same geometry but where the P2 was cured with curing compound. This outcome is in line with the lower differential drying shrinkage that was estimated for Section M compared to Sections J and L (Figure 3.38).

The transverse joints in P3 Sections H and N deployed considerably later than joints in the P2 sections with the same geometry (6×6 slabs) and curing procedure. This result is in line with the lower differential drying shrinkage that was estimated for the P3 mix compared to the P2 mix, as shown in Figure 3.36 (unrestrained shrinkage beams) and Figure 3.38 (BCOA sections). It is also compatible with the lower drying shrinkage that was measured in the laboratory for the P3 mix compared to the P2 mix (Figure 3.37).

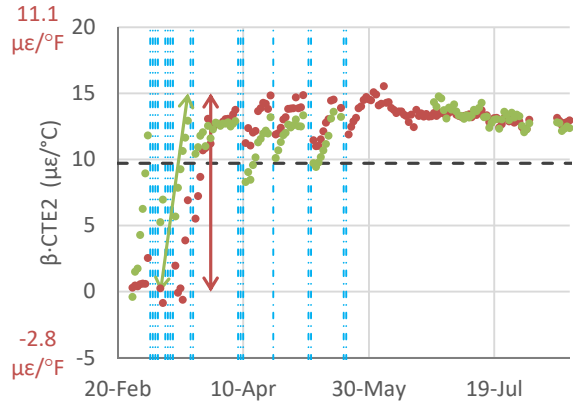
As expected, the CSA sections (H and O) deployed joints later than any other type of section. These joint deployments took place in the CSA sections between May 5 and August 8, 2016, which means that no cracking was observable May 5 and that all of them were visible on August 8. Unfortunately, no visual assessment was conducted between those two dates. This is the approximate period when the RH and VWSG sensors started to show evidence of drying in Section O.

As noted, only the two transverse joints at mid-slab of each section were used for the analysis presented in Figure 3.46. It should be mentioned, however, that with the exception of three out of eight transverse joints in the two CSA sections, cracks were observed at all the transverse joints (not only those at mid-slab) of all the sections during the visual assessment on August 8, 2016. This high level of joint deployments is related to the high drying shrinkage levels that were estimated for all mixes.

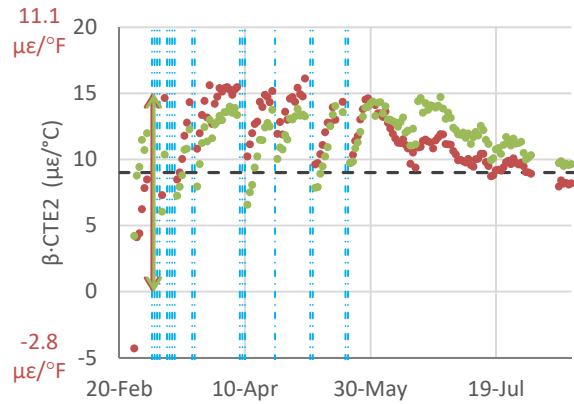
A preliminary analysis was conducted in order to evaluate how the deployment of the transverse joints would affect the response of the environmental sections to temperature gradients through the slab depth. In theory, temperature gradients should produce little bending, if any, before the transverse joints deploy. This means that thermal bending compliance (the ratio of differential thermal strain to ELTD, i.e., $\beta \cdot CTE2$) should be small until joint deployment. As transverse joints deploy, the thermal bending compliance determined for the pairs of strain gages located at the corners should increase and reach a maximum when the joints are fully cracked. The results of the analysis are shown in Figure 3.47, where the backcalculated $\beta \cdot CTE2$ values are included for each of the ENV sections. Figure 3.47 shows that there is a clear link between joint deployment, which was evaluated by visual assessments, and thermal bending compliance of the slabs evaluated on the basis of VWSG data. This result

was expected. In most cases, the VWSG data anticipated the results of visual assessments, which means that the transverse joints started to work before vertical cracks were visible below the joint cuts at slabs edges.

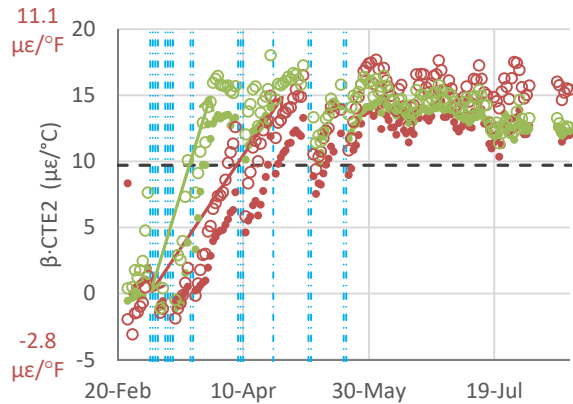
Lab CTE values are also shown in Figure 3.47. If the CTE of the concrete were constant, $\beta \cdot \text{CTE}_2$ of the slabs should approach the lab CTE of the corresponding mix as the joints deploy. What Figure 3.47 shows is that $\beta \cdot \text{CTE}_2$ reached values that were considerably higher than the CTE determined in the lab for the corresponding mix. This outcome is in line with results obtained for the unrestrained shrinkage beams (Figure 3.43 and Figure 3.44). As explained above, this agrees with experimental laboratory studies showing that as concrete dries its CTE can reach values considerably higher than under saturated conditions (14). Consequently, $\beta \cdot \text{CTE}_2$ reflects not only joint deployment (through β) but also moisture-related changes in concrete CTE. As Figure 3.47 shows, $\beta \cdot \text{CTE}_2$ was reduced considerably after periods of rainfall for all the mixes based on portland cement. An interesting result is that $\beta \cdot \text{CTE}$ in Section M, where the topical SRA treatment was used, did not change with drying-wetting as much as it changed in the P2 sections cured with curing compound. This outcome was not observed for the shrinkage beams. Again, SRA treatment seemed to have produced a different effect on the section than in the unrestrained shrinkage beams.



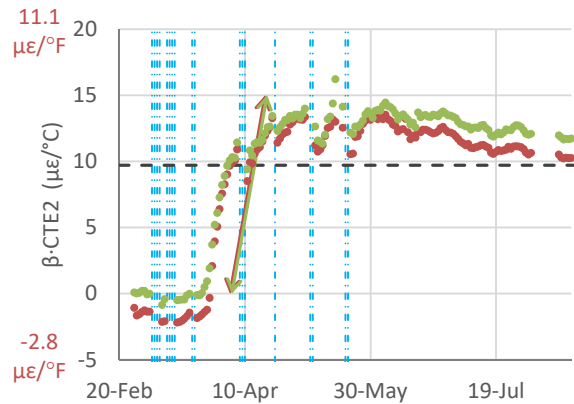
Section J, P2, 12x12 Slabs 3.6x3.6 m²



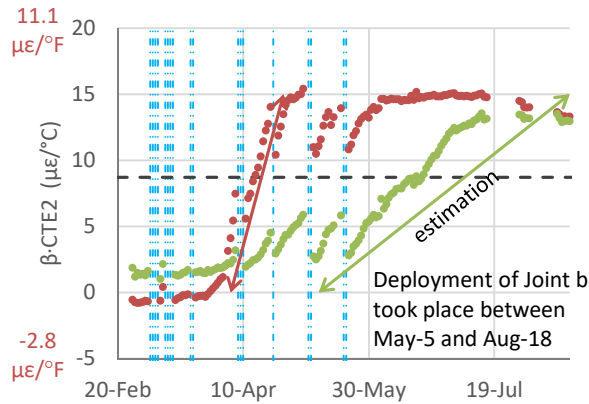
Section K, P2-ICC, 12x12 Slabs



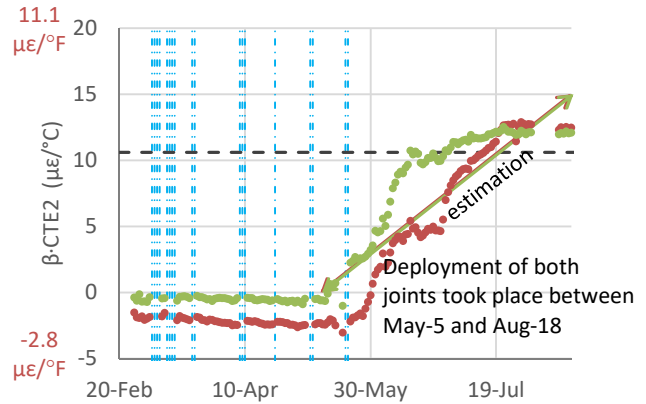
Section L, P2, 6x6 Slabs



Section M, P2, 6x6 Slabs



Section N, P3, 6x6 Slabs



Section O, CSA, 6x6 Slabs

- - - Rainfall day • β -CTE2 @ Joint a • β -CTE2 @ Joint b
 - - - Lab CTE \longleftrightarrow Joint a deployment \longleftrightarrow Joint b deployment

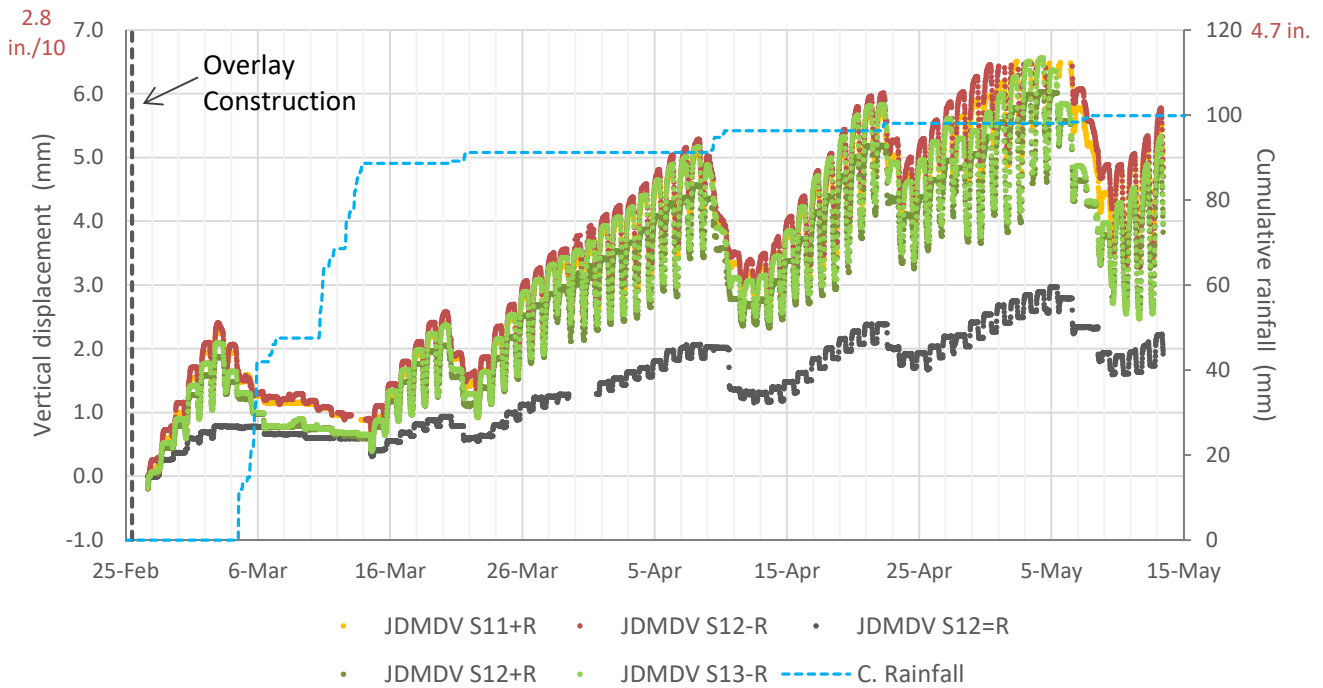
Notes: - Each joint deployment series extends from the time the crack was first observed on one side of the joint (usually the south side) until the time it was observed on the other side.
 - No visual assessment was conducted between May 5, 2016, and August 8, 2016, so the deployment of one joint in Section N and the two joints in Section O were missing.

Figure 3.47: Effect of transverse joint deployment on thermal bending compliance of the slabs.

3.5 Data Collected by the JDMD and IOMD Sensors

3.5.1 Examples of Collected Data

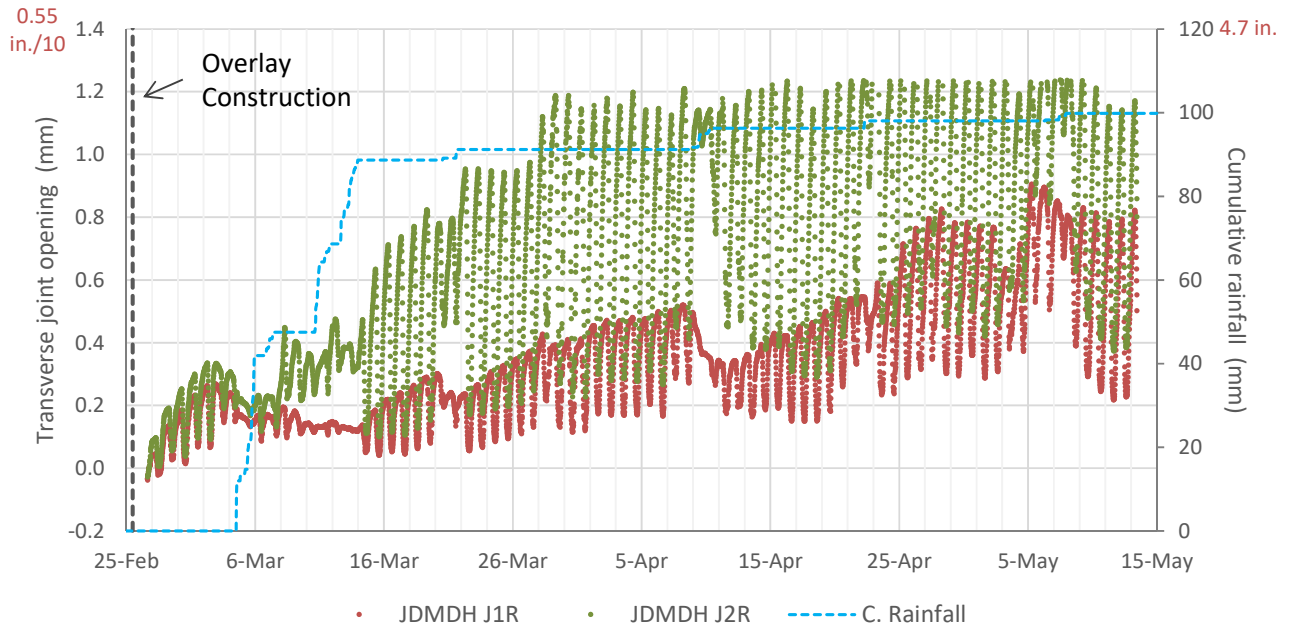
Figure 3.48 to Figure 3.50 show examples of the data collected with the LVDT sensors in Section K. Specifically, Figure 3.48 shows data collected with the vertical JDMDs located at the shoulder edge of the section, Figure 3.49 shows data collected with the two horizontal JDMDs that measure the opening/closing of transverse joints, and Figure 3.50 shows data collected with the two IOMDs that measure the opening/closing of the concrete-asphalt interface. As expected, the slab corners and edges moved upward and the transverse joints and the concrete asphalt interface tended to open in the mid- and long-term due to moisture-related shrinkage. As was also expected, downward corner movements and joint closings were mainly experienced during daytime, and the opposite during nighttime, in both cases due to the diurnal variations of slab temperature. The same pattern is present in the rest of the sections, although the displacements were smaller than in Section K. Section K presented higher displacements than the other sections because its slab size was 12×12, which is twice the length of the slabs of the other ENV sections instrumented with JDMDs. Another set of examples, this time for a 6×6 section, are included in Figure 3.51 to Figure 3.53.



Notes: - Positive displacement is upward.

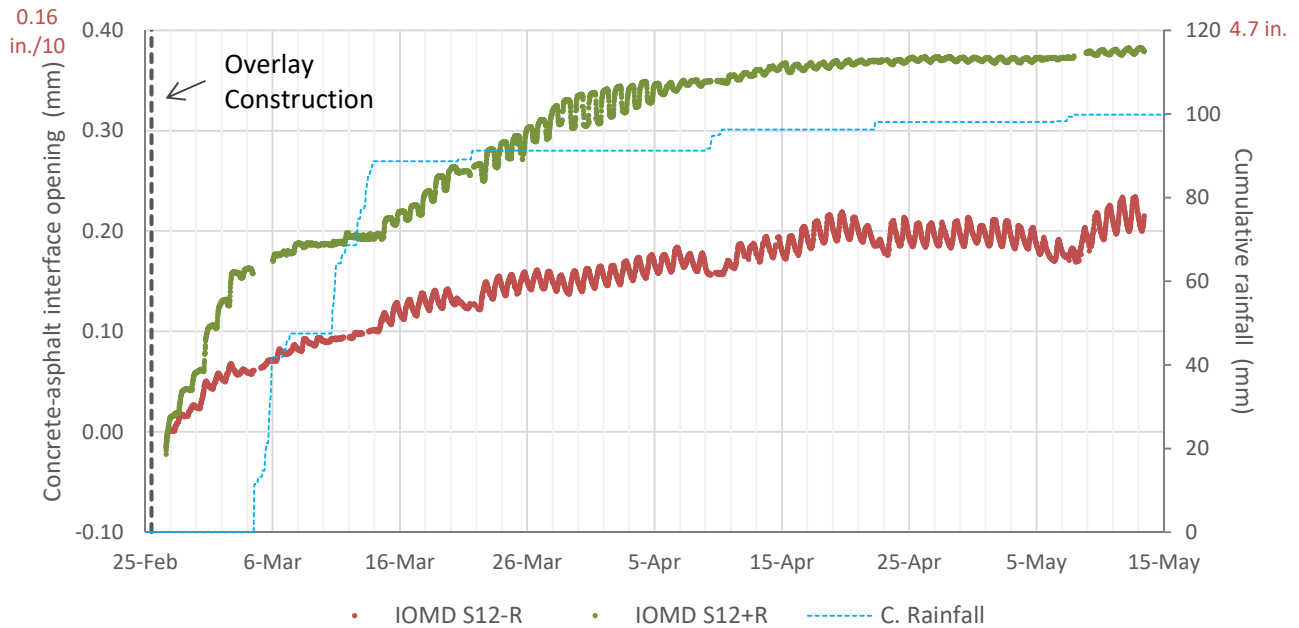
- All sensors are located at the shoulder edge of the slabs. An “-R” or “+R” at the end of the sensor label indicates its location is a slab shoulder corner; similarly, an “=R” indicates a mid-slab location. See the instrumentation layout in Figure 2.3.

Figure 3.48: Example of readings from vertical JDMDs in a section with 12×12 slabs (Section K).



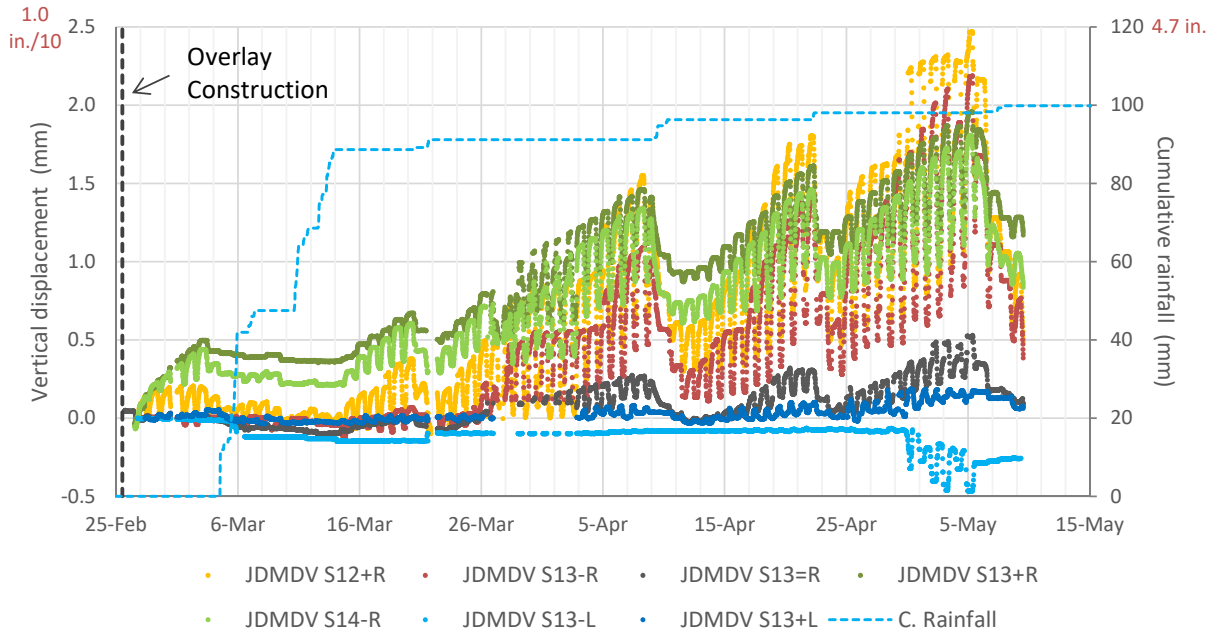
Note: The sensors are located at each of the two transverse joints of Section K, in both cases at the shoulder edge of the transverse joints. See the instrumentation layout in Figure 2.3.

Figure 3.49: Example of readings from horizontal JDMDs in a section with 12×12 slabs (Section K).



Note: The sensors are located at the shoulder corners of the middle slab of Section K. See instrumentation layout in Figure 2.3.

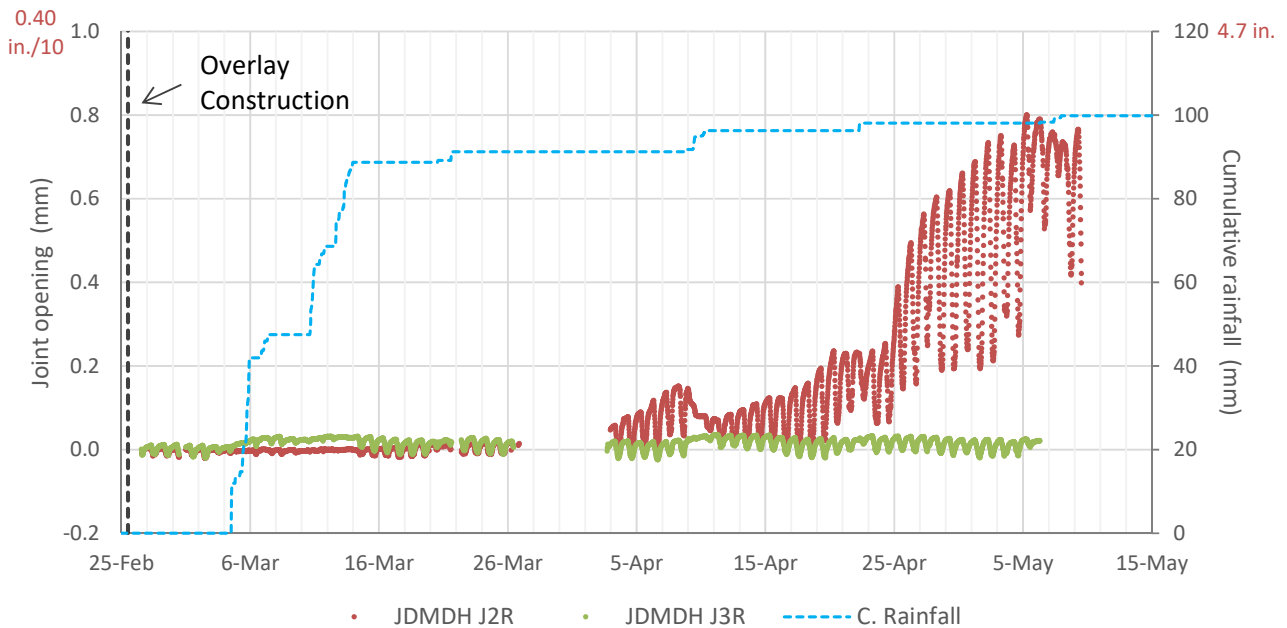
Figure 3.50: Example of readings from IOMDs in a section with 12×12 slabs (Section K).



Notes: - Positive displacement is upward.

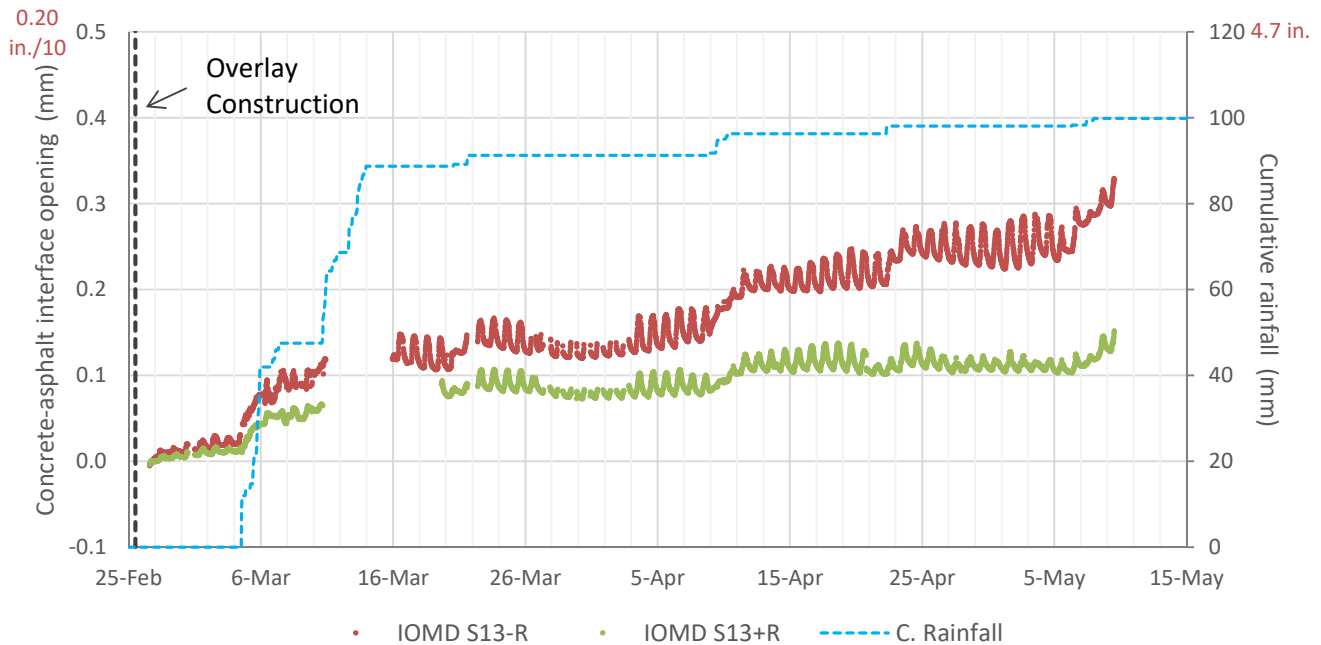
An “-R” or “+R” at the end of a sensor label indicates that its location is a slab shoulder corner; an “-L” or “+L” at the end of the label indicates a location at a slab interior corner; and an “=R” at the end of the label indicates a location at the shoulder edge of the middle slab, at mid-slab. See instrumentation layout in Figure 2.3.

Figure 3.51: Example of readings from vertical JDMDs in a section with 6x6 slabs (Section N).



Note: The sensors are located at each of two transverse joints of Section N, in both cases at the shoulder edge of the transverse joints. See instrumentation layout in Figure 2.3.

Figure 3.52: Example of readings from horizontal JDMDs in a section with 6x6 slabs (Section N).



Note: The sensors are located at the shoulder corners of the middle slab of Section K. See instrumentation layout in Figure 2.3.

Figure 3.53: Example of readings from IOMDs in a section with 6×6 slabs (Section N).

It should be noted that in the preceding figures the data from the LVDTs were only collected up to May 13, 2016. On that date the JDMD and IOMD sensors had to be removed to build the shoulders of the BCOA sections so that the HVS could be brought onto the sections. As noted in Section 2.3, these sensors were reinstalled in Sections L and N in January 2017, although only LVDT data collected during the initial phase (February to May 2016) have been analyzed and presented in this report.

It should be also noted that no LVDT data were collected during or right after overlay construction. As was mentioned in Section 2.3, the installation of the LVDT-based sensors (JDMDs and IOMDs) was relatively time-consuming and could not be conducted before saw-cutting operations. Since the JDMDs and IOMDs could not be installed before the field setting time of the different sections, this time could not be used as a reference for determining displacements. Instead, a reference time (t_1) was chosen for each ENV section when all the JDMDs and IOMDs of the section were installed and collecting data. The reference time for Section L was 6:00 p.m. on February 23, 2016, which was around eight hours after the concrete field setting time in this section. The reference time for the rest of the ENV sections was 6:00 p.m. on February 26, 2016, which was approximately 24 hours (it changed from section to section) after the field setting time in the different sections. The LVDT data in this report were determined versus the reference time, i.e., LVDT measurements are zero at the reference time (t_1).

3.5.2 Data Analysis

LVDT data were analyzed by following the same approach that was used for the VWSGs. The models used to fit the LVDT data were essentially the same models used to fit the VWSG data. The final expressions of these models, which were also formulated incrementally, are shown in Equations [8] to [10] below.

$$\text{Model for vertical JDMDs} \quad \Delta U_V = \Delta U_{V,Sh,T1} + \gamma \cdot \text{CTE3}(t) \cdot \Delta \text{ELTD} \quad [8]$$

where: U_V is the deflection measured with the JDMD ($U_V=0$ at time t_1);
 $U_{V,Sh,T1}$ is the moisture-related component of U_V at the reference temperature $T1$;
 γ is a coefficient that reflects 1) the restriction to slab warping due to slab weight, slab interaction with the asphalt base, and transverse joint locking or lack of deployment and 2) the geometry and configuration of the overlay (γ units are [L]);
 $\text{CTE3}(t)$ is time-dependent equivalent CTE of the concrete slab;
 t is time;
 t_1 is the reference time, when the JDMD started to collect data;
 $T1$ is slab temperature distribution at t_1 ; and
 ELTD is the equivalent linear temperature difference in the slab.

$$\text{Model for horizontal JDMDs} \quad \Delta U_H = \Delta U_{H,Sh,T1} + \delta \cdot \text{CTE4}(t) \cdot \Delta T_{\text{MEAN}} \quad [9]$$

where: U_H is the opening-closing measured with the JDMD ($U_H=0$ at time t_1);
 $U_{H,Sh,T1}$ is the moisture-related component of U_H at the reference temperature $T1$;
 δ is a coefficient that reflects 1) the restriction to joint opening-closing due to slab weight, slab interaction with the asphalt base, and transverse joint locking or lack of deployment and 2) the geometry and configuration of the overlay (δ units are [L]);
 $\text{CTE4}(t)$ is the time-dependent equivalent CTE of the concrete slab;
 t is time
 t_1 is the reference time, when the JDMD started to collect data;
 $T1$ slab temperature distribution at t_1 ; and
 T_{MEAN} is mean slab temperature.

$$\text{Model for IOMDs} \quad \Delta I = \Delta I_{Sh,T1} + \varphi \cdot \text{CTE5}(t) \cdot \Delta \text{ELTD} \quad [10]$$

where: I is the opening-closing measured with the IOMD ($I=0$ at time t_1);
 $I_{Sh,T1}$ is the moisture-related component of I at the reference temperature $T1$;
 φ is a coefficient that reflects 1) the restriction to slab warping due to slab weight, slab interaction with the asphalt base, and transverse joint locking or lack of deployment, 2) the geometry and configuration of the overlay, and 3) the condition of concrete-asphalt interface (φ units are [L]);
 $\text{CTE5}(t)$ is the time-dependent equivalent CTE of the concrete slab;
 t is time;
 t_1 is the reference time, when the IOMD started to collect data;
 $T1$ is the slab temperature distribution at t_1 ; and
 ELTD is the equivalent linear temperature difference in the slab.

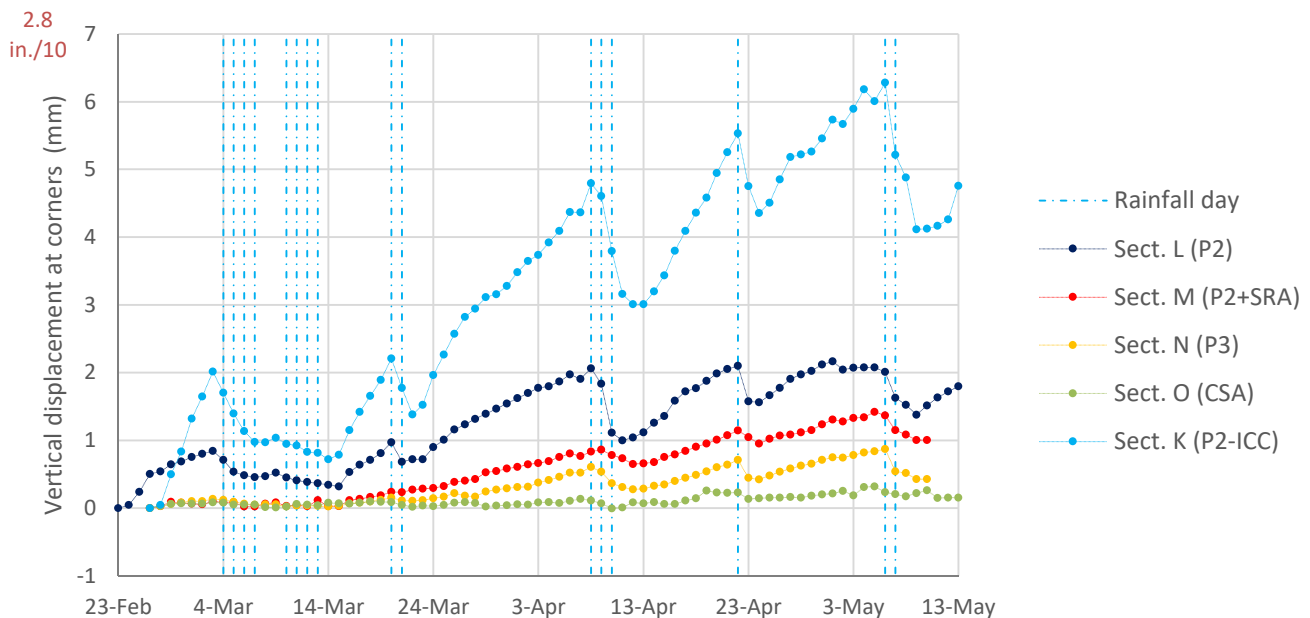
3.5.3 Preliminary Conclusions

Ranking of Mixes and Curing Procedures Based on Corner Displacements

Figure 3.54 shows the moisture-related component of the displacements measured with the vertical JDMDs located at the corners of each ENV section. For Section K, which has a slab size of 12×12, the data in Figure 3.54 are the average of four vertical JDMDs located at slab-shoulder corners. For the rest of the sections, all of which have a 6×6 slab size, the data in Figure 3.54 are the average of the four vertical JDMDs located at the slab-shoulder corners and the two vertical JDMDs located at the interior corners, as shown in Equation [11]. It should be noted that the vertical displacements measured with the JDMDs located at the interior corners of the 6×6 sections were much smaller than the displacements measured at the exterior corners. This can be seen in the example in Figure 3.51. Section K did not have interior corners since its slabs were full-lane width.

$$U = \frac{\frac{U_{S12+R} + U_{S13-R} + U_{S13+R} + U_{S14-R}}{4} + \frac{U_{S13-L} + U_{S13+L}}{2}}{2} \quad [11]$$

where: U is the average moisture-related corner displacement of the section, and
 U_i is the moisture-related component ($U_{V,Sh,T1}$) of the displacement measured with each of the six vertical JDMDs located at the corners of the slabs in the 6×6 sections (see Figure 2.3 (“Instrumentation of the ENV sections”) and the sensor-naming convention in the Appendix.



Notes: - Positive displacement is upward.
 - Each curve in this figure is a weighted average of the vertical JDMDs located at the corners of each ENV section (four JDMDs in Section K and six JDMDs in the rest of the section).

Figure 3.54: Moisture-related component of the vertical displacements ($U_{V,Sh,T1}$), corner JDMDs.

Figure 3.54 shows that the largest vertical movements were registered on Section K (P2-ICC). This result was expected, since the section's slabs are full-lane width while the slabs of the other environmental sections instrumented with JDMDs are half-lane width. It is also in line with the fact that the P2-ICC mix showed the highest differential drying shrinkage values among all the mixes (Figure 3.38).

The lowest vertical movements corresponded to the CSA section (Section O), which again is in line with the differential drying shrinkage values shown in Figure 3.38.

The performance of Sections N (P3) and M (P2 cured with SRA) fell between that of Section O (CSA) and Section L (P2, standard curing). This was also observed in terms of the differential drying shrinkage measured by the VWSG sensors (Figure 3.38). As expected, there is a clear parallel between the vertical JDMD displacements in Figure 3.54 and the differential drying shrinkage values in Figure 3.38. This parallel is further explored below.

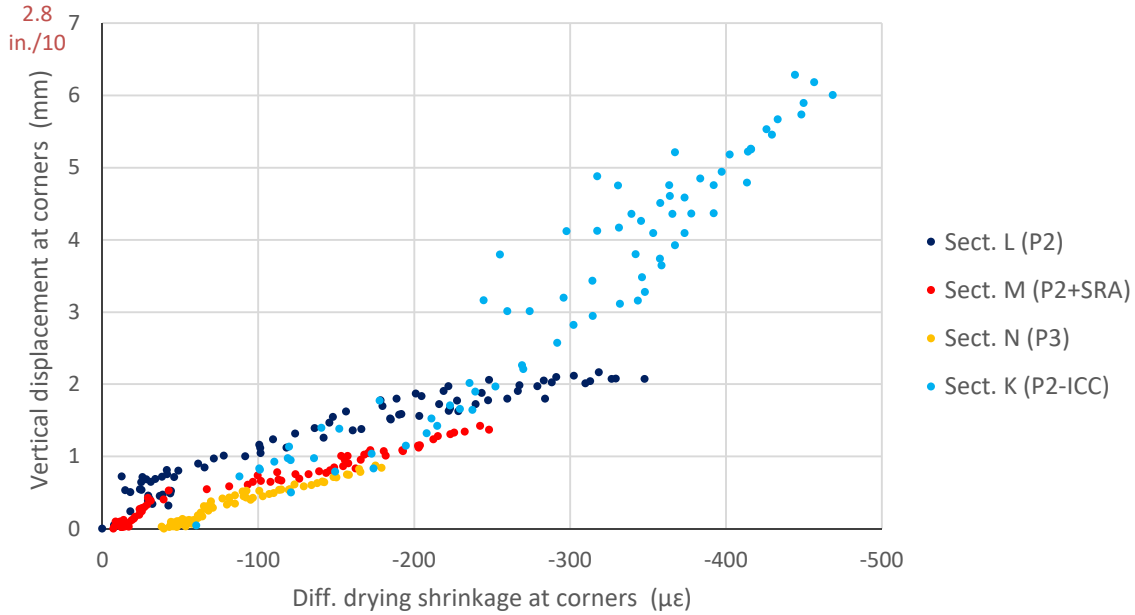
Effect of Environmental Conditions on Corner Vertical Displacements

Figure 3.54 shows the moisture-related component of the displacements measured with the vertical JDMDs located at the corners of each ENV section. As discussed in the preceding section, these displacements reflect the differential drying shrinkage taking place on the sections (top versus bottom of the slab) and, consequently, they can be used to estimate how environmental conditions impact slab warping.

Upward displacements due to top-down drying for periods without rainfall can be seen in Figure 3.54. The figure also shows that rainfall events produce an almost immediate effect on slab warping. The same quick reaction was observed in terms of differential drying shrinkage (Figure 3.38) and also in terms of relative humidity measured at 20 mm (0.8 in.) depth (Figure 3.13), which is expected as these are all manifestations of the same differential drying process.

Relationship Between Corner Vertical Displacements and Differential Drying Shrinkage

A clear parallel exists between the moisture-related component of the displacements measured at slab corners with vertical JDMDs (Figure 3.54) and the differential drying shrinkage estimated on the basis of readings from VWSGs—also located at the corners (Figure 3.38). This was an expected outcome since the corners' upward-downward movements are caused by temperature and drying shrinkage gradients through the slab thickness. The plot in Figure 3.55 shows both variables, with differential dry shrinkage on the x-axis and vertical displacement at the corners on the y-axis. As expected, a clear relationship can be seen between these two variables.



Notes: - Positive displacement is upward.

- The abscissa in the figure is the differential drying shrinkage determined from corner VWSG data (Figure 3.38). The ordinate is a weighted average of the moisture-related component of the displacements measured at the corners with vertical JDMDs (Figure 3.54). Each point in the graph corresponds to one day.

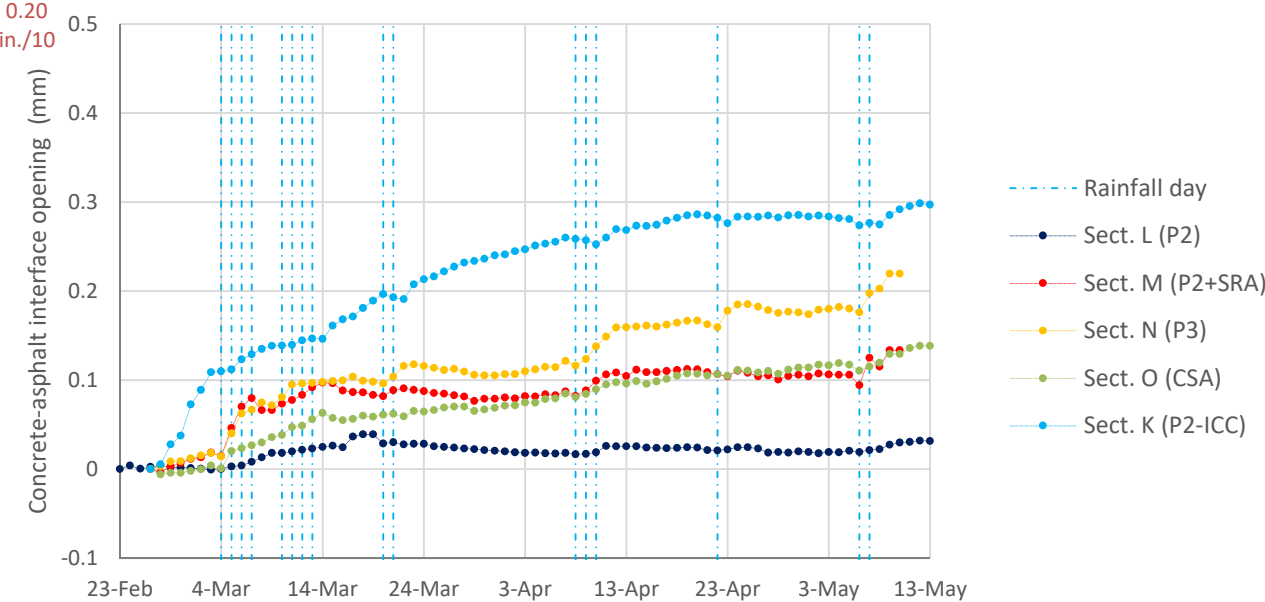
Figure 3.55: Corner vertical displacements versus differential drying shrinkage ($U_{V,Sh,T0}$ vs $\epsilon_{DIFF,Sh,T0}$).

The relationship between corner vertical displacements and differential drying shrinkage did not seem to significantly differ among the different sections. This relationship was expected to depend on slab size, on the bending stiffness of concrete slab and asphalt base, and on the stiffness of concrete-asphalt interface. Since the asphalt base was the same in all the sections with 6×6 slabs (Figure 2.2), large differences were not expected among these sections. As far as Section K is concerned, its slab size was double that of the rest of the sections (Figure 1.1) and its asphalt base was also much thicker (Figure 2.2). The larger slab size should result in larger displacements for the same level of differential drying shrinkage compared to the rest of the sections. However, the thicker asphalt base should result in the opposite outcome. The timing of joint deployment also plays a role in the relationship between corner displacements and differential drying shrinkage. Further analysis is required to determine why Section K did not considerably differ from the other sections in terms of the relationship between corner JDMD displacements and differential drying shrinkage.

Concrete-Asphalt Interface Opening

Figure 3.56 shows the moisture-related component of the concrete-asphalt interface opening measured with IOMDs in each ENV section. Each curve in the figure is the average of the two IOMDs installed in each of the sections. The low values for interface opening reflected in Figure 3.56, especially when compared to the corner

displacements shown in Figure 3.54, indicate that the concrete and asphalt remained bonded. This means that as the slab corners curled upward they pulled the asphalt base upwards as shown in Figure 3.54, up to 6 mm in the case of Section K. This indicates that slabs can warp significantly without losing contact with the asphalt base, at least in the nine month time period of this monitoring, and it is likely that the concrete and asphalt base will continue working together as a composite structure. This outcome has significant consequences for the good performance of BCOA sections.



Note: Each curve in this figure is the average of the two IOMDs of each ENV section.

Figure 3.56: Moisture-related component of concrete-asphalt interface opening measured with IOMDs (I_{sh,10}).

4 CONCLUSIONS

Fifteen bonded concrete overlay of asphalt (BCOA) sections were built at the UCPRC facility in Davis, California, from February 23 to 25, 2016. Six of the 15 sections were instrumented with 245 sensors to measure the response of the concrete slabs to environmental actions and cement hydration. The structural response of the slabs was measured with vibrating wire strain gages (VWSGs), joint displacement measuring devices (JDMDs), and interface opening measuring devices (IOMDs). Concrete temperature, internal moisture, and internal relative humidity were measured as well. Most of the 245 sensors began collecting data on the day before the construction of the overlay, and data collection continued on a regular basis for approximately 15 months, up until May 31, 2017. Based on the analysis of that data, preliminary conclusions were drawn about how the different section configurations and concrete types responded to moisture and temperature-related actions. These preliminary conclusions are summarized below:

Conclusions Related to Moisture-Related Shrinkage

- Very high levels of moisture-related shrinkage were measured in all the portland cement mixes treated with curing compound: 550 to 800 $\mu\epsilon$ were measured in a set of unrestrained shrinkage beams located outdoors by the test sections, and 450 to 550 $\mu\epsilon$ differential drying shrinkage (the difference between the strains at the top and at the bottom of the slab, measured at the corner) were measured in the BCOA sections.
- The peak value of differential drying shrinkage in the section with Type III portland cement was 10 percent lower than in the section with Type II/V portland cement, both of which were treated with curing compound.
- The peak value of differential drying shrinkage in the section with calcium sulfoaluminate (CSA) cement was 53 percent lower than in the section with Type II/V portland cement, both of which were treated with curing compound.
- The topical use of a shrinkage-reducing admixture (SRA), 275 ml SRA/m² (7.8 oz/yd²), prior to the application of the curing compound considerably reduced the moisture-related shrinkage of the Type II portland cement mix. The peak value of the differential drying shrinkage in the SRA-treated section was 27 percent lower than in its untreated counterpart. The SRA effect was also verified in terms of an increase in concrete relative humidity at 20 mm (0.8 in.) depth.
- The replacement of 50 percent of the sand of the Type II/V cement mix with pre-wetted lightweight aggregates was effective in reducing the autogenous shrinkage that barely occurred in the internally cured mix. However, the internally cured mix resulted in a 6 percent higher differential drying shrinkage peak value and lower internal relative humidity than the original mix.

- Around 200 to 250 $\mu\epsilon$ of autogenous shrinkage was estimated for both mixes with Type II/V and Type III portland cement and water/cement ratios of 0.33 and 0.31, respectively. No autogenous shrinkage was measured in the CSA mix, which actually underwent a slight expansion.

Conclusions Related to the Effects of Environmental Conditions

- The relative humidity and moisture-content sensors located at 20 mm (0.8 in.) depth in the concrete slabs clearly reflected the drying and wetting processes related to environmental conditions. However, environmental conditions did not seem to have much of an effect on the measurements at 50 mm (2.0 in.) depth.
- Rainfall events produced an almost immediate increase in relative humidity at 20 mm (0.8 in.) depth. The same quick reaction was observed in terms of the decrease in magnitude of the differential drying shrinkage and uplift at the slab corners.
- Relative humidity (RH) sensors located at 20 mm (0.8 in.) depth showed that concrete RH increased linearly with temperature, with the proportionality factor being a mix-dependent function of concrete RH. The RH in the portland cement mixes changed as much as 0.5 percent/ $^{\circ}\text{C}$ (0.25 percent/ $^{\circ}\text{F}$).
- The mixes with Type II/V cement presented higher concrete and asphalt temperatures and higher positive temperature gradients (top warmer than bottom) than the mixes with CSA and Type III cements. This outcome was attributed to the higher albedo (that is, higher capacity for reflecting solar radiation) of the mixes with CSA and Type III cements compared with the mixes with Type II/V cement.

Conclusions Related to Thermal Deformation of the Slabs

- The coefficient of thermal expansion of the mixes was highly influenced by concrete moisture conditions. CTE tended to increase during dry periods compared with the laboratory value measured under saturated conditions and to decrease after rainfall events.
- Thermal deformations measured on a set of beams located outdoors by the test track were much higher—up to 50 percent greater—than the values predicted using the coefficient of thermal expansion determined in the laboratory under saturated conditions.

Conclusions Related to Joint Deployment and BCOA Performance

- With the exception of some transverse joints in the CSA sections, cracks were observed at all the transverse joints of all the other sections by August 2016. This high level of joint deployment is related to the high drying shrinkage levels that were estimated for all mixes.
- There was a clear link between joint deployment, evaluated by visual assessments, and thermal bending compliance of the slabs (the ratio of slab differential strain—that is, top to bottom of the slab—to slab

equivalent linear temperature difference) evaluated on the basis of VWSG data. In most cases, the VWSG data anticipated the results of visual assessments.

- The concrete-asphalt interface opening measured with IOMDs indicated that the concrete and asphalt remained bonded 15 months after the overlay construction despite the high levels of warping, with up to 6 mm of upward movement at the corners, measured in all the portland cement sections.

REFERENCES

1. Mateos, A., J. Harvey, F. Paniagua, J. Paniagua, and R. Wu. 2018. Development of Improved Guidelines and Designs for Thin Whitetopping: Construction and Initial Environmental Response of Full-Scale BCOA Sections. (UCPRC-RR-2017-01).
2. Mateos, A., J. Harvey, J. Paniagua, R. Wu, and F. Paniagua. 2018. Development of Improved Guidelines and Designs for Thin Whitetopping: Environmental Effects on the Coefficient of Thermal Expansion of the Concrete. Research Report: UCPRC-RR-2017-04. *In progress*.
3. Mateos, A., J. Harvey, F. Paniagua, J. Paniagua, and R. Wu. Development of Improved Guidelines and Designs for Thin Whitetopping: Moisture-Related Shrinkage of BCOA Sections. 2019. Research Report: UCPRC-RR-2017-05.
4. Sun, R. J., Z. Ge, W. Li, H.F. Zhou, and D.W. Huang. 2013. Experimental Research of the Rapid Set Cement Concrete for Rapid Repair of Concrete Pavements. In *Advanced Materials Research* (Vol. 634, pp. 2697-2701). Trans Tech Publications.
5. Jones, D., R. Wu, and S. Louw. 2014. Full-Depth Recycling Study: Test Track Construction and First Level Analysis of Phase 1 HVS and Laboratory Testing. UCPRC-RR-2014-03.
6. Heath, A.C., and J.R. Roesler. 1999. Shrinkage and Thermal Cracking of Fast-setting Hydraulic Cement Concrete Pavements in Palmdale, California. University of California Pavement Research Center, Institute of Transportation Studies, University of California, Berkeley. UCPRC-RR-1999-07.
7. Janssen, D. J., and M.B. Snyder. 2000. Temperature-moment Concept for Evaluating Pavement Temperature Data. *Journal of Infrastructure Systems*, Vol. 6(2), 81-83.
8. Caltrans weather regions web site http://www.dot.ca.gov/hq/maint/Pavement/Offices/Pavement_Engineering/Climate.html
9. Villani, C., C. Lucero, D. Bentz, D. Hussey, D.L. Jacobson, and J.W. Weiss. 2014. Neutron Radiography Evaluation of Drying in Mortars with and without Shrinkage Reducing Admixtures. In *American Concrete Institute Fall Meeting*, Washington, DC (October: Vol. 26).
10. Bentz, D.P., and W.J. Weiss. 2011. Internal Curing: A 2010 State-of-the-Art Review. US Department of Commerce, National Institute of Standards and Technology.
11. National Cooperative Highway Research Program. 2004. "AASHTO Mechanistic-Empirical Design Guide," NCHRP Project 1-37a, Transportation Research Board, Washington, DC.
12. Ruiz, J. M., S. Garber, and J.C. Dick. 2015. Computer-Based Guidelines for Concrete Pavements, HIPERPAV III[®], Version 3.3 User's Manual (No. FHWA-HRT-14-087)
13. Sellevold, E.J., and Ø. Bjøntegaard. 2006. Coefficient of Thermal Expansion of Cement Paste and Concrete: Mechanisms of Moisture Interaction. *Materials and Structures*, Vol. 39(9), 809-815.

14. Meyers, S.L. 1951. How Temperature and Moisture Changes May Affect the Durability of Concrete. *Rock Products*, Vol. 54(8), 153-162.
15. Jonasson, J.E., and H. Hedlund. 2000. An Engineering Model for Creep and Shrinkage in High Performance Concrete. Reunion Internationale des Laboratoires D'essais et de Recherches sur les Materiaux et les Constructions (RILEM) proceedings, Shrinkage of Concrete, Shrinkage 2000, 507-529.
16. Bentz, D.P., E.J. Garboczi, and D.A. Quenard. 1998. Modelling Drying Shrinkage in Reconstructed Porous Materials: Application to Porous Vycor Glass. *Modelling and Simulation in Materials Science and Engineering* 6, no. 3: 211.

APPENDIX: SENSOR-NAMING CONVENTION

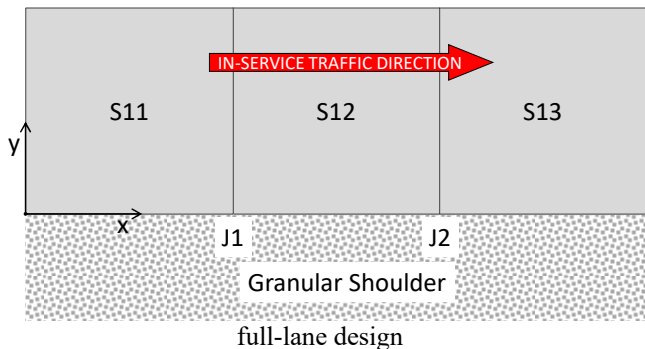
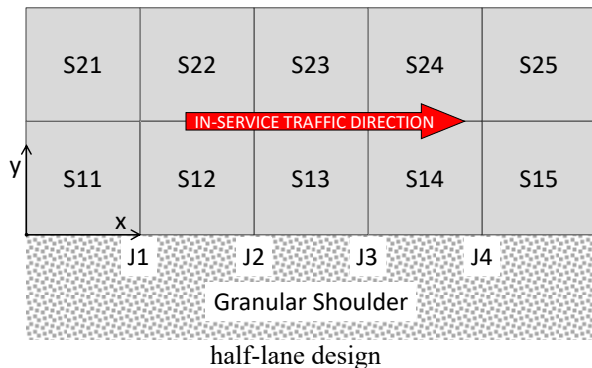
A coding system has been used to assign each sensor a unique identifier. Each identifier is composed of four parts, separated by dots (for example, “Therm.A.S12+R.180.”) How this identifier was arrived at is indicated below:

1. The first part of the name indicates the sensor type and direction (where applicable). The short names used for the different types of sensors are shown in Table A.1. The direction code is applicable for strain gages and JDMDs.

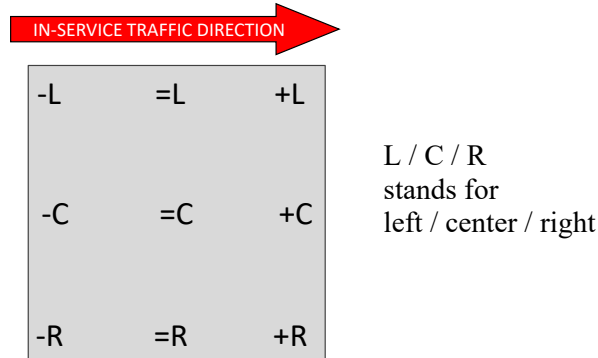
Table A.1: Short Names of the Sensor Types

Short Names	Sensor Type	Direction
Therm	Thermocouple	Not applicable
DySG	Dynamic strain gage	Transverse (T)
StSG	Static (vibrating wire type) strain gage	Longitudinal (L)
JDMD	LVDT	Vertical (V) Horizontal (H)
IOMD	LVDT	Not indicated, since they are always vertical
RHC	Relative humidity, CS215-L	Not applicable
RHS	Relative humidity, SHT75 with Univ. of Pittsburgh set up	Not applicable
MC	Moisture content	Not applicable

2. The second part indicates the letter of the section where the sensor was installed. For example, “C” is used for Section C.
3. The third item in the identifier indicates the sensor location, as indicated by the slab or joint number, preceded by the letter “S” for slab or “J” for joint, and by the location within the slab or joint. For example, “J3R” is used for the right edge of Joint 3.
 - a. Slab and joint numbers have been assigned as indicated below. Each section has a hypothetical traffic direction (that is, the direction traffic would flow if this was an in-service pavement in the US).

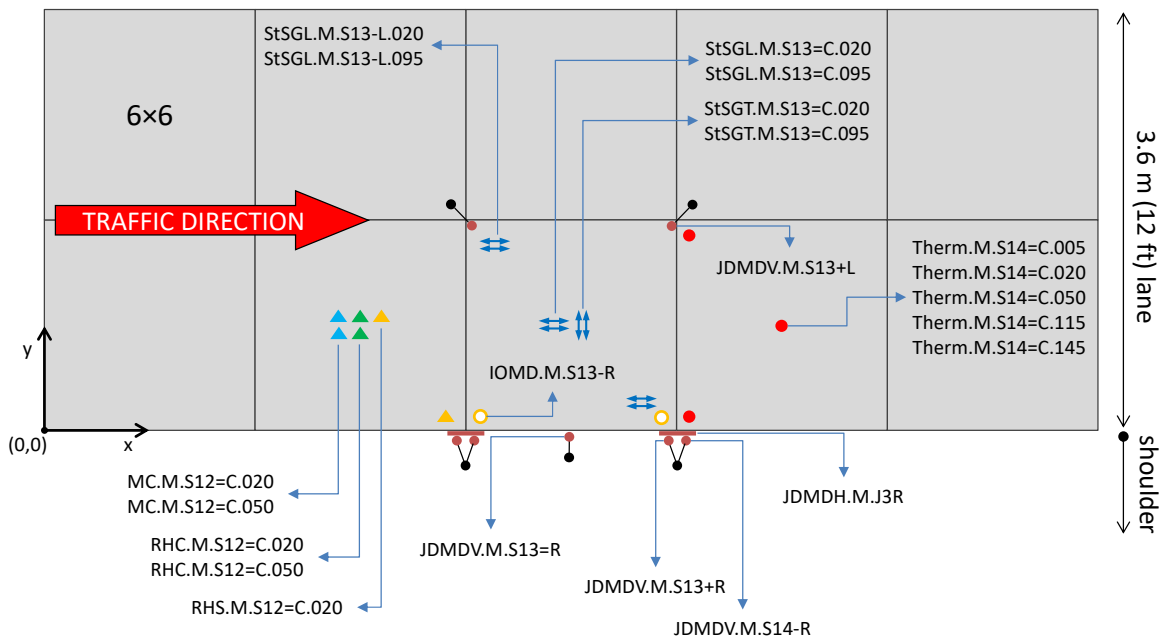


- b. The sensor's location within the slab is indicated with a symbol and a letter, as indicated below. Its location within a joint is indicated with either an "L" for left or an "R" for right. A minus sign (-), an equal sign (=), or a plus sign (+) refers to the approaching, middle, or leave part of a slab, respectively.



4. The fourth part of the identifier indicates the theoretical depth of the sensor, in millimeters.

As examples, Figure A.1 and Figure A.2 include sensor code identifiers for Sections M and K, respectively.



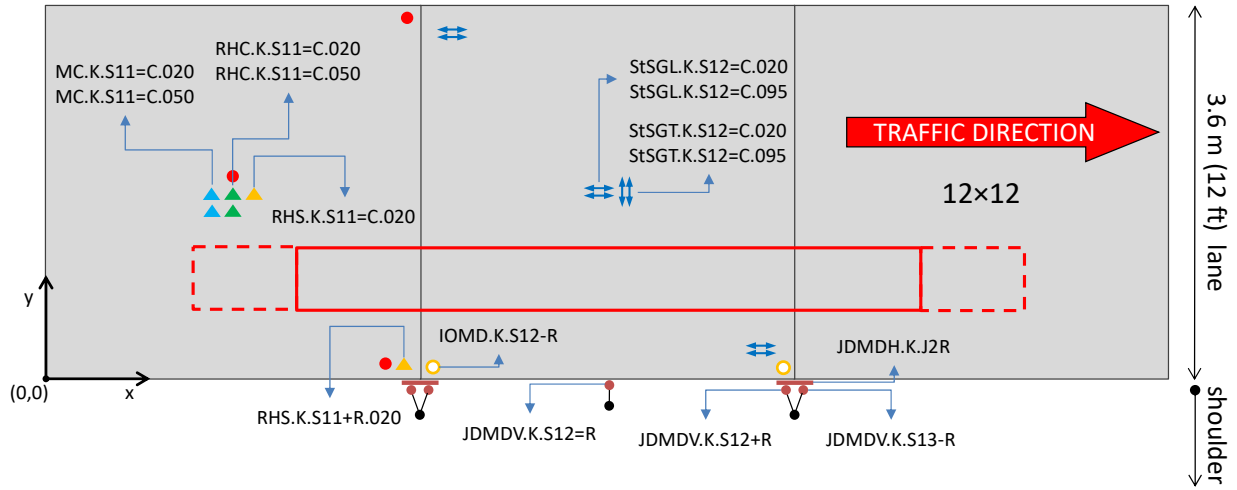


Figure A.2: Example sensor codes (Section K).